IMPRINT LITHOGRAPHY AND CHARACTERIZATION OF PHOTOSENSITIVE POLYMERS FOR ADVANCED MICROELECTRONICS PACKAGING

A Dissertation
Presented to
The Academic Faculty

by

Venmathy Rajarathinam

In Partial Fulfillment
of the Requirements for the Degree
Doctor of Philosophy in the
School of Chemical & Biomolecular Engineering

Georgia Institute of Technology
August 2010

IMPRINT LITHOGRAPHY AND CHARACTERIZATION OF PHOTOSENSITIVE POLYMERS FOR ADVANCED MICROELECTRONICS PACKAGING

Approved by:

Dr. Sue Ann Bidstrup Allen, Advisor
School of Chemical & Biomolecular Engineering
Georgia Institute of Technology

Dr. Paul A. Kohl, Advisor
School of Chemical & Biomolecular Engineering
Georgia Institute of Technology

Dr. Farrokh Ayazi
School of Electrical Engineering
Georgia Institute of Technology

Dr. Dennis W. Hess
School of Chemical & Biomolecular Engineering
Georgia Institute of Technology

Dr. Hang Lu
School of Chemical & Biomolecular Engineering
Georgia Institute of Technology

Dr. Carson Meredith
School of Chemical & Biomolecular Engineering
Georgia Institute of Technology

Date Approved: June 15, 2010

In dedication to my loving parents

ACKNOWLEDGEMENTS

I would like to express sincere gratitude to my thesis advisors, Prof. Paul Kohl and Prof. Sue Ann Bidustrup Allen for their advice, support, and encouragement during my time at Georgia Tech. I would also thank my thesis committee members Prof. Dennis Hess, Prof. Hang Lu, Prof. Carson Meredith, and Prof. Farrokh Ayazi for their helpful input during my Ph.D. I would also like to give a very special thank you to all my current and past group members who have helped make my time at Georgia Tech such a wonderful experience. Thank you in particular to Dr. Ate He, Dr. Tyler Osborn, C. Hunter Lightsey, and Nathan Fritz for all their help with the work presented in this thesis and my undergraduate research assistants Shakira Charles, Laura Gaskins and Lisa Thornsberry for their assistance with running experiments. I would also like to thank Daphne Perry who goes above and beyond to ensure that everything in the Kohl Group runs smoothly.

This work would not have been possible without the support of the IFC, and I would like to acknowledge Prof. Andrei Federov, Dr. Yogendra Joshi, Dr. Kevin Martin, and Dr. Muhannad Bakir for their many insightful discussions. Thank you to the MiRC Cleanroom staff Gary Spinner, Charlie Suh, Tran-Vinh Nguyen, Devin Brown, Janet Cobb, William Kimes, Ben Hollerbach, John Pham, Walter Henderson, Eric Woods Gregory Book, Scott Fowler, and Mikkel Thomas for all their assistance throughout my time in the cleanroom. Thank you also to Dr. Ed Elce and Brian Knapp from Promerus LLC for their insight and support. Finally, I would like to thank my family for all of their encouragement.

TABLE OF CONTENTS

LIST OF TABLES

LIST OF FIGURES

LIST OF SYMBOLS AND ABBREVIATIONS

γ	Contrast
AC	Alternating current
BGA	Ball grid array
COB	Chip on board
CTE	Coefficient of thermal expansion
D_0	Exposure dose at which all of the photodefined material is removed upon exposure to developer
D_{100}	Exposure dose at which none of the photodefined material is removed upon exposure to developer
DSC	Differential scanning calorimetry
E_r	Reduced modulus
FTIR	Fourier transform infrared
Ghz	Gigahertz
H	Hardness
I/O	Input/Output
IC	Integrated circuit
ITRS	International technology roadmap for semiconductors
MEMS	Microelectromechanical systems
PAG	Photo-acid generator
PCB	Printed circuit board
PDMS	Polydimethylsiloxane
PEB	Post-exposure bake
PGMEA	Propylene glycol monomethyl ether acetate
PMMA	Poly(methyl methacrylate)

POSS	Epoxycyclohexyl polyhedral oligomeric silsesquioxane
PPC	Polypropylene carbonate
RF	Radio frequency
RIE	Reactive ion etching
RPM	Revolutions per minute
SEM	Scanning electron microscope
T_g	Glass transition temperature
TGA	Thermogravimetric analysis
UV	Ultraviolet

SUMMARY

To enable fast and reliable processors, advances must be made in the interconnections on the printed circuit board and in the interconnections from the chip to the printed circuit board. Processing techniques have been demonstrated to fabricate a copper-clad encapsulated air dielectric layer to enable low loss off-chip electrical signal lines using sacrificial polymers and the three dimensional patterning capabilities of imprint lithography. The inclusion of an air gap can eliminate the dielectric loss allowing the signal to propagate over longer lengths. Additionally, the low dielectric constant of air lowers the loss contributions from the conductor and increases the signal propagation velocity reducing delay. The metal shielding could minimize the crosstalk noise and radiation losses that are significant at high frequencies. The three dimensional patterning capabilities of imprint lithography fabricated curved structures and rounded terminations which can reduce reflections at discontinuities. Furthermore, imprint lithography also created planarized surfaces which simplified the buildup process. Since imprint lithography, only uses temperature and pressure to make a pattern it is an inexpensive and simple process advancement. The metal-clad encapsulated air dielectric structures were fabricated in a comparable number of registration steps to traditional transmission lines.

Implementation of all copper chip to substrate interconnects would provide high conductivity electrical connections, resistance to electromigration while avoiding formation of brittle intermetallics. High aspect ratio polymer molds for copper electroplating interconnects could enable improved integrated circuit electrical performance. The properties of a new aqueous base develop, negative-tone photosensitive polynorbornene polymer have been characterized to develop

mechanically compliant all copper connections between the chip and printed circuit board. High aspect ratio features of 7:1 (height:width) were produced in 70 μm thick films in a single coat with straight side-wall profiles and high fidelity. The polymer films studied had a contrast of 11.6 and a low absorption coefficient. To evaluate the polymer's suitability to microelectronics applications, epoxy cross-linking reactions were studied as a function of processing condition through Fourier transform infrared spectroscopy, nano-indentation, and dielectric measurements. The fully cross-linked films had an elastic modulus of 2.9 GPa and hardness of 0.18 GPa which can improve the mechanical compliance of the copper interconnections.

A photo-imprint lithography process was developed to improve the photo-patterning of the polynorbornene polymer for high aspect ratio hollow structures. A shallow photo-imprint stamp was developed to physically displace material in the polymer core. Since the imprint stamp displaces material in the area of the feature, the effective film thickness is reduced compared to the bulk film. The reduction in film height reduced the effects of scattering in the core and also facilitated transport of developer within the core. The photo-imprint lithography process resulted in high aspect ratio hollow core pillars that exceeded optical resolution capabilities for comparable feature sizes.

CHAPTER 1

PROJECT MOTIVATION

Imprint lithography is a rapidly evolving field because of its potential as a next generation lithography technique that is economically viable and capable of achieving high resolution. There are many variations on the imprint process [1-4], but all require conformal replication of stamp topography to generate patterns. A stamp with a three dimensional pattern is pressed into a moldable material, and after the material replicates the pattern on the stamp, the material is hardened. Like other lithography techniques, imprint lithography requires precise X-Y stages, layer-to-layer alignment systems, and wafer handling equipment. However, the primary advantage of imprint lithography over optical lithography is that it is a contact patterning method, and its resolution is limited by the resolution of the stamp and the resolution of the pattern replica. Therefore, the primary constraint of this technique is the ability to fabricate stamps of adequate spatial resolution and of sufficient durability. The quality of the pattern generated is limited by the capacity of a material to replicate the pattern, and the ability to separate the stamp and imprint material while retaining the imprinted shape.

Extensive research has been devoted over the past decade to study the use of imprint lithography to enable manufacturing of semiconductor integrated circuits (IC) at the nanometer scale. Chou et al. demonstrated the potential of thermal imprint lithography to fabricate sub-10 nm patterns [5]. Resnick et al. have demonstrated patterned areas of high and low density, semi-dense and isolated lines to 20 nm [4]. These ICs need to be connected to other components on a printed circuit board (PCB) to form electronic

products. Packaging is defined as the bridge that connects the integrated circuit with other components on a system level [6]. The development of imprint lithography processes for advanced packaging applications could advance IC performance capabilities with high throughput and yield while maintaining low cost.

In this project, imprint technology has been applied to two microelectronics packaging applications to enable high performance chip-to-chip communication. Particular focus has been placed on the capability of imprint lithography to produce complex, high aspect ratio and three-dimensional patterns which are challenging to fabricate with traditional processing techniques. Specifically, imprint lithography has been applied to fabricate copper-clad encapsulated air dielectric layers to achieve low-loss, off-chip, air-gap electrical signal lines and to fabricate high aspect ratio hollow core pillars to facilitate dense pin count chip-to-board all copper connections.

Routing high frequency (multi-GHz) signals off-chip is a challenging task. Molecules in the dielectric layer attempt to align to the alternating electric field resulting in energy dissipated as heat. Low loss structures are needed to enable high frequency chip-to-chip communication. Air dielectric layers can lower power loss contributions from both the conductor and dielectric, and a coaxial structure could provide electrical shielding [7]. However, the complex geometric shape of the coaxial structure is challenging to fabricate with traditional processing. Development of the imprint process to pattern complex geometric patterns could enable high frequency chip-to-chip communication.

Implementation of all copper chip to substrate interconnects could allow significant advances in IC performance. An all copper connection would provide high

conductivity electrical connections, resistance to electro-migration while avoiding formation of brittle intermetallics [8]. Copper interconnects have been demonstrated to have high bonds strengths with low annealing temperatures that are compatible with organic substrates [9]. However, to achieve mechanical compliance these structures need to have high aspect ratios. High aspect ratio photo-processing of polymers is difficult with photolithography techniques. Thick films suffer from light scattering, resulting in poor resolution compared to thin films. Since imprint stamps can be used to displace material in specific areas, the effective film thickness in the feature area could be reduced compared to the bulk film. Development of the imprint process to fabricate high aspect ratio polymer molds for copper electroplating interconnects could enable improved IC electrical performance and reliability.

CHAPTER 2

INTRODUCTION TO IMPRINT LITHOGRAPHY AND POLYMER CHARACTERIZATION

This chapter provides a basic overview of imprint lithography and polymer characterization to facilitate understanding of the work presented in this thesis.

2.1 Imprint Lithography

2.1.1 Introduction

Imprint lithography has emerged as a high throughput and resolution patterning method that relies on mold replication to generate patterns. Imprint lithography has influences from previous technologies and applications such as compression injection molding of compact discs [10], microreplication by LIGA [11], embossing of holograms, and semiconductor manufacturing [12-14]. Much of the research in next generation lithography is focused on projection optics, mask schemes, and exposure systems that are very expensive and contribute heavily to the overall equipment costs. In order to minimize lithography tool costs while achieving further resolution improvements, many researchers have explored the use of imprint lithography as an inexpensive pattern generation technique for features below 100 nm. Imprint lithography can potentially realize significant cost savings over next generation lithography techniques because it eliminates expensive projection optics and exposure systems needed to achieve resolution targets. Furthermore, imprint lithography takes advantage of precision X-Y stages, layer-to-layer alignment systems, and wafer handling equipment derived from current lithography technology to further reduce development costs. The International Technology Roadmap

for Semiconductors accepted imprint lithography as a next generation lithography candidate for the 32 nm technology node and beyond for manufacturing in 2013 [15].

Aside from the potential tool cost savings, imprint lithography has some fundamental advantages over conventional optical lithography and next generation lithography techniques. Imprint lithography is non-optical by design and its resolution appears to be limited only by the structures that can be generated on the stamp. Imprint stamps can take full advantage of the resolution provided by e-beam technology to define high resolution structures without compromising throughput goals required for high volume manufacturing. Moreover, complex geometries such as curved, multi-relief, and high aspect ratio structures that are challenging to fabricate with traditional processing techniques can be achieved with imprint lithography [1,16-17]. An additional potential benefit of imprint technology is that tool life is not restricted to one technology node. As advances in imprint lithography are dictated by template and process development, an imprint tool inserted at the 32 nm technology node could extend over several technology nodes.

A standard process cannot be defined yet for imprint lithography and this is reflective of the many diverging applications that have different requirements and unique challenges such as microelectromechanical systems **(**MEMS) versus IC manufacturing. All techniques rely on mold replication to generate patterns, but the imprint materials and curing process divide imprint lithography. For simplicity, the techniques will be classified into two primary approaches: (i) imprinting into a thermoplastic or thermoset material at elevated temperatures and pressures, and (ii) imprinting into a photo-definable material.

2.1.2 Thermal Imprint Lithography

In thermal imprint lithography, a stamp with a three dimensional relief pattern is pressed into a thermoplastic material at a temperature above the glass transition temperature of the material and pressure on the order of 10 to 100 MPa until the material conforms to the stamp relief patterns. The mold and substrate are then cooled below the glass transition temperature to set the mold pattern, and then the mold is separated from the substrate. This imprint lithography process is illustrated in Figure 2.1.

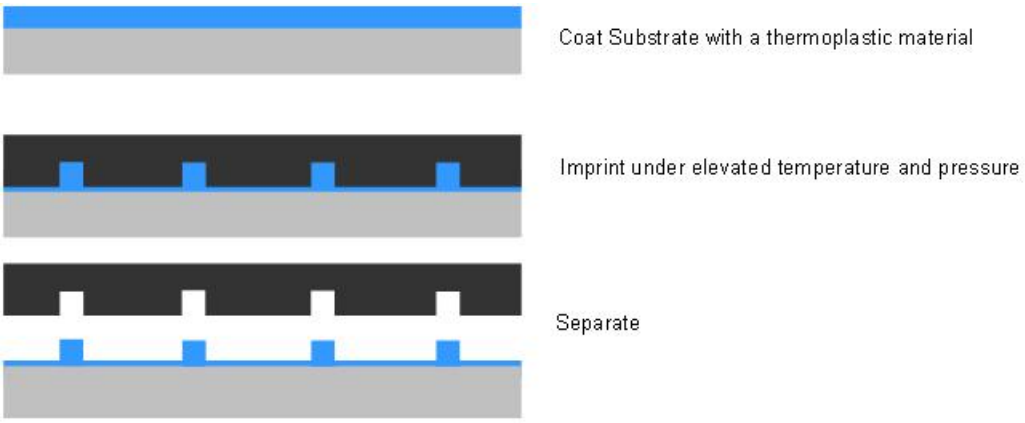

Figure 2.1: Thermal imprint lithography process

The thermal imprinting process has been studied by many researchers including Chou et al. [1,18-20], Scheer et al. [21], and Schift et al. [3,22-23]. Chou et al. have fabricated many devices including high density magnetic storage [18], compact disks [24], photodetectors [25], single-electron transistor memory [26], and field effect transistors [2]. These devices were all made using thermal imprint lithography, but none required significant overlay control and had an alignment accuracy on the order of 1μm [27]. Scheer et al. have focused their work on the fundamentals of thermal imprint patterning [21,28].

The authors have shown that the process can be limited by material transport, and that pressures around 100 bar and temperatures 90ºC above the polymer glass transition temperature are optimal for material displacement [21,28]. Furthermore, the authors conclude that regular, repeating patterns that require little material displacement are ideal for this type of patterning [21,28]. Schift et al.[22-23] have developed a hot embossing technique which is similar to the methods demonstrated by Chou and Scheer and have demonstrated compatibility with metal lift-off techniques using titanium [3].

There are several challenges with this technique including layer to layer registration and alignment control. Because imprinting is done at elevated temperature, different coefficients of thermal expansion (CTE) between materials on the stamp and the substrate can cause challenges for multiple layer overlay. Furthermore, non-transparent templates commonly used in this approach make layer-to-layer alignment difficult. Also due to the heating cycles required to heat the material above the glass transition temperature (T_g) and subsequently cool the system, the process can be slow for mass manufacturing. Additionally, the high forces required to displace high viscosity materials could cause mechanical distortions to the underlying layers.

To mitigate CTE mismatch, many processes use silicon for both the template and substrate. However, the use of non-transparent templates makes layer-to-layer alignment difficult. To achieve overlay alignment through silicon templates, infrared light must be employed but this limits the resolution to approximately 100 nm due to its long wavelength. Alignment of both the template and wafer could be performed separately to a common reference point, but would require X-Y stages with a precision beyond what is

currently available. To address the thermal cycling limitations, Chou and coworkers developed polymers with lower T_gs that can be processed at approximately 100°C [29].

2.1.3 UV Imprint Lithography

During the ultraviolet imprint process, a transparent stamp with surface relief structures is brought into contact with a photosensitive material. Temperature and pressure are applied to cause the photosensitive material to fill the mold, and UV light is then emitted to photo-cure the substrate. Pressure is then released, and the substrate is separated from the mold. This process can utilize low viscosity photosensitive materials, allowing the imprint to be accomplished at lower temperatures and pressures than thermal imprint lithography. The photo-imprint process is illustrated below in Figure 2.2.

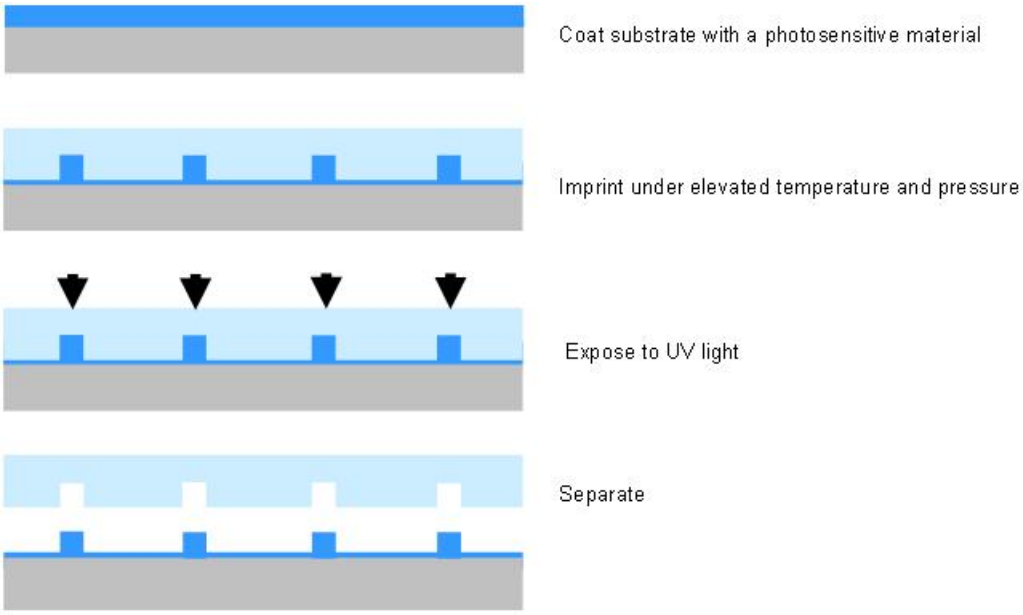

Figure 2.2: UV imprint lithography process

Phillips Research used a UV imprint process to demonstrate high resolution patterning of polymer features [30] and to fabricate optical disks [31] using a low viscosity liquid acrylate. Since the process does not require high temperatures, thermal expansion mismatch is not of concern. Furthermore, the use of transparent templates makes through-template overlay alignment possible, and the use of low-viscosity polymers reduces the pressure required for filling the mold. The Phillips Research group has demonstrated the ability to pattern sub-50 nm features, but it did not produce high aspect ratio features or high etch resistance which is unfavorable for semiconductor manufacturing [30].

Willson and coworkers have also demonstrated a method to combine the benefits of thermal imprint lithography with traditional photolithography techniques [32]. In this method called step and flash imprint lithography, a bilayer resist scheme is used to produce high aspect ratio features with etch resistance. The use of a low-viscosity UV

curing solution allows imprinting at room temperature with minimal pressure. The imprinting process is performed over a blanket layer of organic polymer to create a bilayer structure, and the pattern aspect ratio is subsequently amplified by reactive ion etching. The use of a transparent stamp allows flood exposure and enables traditional optical techniques for layer-to-layer alignment. This technique has successfully patterned areas of high and low density, semi-dense and isolated lines down to 20 nm [4] and demonstrated the capability of layer-to-layer alignment [33]. Step and flash imprint lithography has also produced functional optical devices with a micropolarizer array consisting of orthogonal 100 nm titanium lines and spaces fabricated using a metal lift-off process [32].

Guo and coworkers developed a technique to integrate photolithography and imprint lithography [17]. In this technique shown in Figure 2.3, a hybrid mask is used that is UV transparent and protrusions are made on the stamp for imprinting nano-scale features, and metal pads are used as a mask for large features [34]. The hybrid stamp is first imprinted into a negative-tone resist under pressure and then exposed to UV radiation. After the stamp and substrate are separated the sample is developed in solution to remove the unexposed regions. The use of a hybrid mask allows the patterning of large-scale and nano-scale structures simultaneously. This technique was able to fabricate large scale features on the order of 200 μm and nano-scale features on the order of 350 nm in SU-8[17]. Since the large features are patterned using photolithography, minimal material has to be displaced, allowing the process to be run at a low imprinting pressure. Furthermore, a metal layer was placed onto the top of the stamp protrusions to prevent the exposure of the resist layer underneath [17]. Therefore, chemical selective removal of

the residual layer was possible, and the resist patterns could then have a higher aspect ratio than the feature on the stamp.

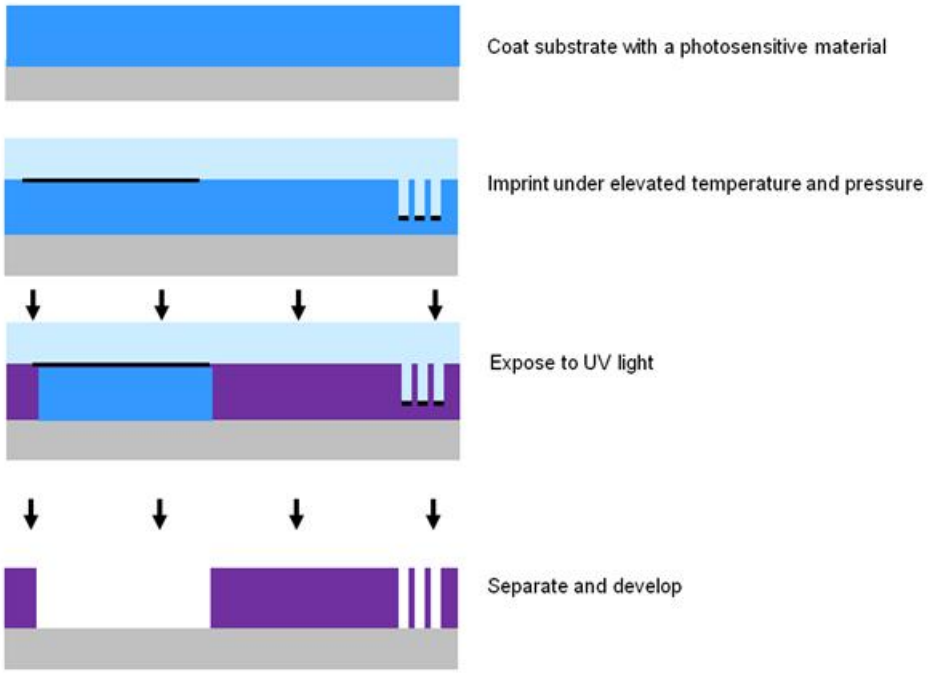

Figure 2.3: Combined imprint and photolithography process

2.1.4 Imprint Stamps

A stamp used in imprint lithography can be made of any solid material that has high strength and durability. Typical considerations for selecting mold materials include hardness, compatibility with traditional microelectronics fabrication techniques, application requirements, and thermal expansion coefficient of the material. Si, SiO_2, and metals such as nickel have been traditionally used for imprint applications and have demonstrated sufficient hardness and high mechanical strength. The primary requirement is that the protrusion pattern should not deform, buckle, or collapse even on the

nanometer scale. The imprint resist can act as a shock absorber slowing down the stamp/substrate closing velocity by squeeze flow and thereby reduce the risk of breaking fragile structures upon contact with the substrate. It is also advantageous for the stamp to have global flexibility and local rigidity, so that large-area conformal contact can be maintained without high pressures [35]. For imprinting conducted at elevated temperatures, the thermal expansion coefficient of the material becomes important. Thermal mismatch between the stamp and the substrate can cause pattern distortion or stress buildup during the heating and cooling cycles. Furthermore, the lifetime of the stamp is determined by contamination and damage. Cleaning of stamps becomes necessary if resist residue adheres or particles become lodged into one of the features of the stamp. Once such a defect occurs it can be repeated in subsequent imprints or cause damage to the substrate or stamp. To counteract these issues, Obducat has developed an intermediate polymer stamp that is used for every single imprint [36]. This process prevents the fracture of the hard master stamp because contamination is enclosed by the intermediate stamp. Furthermore, due to the hydrophobic nature of the polymer stamp, no residue adheres to the master stamp eliminating the need for cleaning [37]. This process was developed to pattern via holes in printed circuit boards for a three level structure on the order of 20 μm and has been scaled down to structures with sub-100 nm resolution.

2.1.5 Imprint Release Layers

Since imprint stamps have surface relief patterns, the effective total surface area that contacts the imprint material is high. Imprint material will readily adhere to stamps with no surface treatments. Adhesion between the stamp and the wafer can increase defect generation in the imprinted pattern, damage the stamp, or cause imprint material-

substrate delamination. There are several strategies used to reduce adhesion between the stamp and substrate and they include (i) applying a low surface energy coating to the stamp, (ii) using a stamp material with an intrinsically low surface energy, and (iii) incorporating a release agent into the imprint resist formulation. A self-assembled monolayer of a fluorosilane release agent is generally solution-phase or vapor-phase deposited on the stamp surface. Jung et al. compared solution-phase and vapor-phase deposition and concluded that vapor-phase coating had better anti-adhesion properties [38]. Schift et al. determined that co-depositing monochlorosilanes with trichlorosilanes reduced steric hindrance between the trichlorosilane molecules bound to the stamp surface resulting in better molecular packing [39]. These silanes have low surface energy, high surface reactivity, and high resistance at elevated temperature and pressures[39]. However, the fluorosilane layers applied to UV imprint stamps have been shown to undergo attack under different photosensitive resists [40]. Diamond like carbon has been successfully used as a imprint release layer for a methacrylate resist suggesting that a material with a low reactivity rather than a low surface energy can also act as a release agent [40-42]. It has also been shown that amorphous fluoropolymers such as Teflon AF can be used as an imprint release layer. The solution can be cast over the imprint stamp [43] or a flexible stamp can be made of the fluoropolymer [44]. Most imprint materials are homo-polymer resists and a new class of copolymers has been developed to minimize adhesion to the mold. A Polydimethylsiloxane-Poly(methyl methacrylate) (PDMS-PMMA) copolymer has been demonstrated to have low surface energy, low T_g, high thermal stability, and high etch resistance [45].

2.1.6 Imprint Resists

Since imprint lithography relies on mold replication to generate patterns, the imprint resist must be displaceable under elevated temperature and pressure. The imprint material must also have sufficient mechanical strength to retain stamp patterns after separation from the stamp. The flow of the polymer during imprint is governed by the viscoelastic properties of the material which vary depending on imprint temperature and pressure. The Young's modulus of the resist must be lower than that of the stamp, and the imprint should be conducted at pressures that are higher than the shear modulus of the polymer [46]. For thermal imprinting, the glass transition temperature of a polymer is often used to determine the imprint temperature and the de-molding temperature [47]. Schift et al. recommends an imprint temperature 50-70°C higher than the T_g of a polymer and a de-molding temperature 20°C lower the T_g [48]. Similar results were demonstrated when this principle was applied to several different thermoplastic polymers [48]. However, many applications require lower operating temperatures, and reductions in temperature can be mitigated by increasing imprint pressure and time [49]. The material should also have a viscosity that is low enough so that it is deformable under reasonable time frames [50]. For polymer viscosities on the order of 10^3-10^7 Pa·s, efficient squeeze flow can be achieved and repeating structures can be molded quickly while large unstructured areas take can take long times to fill [51]. Shear thinning may reduce the viscosity due to sliding of polymer chains and improve mold filling [52]. This behavior is more pronounced for polymers with longer chain lengths, and viscosity reductions were shown from 1.5 up to 4 orders of magnitude depending on the molecular weight of the polymer [52]. Other

important material properties include etch resistance, stiffness, refractive index, surface energy, photo-polymerization, adhesion, and CTE.

2.2 Polymer Characterization

2.2.1 Introduction

Polymers are widely used in the microelectronics industry as thin-film, dielectric layers with copper in substrates and packages, and as passivation layers on semiconductor devices. Epoxy based polymers are particularly useful in electronic packaging because they have excellent adhesion and react at modest temperatures. A challenging application space exists for photosensitive, thick-film, high aspect ratio polymers in microelectronics. To meet the high input/output (I/O) density projections, high aspect ratio connections and a high elastic modulus are needed to accommodate the stress between the chip and PCB. A polymer structure with an aspect ratio of 10:1 is required for such devices. It is difficult to use a traditional dry etching reactive ion etching (RIE) process to etch a polymer to achieve these dimensions.

However, high aspect ratio photo-processing of thick polymers is difficult with traditional photolithography techniques. Thick films suffer from light scattering, resulting in poor resolution compared to thin films. Furthermore, high aspect ratio hollow pillars are challenging to fabricate with photolithography because the transport of the developer in the core is slow in comparison with the transport of developer around the perimeter of the feature. As a result, hollow core pillars require longer development times than solid pillars of comparable aspect ratios, and at high aspect ratios delamination of the structure occurs before the core can be fully developed. Additionally, material limitations such as poor adhesion to the substrate can further exacerbate these challenges,

making this geometry difficult to fabricate. In this work, an imprint process has been developed to fabricate high aspect ratio polymer molds for electroplating copper interconnects.

However, the polymer properties required for this advanced packaging application are stringent. To evaluate suitable materials for this application, polymer properties were characterized and include: contrast, residual stress, elastic modulus, and dielectric constant. The following sections review the fundamental theory for characterizing these properties.

2.2.2 Contrast

An important characteristic of photosensitive polymers is contrast. For a negative-tone material, high contrast is achieved in a material when a small increase in exposure dose causes cross-linking and insolubility of the film in developer. Contrast is an important parameter for evaluating materials to determine if they can fabricate high-aspect-ratio (depth-to-width) structures. The contrast (γ) of the photosensitive polymers was obtained by measuring film thickness after developing as a function of exposure dose. Equation 2.1 describes the relationship between exposure dose and contrast [53].

$$\gamma = \frac{1}{\log_{10}\left(\frac{D_{100}}{D_0}\right)} \quad (2.1)$$

D_{100} is the exposure dose at which none of the photodefined material is removed upon exposure to developer, and D_0 is the exposure dose at which all of the photodefined material is removed. Mathematically γ represents the slope of the linear region of a plot of normalized film thickness versus the log of exposure dose.

2.2.3 Residual Stress

Stoney's equation shown in equation 2.2 is used to relate the residual stress of a film to the change in the radius of curvature of the supporting substrate [54].

$$\sigma = \left(\frac{E}{1-\upsilon}\right)\frac{h^2}{6Rt} \quad (2.2)$$

where σ is the residual stress, $E/1-\upsilon$ is the biaxial elastic modulus of the substrate (1.805 x10^{11} Pa for <100> oriented silicon), t is the thickness of the film, and h is the substrate thickness. R is the reduced change in radius given by:

$$\frac{1}{R} = \frac{1}{R_2} - \frac{1}{R_1} \quad (2.3)$$

R_1 is the radius of curvature of the uncoated substrate and R_2 is the radius of curvature of the substrate after film coating and processing. According to Klein, Stoney's equation correctly represents the average biaxial stress acting within a film deposited on a substrate for film thicknesses less than 10 % of the substrate thickness [55].

2.2.4 Elastic Modulus

Dielectric materials must also provide mechanical support for metal connections. A lower elastic modulus material will exhibit greater deformation under stress. It is desirable for deformations to be in the elastic region and plastic deformation is undesirable. Nano-indentation is a depth sensing technique used to characterize mechanical properties such as reduced modulus and hardness. This technique has been used to characterize materials such as ceramics [56], biological specimens [57], and metallic alloys [58-59]. However, the nano-indentation of polymers is particularly challenging due to their significant compliance and low hardness [60], viscoelastic or viscoplastic response [61], and resulting strain-rate dependence of deformation [62].

The hardness is defined as applied load per unit area of indentation. For a maximum load (P_{max}) and a projected contact area ($A(h_c)$) as a function of contact depth (h_c), the indentation hardness is defined in equation 2.4 [63].

$$H = \frac{P_{\max}}{A(h_c)} \quad (2.4)$$

The gradient of the initial portion of the unloading stiffness curve provides the elastic parameters of the material given that the creep effects are dissipated through a hold [63]. The gradient or unloading stiffness (S) is given by:

$$S = \frac{dP}{dh} \quad (2.5)$$

A key challenge in interpreting indentation results is the determination of $A(h_c)$. Oliver and Pharr[63] estimate h_c for a geometrical constant (ε) from:

$$h_c = h_{\max} - \varepsilon \frac{P_{\max}}{S} \quad (2.6)$$

The value of E_r is expressed by equation 2.7 [63-65].

$$\frac{1}{E_r} = \frac{\left(1 - v_m^2\right)}{E_m} + \frac{\left(1 - v_i^2\right)}{E_i} \quad (2.7)$$

Where E and v are the elastic modulus and the Poisson's ratio, respectively, and the subscripts m and i refer to the material and the indenter respectively. The relationship between S and E_r is shown by equation 2.8 [63].

$$S = 2aE_r = \frac{2\beta E_r \sqrt{A}}{\sqrt{\pi}} \quad (2.8)$$

Where β is a constant and the ideal area function of a Berkovich tip is represented by $A=24.5h_c^2$. For an indenter with a tip imperfection, the area is described by equation 2.9[63].

$$A(h_c) = 24.5h_c^2 + \sum_{i=0}^{7} a_i h_c^{\frac{1}{2^i}} \quad (2.9)$$

The extended coefficients (a_i) for the area function are typically found by performing indents over a range of depths in a material of known modulus. Fused silica (quartz) is commonly used as a standard because its elastic modulus does not vary significantly with depth and does not contain a surface layer such as a surface oxide in metals [66]. However, researchers have shown that it is necessary to calibrate with a standard having a modulus similar to the sample so that the area function obtained from the standard is valid over the indentation depths of the sample [67]. A polycarbonate calibration standard (Hysitron Inc.) with a modulus of 3.1 GPa was used to calculate the area function for the measurements presented in this work.

2.2.5 Dielectric Constant

A dielectric material is a non-conducting substance that is often used to electrically isolate conducting metals within a device. An important property of a dielectric is its ability to support an electrostatic field while releasing minimal energy in the form of heat. To minimize the loss of signal strength along the length of a metal line, an insulating material is needed that has a low capacitance and inductance and therefore a low dielectric constant. Under an alternating current, charge may be carried through the dielectric with a current proportional to the complex dielectric constant of the insulating material, ε*, as shown in equation 2.10 [68].

$$J = i\omega\varepsilon^{*}\varepsilon_0 \, E \quad (2.10)$$

Where ω is 2πf, where f is the frequency, ε_0 is the permittivity of vacuum (8.85×10^{-14} farads/cm) and E is the electric field. The complex dielectric constant consists of both the real and imaginary parts as shown in equation 2.11 [68].

$$\varepsilon^{*}(\omega) = \varepsilon'(\omega) - i\varepsilon''(\omega) \quad (2.11)$$

Where ε' is the relative permittivity of the material and ε'' is the relative loss tangent; both relative to vacuum. The relative permittivity is a measure of the electrical polarization of species under an electric field, and the loss tangent is a measure of the energy required for molecular and ion motion in the presence of the electric field. Both relative permittivity and the loss tangent are functions of the material, frequency, temperature, and orientation of the material. Dielectric measurements were performed by fabricating parallel-plate capacitors. In a parallel plate capacitor, capacitance (C) is given by equation 2.12 [68].

$$C = \frac{\varepsilon_0 \varepsilon' A}{t} \quad (2.12)$$

Where A is the area and t is the separation between plates. Capacitance between the plates is proportional to the permittivity of the dielectric layer. Signal delay in a line due to a nearby line is directly proportional to the product of the resistance of the metal line and the capacitive coupling between metal lines. Therefore, a material with a low dielectric constant reduces delay for constant line spacing or can allow closer line spacing at constant delay times.

CHAPTER 3

INTRODUCTION TO ADVANCED MICROELECTRONICS PACKAGING

Extensive research has been devoted to manufacturing high performance ICs. However, these ICs need to be connected to other components on a printed circuit board to form electronic products. This chapter provides a basic overview of board level and chip to board packaging challenges to motivate the research presented in this thesis. Packaging is defined as the bridge that connects the integrated circuit with other components on a system level [6]. The package protects, powers, cools ICs and also serves as an electrical and mechanical connection to other system components. The conductive paths carrying the digital signals are known as interconnects and include the entire electrical pathway away from the chip to the component receiving the signal. To enable fast and reliable processors, advances must be made in the interconnections on the PCB and also in the interconnections from the chip to the printed circuit board.

3.1 Board Level Interconnects

3.1.1 Transmission Line Fundamentals

Previously it had been possible to ignore losses on the PCB because systems operated at low frequencies. However as frequencies continue to increase, complex interactions occur in the transmission line causing degradation in performance. Since the conductor is not infinitely conductive and the dielectric is not infinitely resistive, loss arises in the signal. As a result, routing high frequency signals off-chip is challenging, and low loss structures are needed to enable fast interconnections between system

components. There are three major types of losses that occur in transmission lines: conductor loss, dielectric loss, and radiation loss.

Conductor loss primarily depends on the resistivity of the conductor and the total area in which the current is flowing. As the signal passes through the conductor, heating occurs from the resistance of the conductor and conductor loss also arises from the skin effect. As the frequency increases in alternating current (AC), the free movement of electrons in the conductor is restricted, and the electron flow shifts to the surface of the conductor. At frequencies above 100 MHz, almost all of the electrons flow on the surface of the conductor. As frequency continues to increase, the effective cross-sectional area decreases, and resistance increases since it is inversely proportional to the cross-sectional area. Therefore, power loss increases as frequency increases, and conductor loss scales with the square root of frequency. However, power loss in the conductor decreases as metal conductivity increases. Copper is the industry standard for transmission lines due to its high conductivity, good electromigration resistance, and cost effectiveness [6].

Dielectric loss occurs due to power being dissipated as heat within the dielectric. In AC mode, the molecules in the dielectric attempt to align to the alternating electric field. During this rotation, electrical energy is converted to heat and lost. These losses cause inefficiency and also impact the impedance of the overall circuit. The lost energy in the dielectric is characterized by the loss tangent which is a ratio of the lost energy to stored energy. A vacuum is the only medium where the loss tangent reaches unity. The loss in the dielectric scales linearly with frequency and at operating frequencies above 10 GHz the loss in the dielectric becomes the dominant loss contribution [69]. The inclusion

of an air gap can mitigate dielectric loss allowing the signal to propagate over longer lengths or at higher frequencies [7]. Additionally, the low dielectric constant of air lowers the loss contributions from the conductor and increases the signal propagation velocity reducing delay [7].

Radiation losses also increase with frequency and are due to leakage loss rather than heat dissipation of power. The stray inductances and capacitances can have a large impact on the performance of the overall circuit. The signal on one transmission line can affect and be affected by other signals. Confining the electromagnetic fields with metallic shielding can reduce radiation losses.

3.1.2 Motivation for Ultra-Low Loss Transmission Lines

Because of the large data requirements of high performance computing systems, bandwidth needs for future systems are expected to expand in the next decade. As the frequency of I/O connections increases, there will be a need for high speed connections between system components and the network that do not hinder circuit performance. Advanced connections are especially needed for systems with large distances between components where signal strength can degrade considerably. Both optical and electrical connections are used for high-speed communication between chips or networks. Optical links are preferred for long transmission lengths because optical fibers have low loss. Additionally, a fiber can transmit multiple data sets and therefore attain higher data rates than electrical connections. However at short transmission lengths, integration of optical connections can be challenging due to the rigorous alignment tolerances and losses at sharp routing angles [70].

Implementing electrical connections lessens integration challenges, but signal loss must be reduced to be viable. According to the ITRS off-chip operating frequencies will exceed 9.5 Ghz by 2010 and 88 Ghz by 2020 [15]. The ITRS states that to enable high performance electronic systems, high density and high bandwith off-chip interconnects are necessary. To achieve these goals, electrical interconnects need to reduce losses in the dielectric substrate, losses due to reflections and discontinuities, and minimize crosstalk noise. At these high operating frequencies, the power loss dissipated limits the maximum distance the signal can be routed at the necessary signal to noise ratio. Furthermore, as channel density increases to maximize the data rate, cross-talk and radiation losses become considerable. Low loss structures are needed for high frequencies, long transmission lengths, or high density applications and must have electrical shielding and insulators that provide low capacitance and inductance.

3.1.3 Air Dielectric Transmission Lines

Traditionally, transmission lines on printed circuit boards are microstrip lines shown in Figure 3.1 that are fabricated with copper and an insulating dielectric.

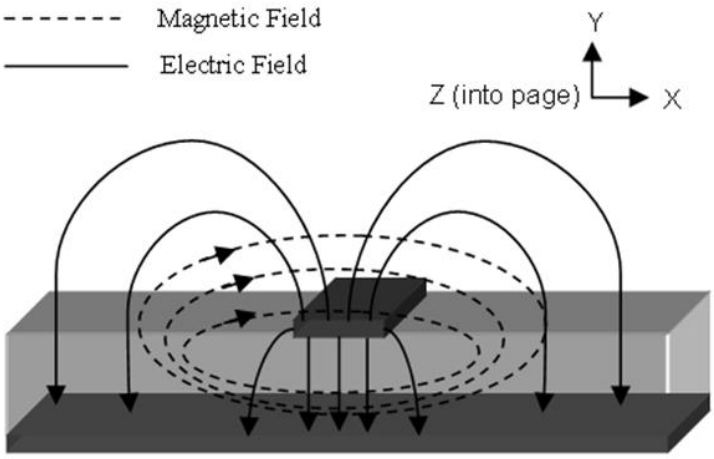

Figure 3.1: Schematic of electrical and magnetic fields for a microstrip transmission line

The top copper layer serves as the conductor, and the bottom conductor serves as the ground. The signal does not merely propagate on the conductor, but between the conductor and the reference plane in the form of an electric and a magnetic field. Since the electric field extends above the copper signal line into the air, it benefits from the low loss properties of air, but the structures lose this benefit if they are encapsulated. Therefore, they are only beneficial for top layers of the printed circuit board, and loss in the dielectric layer is still significant.

Lee et al. fabricated dielectric post air-gap microstrip lines to mitigate the loss in the dielectric, and the structure is shown in Figure 3.2 [71]. The air gap was formed using a sacrificial layer of photo-resist, but further encapsulation of this structure is not possible.

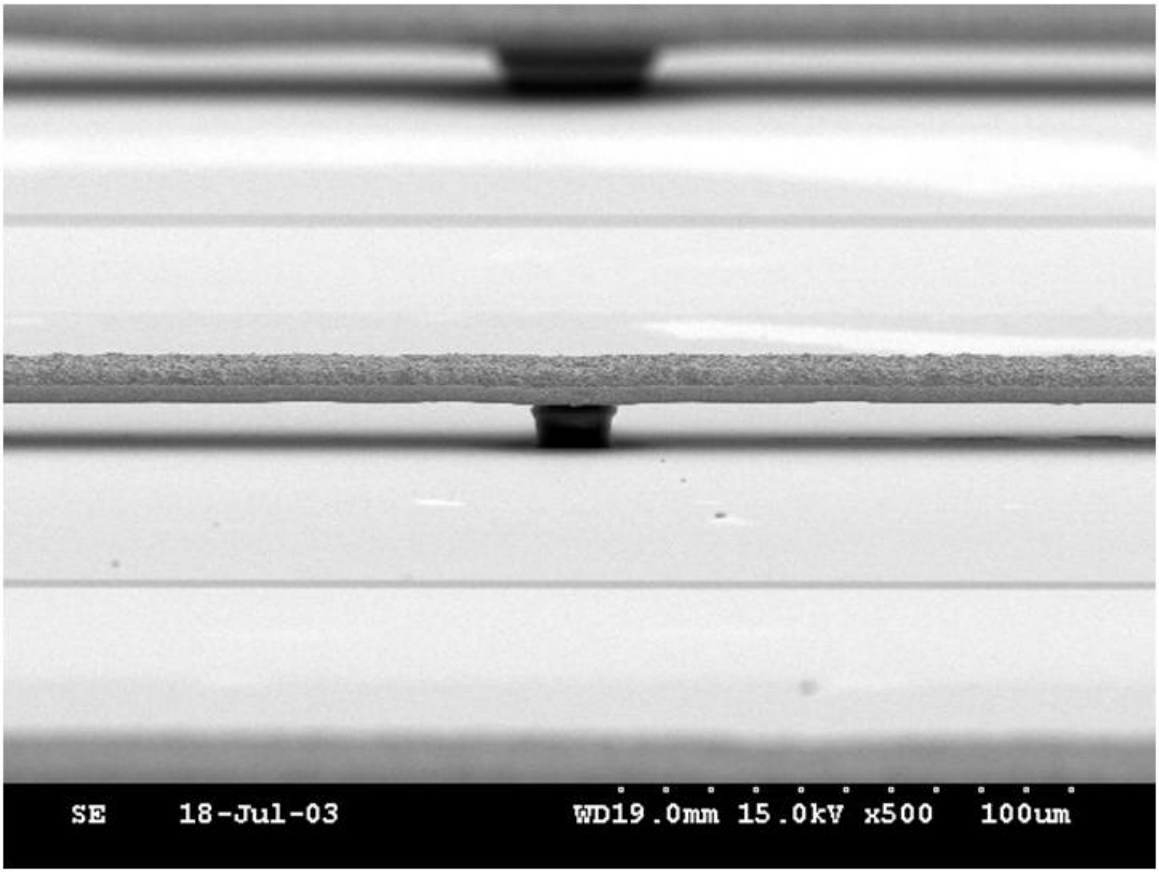

Figure 3.2: Dielectric post air gap microstrip line [71]

Yook et al. fabricated a shielded air cavity transmission line shown in Figure 3.3[72]. The signal line is supported by a dielectric post, and shielding is provided by anodized alumina. As with the dielectric post air gap microstrip line, this structure could only be incorporated on the top layers of the PCB.

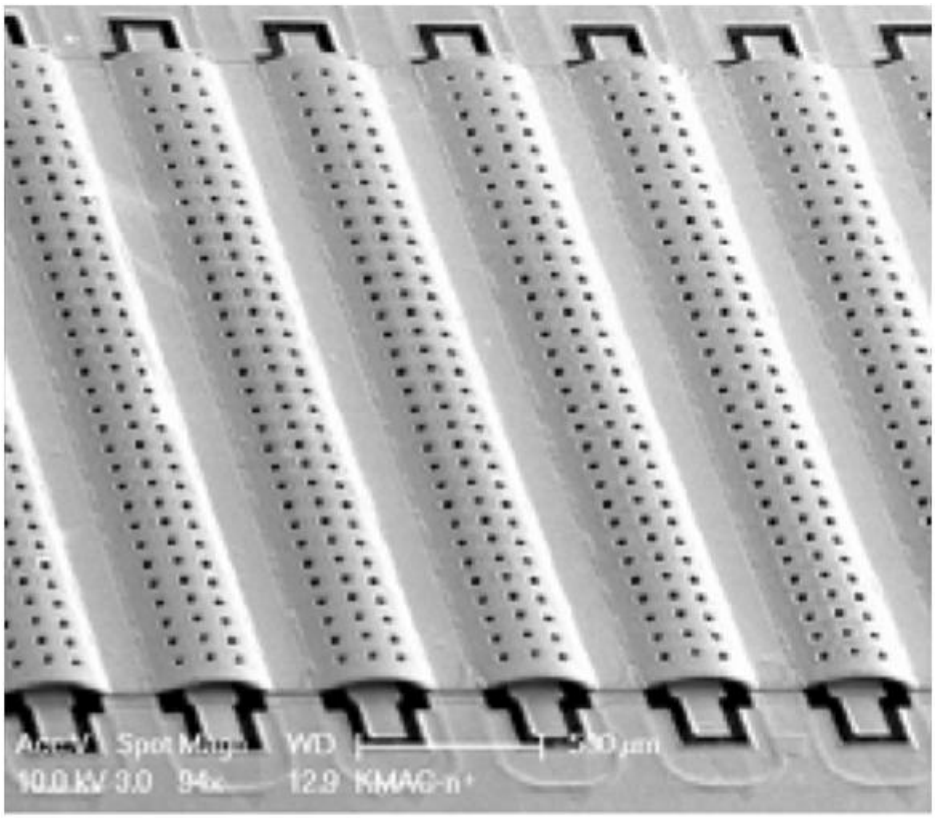

Figure 3.3: Shielded air cavity transmission lines [72]

Coaxial transmission lines shown in Figure 3.4 are commonly used in radio frequency (RF) systems because they contain the propagating electromagnetic signal and consequently do not radiate noise or pick up other signals in their vicinity.

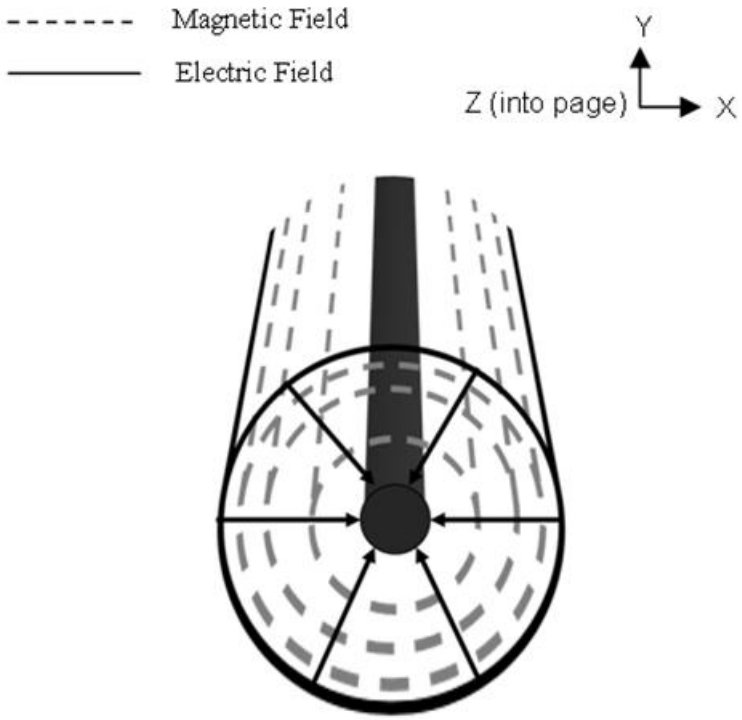

Figure 3.4: Schematic of electrical and magnetic fields for a coaxial transmission line

Fabricating a coaxial line using traditional microelectronics fabrication techniques is challenging due to the three dimensional structure of the coax. Researchers have demonstrated coaxial lines on a monolithic scale and have used complex photolithographic techniques to fabricate half-coaxial structures [73-74]. Natarajan et al. fabricated a polyimide core micro coaxial transmission line shown in Figure 3.5 [74].

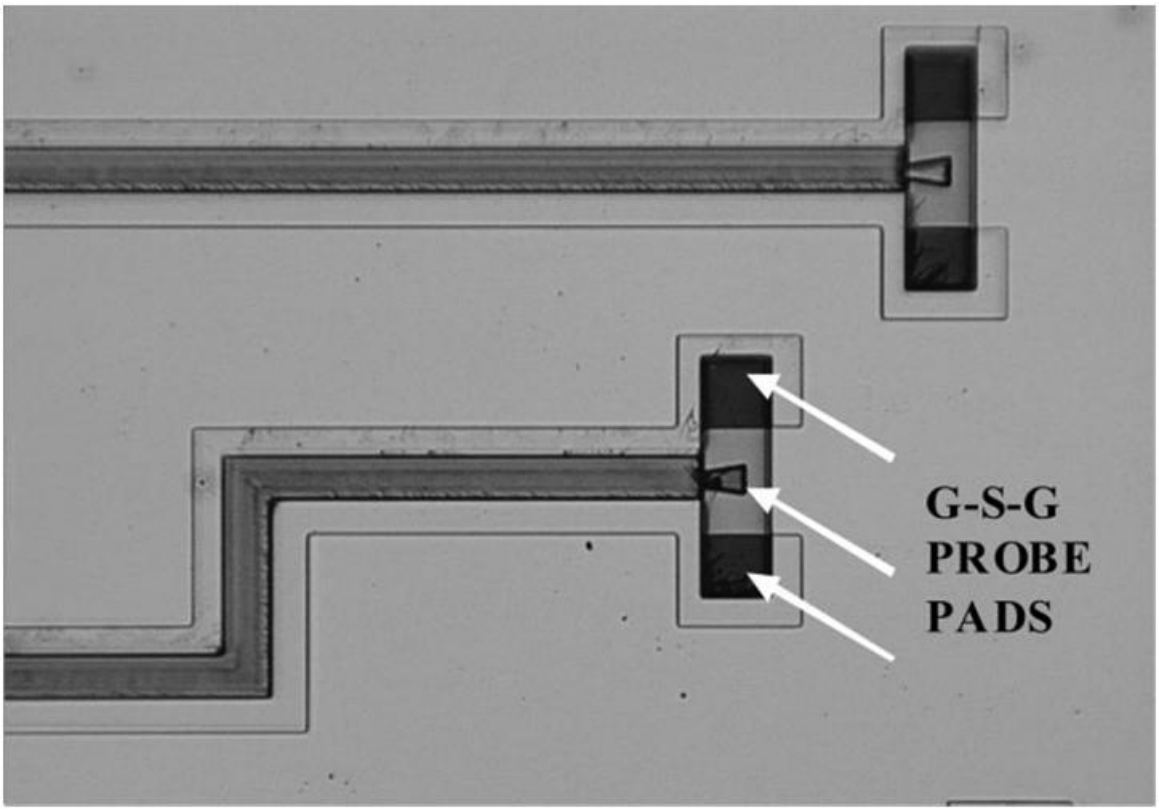

Figure 3.5: Fabricated straight and meander micro coaxial transmission line [74]

Due to the shielded geometry, cross-talk noise and radiation losses are reduced, but these structures did not incorporate air dielectric layers below the signal conductor and therefore, have a high dielectric loss in the polyimide and substrate.

3.2 Chip to Substrate Interconnects

3.2.1 Types of Chip to Substrate Interconnects

Chip to substrate interconnects provide an electrical and mechanical link between the chip and the substrate. The two most common methods to assemble the chip to the substrate are wire bonding and flip chip bonding which are illustrated in Figure 3.6 and Figure 3.7 respectively [6].

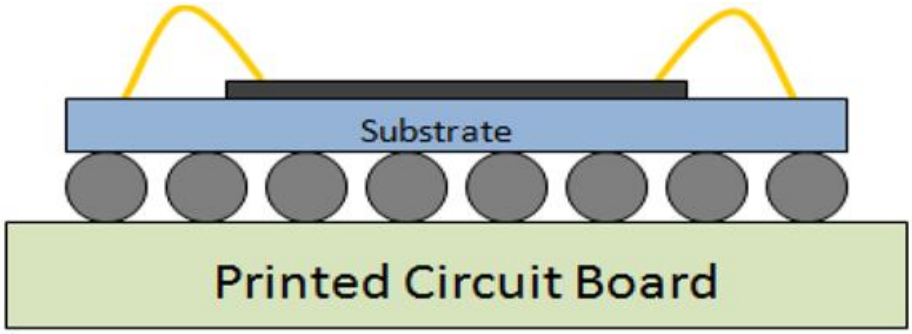

Figure 3.6: Chip to substrate wire bonding

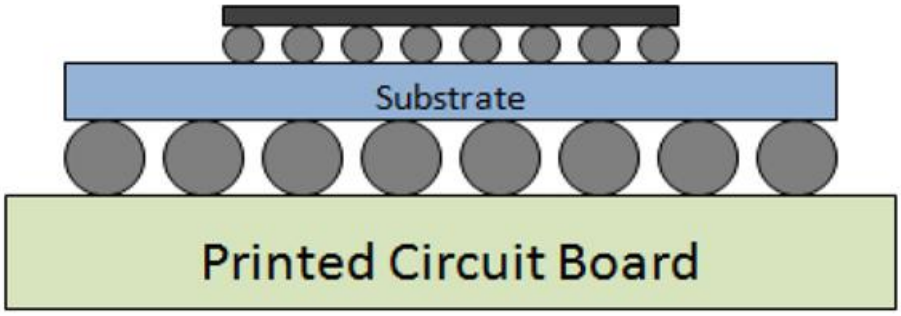

Figure 3.7: Chip to substrate flip-chip interconnection

The flip chip configuration is preferred for high performance systems because the ball grid array (BGA) in the flip chip configuration has a much higher I/O density than wire bonding. Furthermore, the flip chip connections are considerably shorter than the wire bonds lowering interconnect latency and parasitic characteristics [75]. Also, the flip chip configuration offers better thermal characteristics since an external heat sink can be directly added above the chip to remove heat.

A connection can be directly made from the chip to the printed circuit board called chip on board (COB) as shown in Figure 3.8.

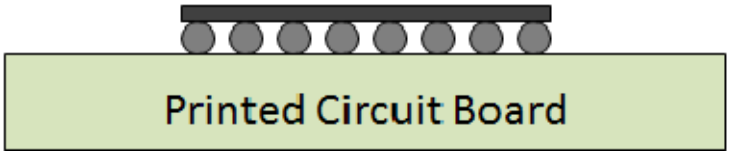

Figure 3.8: Chip on board flip-chip interconnection

The COB process requires less board space, and the direct interconnection between the die and board improves electrical performance [76-78]. However, the substrate allows for a higher number of I/O and can allow integration of a heat-sink which is important for high power chips.

Solder balls are generally used to make the mechanical and electrical connections from the chip to the substrate and the substrate to the board as shown in Figure 3.7. The melting point of solder and its ability to adjust to lateral mis-alignment and nonplanar surfaces makes it compatible with traditional packaging [79-80]. However, solder must be integrated with connections on the board, and copper-tin intermetallics have poor mechanical properties which compromises mechanical integrity.

3.2.2 Motivation

The ITRS dictates that new, cost effective high performance chip-to-substrate interconnects are necessary for high frequency signals, low parasitic power/ground, and high bandwidth optical I/O approaches [15]. As the pitch and size of the solder balls decreases to keep pace with device scaling, solder based connections face many challenges. The CTE of the silicon chip is approximately 3ppm/ºC while the CTE for a PCB such as FR-4 is approximately 15 ppm/ºC [6]. Due to the low mechanical strength of solder, a silica particle filled epoxy material is used as a stress buffer [6]. The ITRS projections for area-array I/O interconnects are 7,000 per cm^2, 10,000 per cm^2, and

14,000 per cm^2, in 2010, 2015, and 2020 respectively (based on minimum pitch requirements) [15]. To meet the increase in I/O interconnect density, the bump-to-bump pitch and solder ball diameter must decrease. The solder connection is limited to an aspect ratio of roughly unity (1:1 height : diameter) making high profile, large stand-off distance chip-to-substrate connections very difficult to fabricate. As the stand-off distance between the chip and substrate decrease, processing with under-fill material becomes difficult. To achieve high I/O density, high aspect ratio connections are needed that can accommodate the stress between the silicon chip and printed circuit board [9].

Copper electrical connections from the chip to the substrate are an attractive solder-free option. An all-copper chip to substrate connection would provide high conductivity electrical connections, excellent resistance to electromigration, and avoid the formation of brittle intermetallics [8]. Copper wiring could then be incorporated as the wiring through the entire package and printed circuit board. Using one metal would reduce reflection loss and impedance mismatch, while eliminating the formation of brittle intermetallic compounds. Also because copper has a much higher yield stress and elastic modulus than tin based solder materials, mechanically complaint chip to substrate connections can be achieved with a high aspect ratio. Fabricating high aspect ratio connections would eliminate the need for under-fill, reducing processing steps and dielectric loss. However, patterning techniques are necessary that can create structures on the order of 10:1 (height to width) aspect ratios which is difficult to achieve with traditional photolithography.

3.2.3 Improved Mechanical Compliance Structures

In order to improve the mechanical compliance of solder based structures, researchers have developed copper pillars with solder caps as shown in Figure 3.9 [81-83].

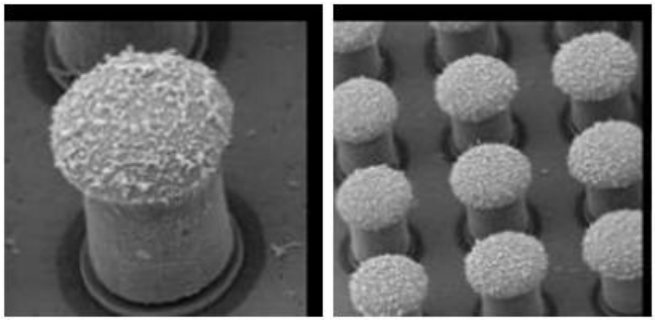

Figure 3.9. Copper Pillars capped with solder [83]

Placing the solder bump on the copper pillar rather than at the surface of the chip or package creates a more mechanically reliable connection. Copper is a higher yield stress material, and placing it at the highest stress point during thermal cycling reduces the likelihood of thermo-mechanical failure. Furthermore, the copper pillar increases the aspect ratio of the connections allowing finer pitch geometries with a greater stand-off distance between the chip and substrate. Under-fill is necessary for these structures because brittle intermetallics will form at the copper tin interface. The higher stand-off distance makes it possible to flow under-fill in between the connections and have a reliable connection. Although this structure is an improvement to traditional solder ball connections, it is still limited electrically and mechanically by the properties of solder. Other capped structures have also been developed, but their implementation is dependent on application specific requirements.

Work has also been conducted to fabricate mechanically compliant, high yield stress metal pillars [84]. By fabricating a metal conductor around a polymer pillar, Aggrawal et al. showed that the mechanical compliance of the interconnect can be improved [84]. As shown in Figure 3.10, a polyimide core with a copper shell was fabricated, and this structure had a greater compliance than solid copper pillars of the same dimension [84].

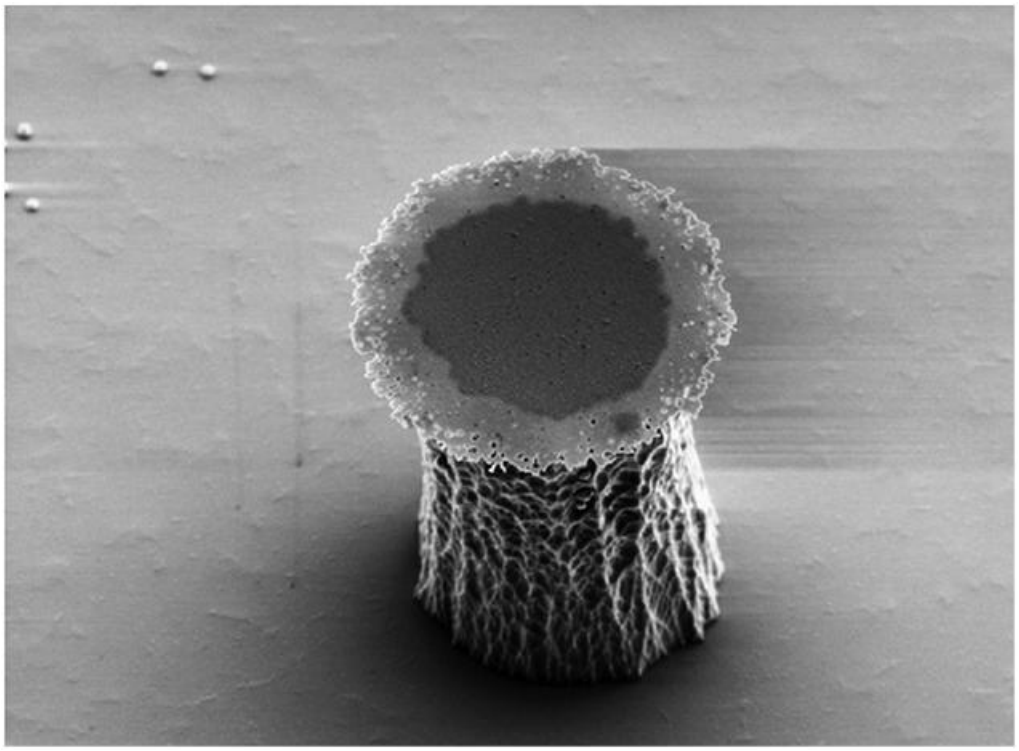

Figure 3.10. Metal clad polymer pillar [84]

The copper shell does not have to be thick since the signal will not penetrate deep into the metal due to the skin effect. The roughness of the structure arises from the fact that the high aspect ratio polymer pillars were fabricated using plasma RIE. This roughened polymer surface enabled good adhesion with electro-less copper. However,

plasma etching of polymer structures at these length scales has poor throughput and is not a cost effective packaging technology.

CHAPTER 4

ULTRA LOW LOSS COAXIAL INTERCONNECTS

4.1 Introduction

In this work, sacrificial polymers and the unique three dimensional patterning capabilities of imprint lithography have been used to fabricate the ultra-low loss transmission lines shown in Figure 4.1(a) and (b).

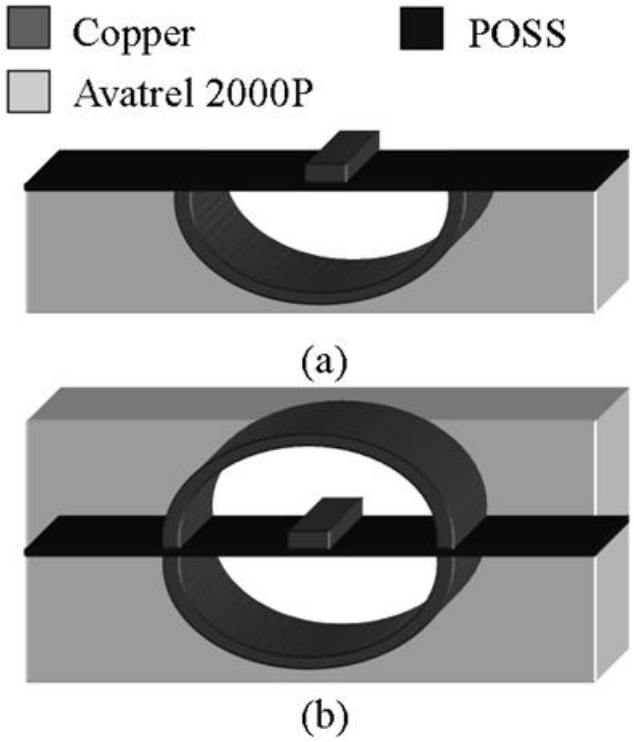

Figure 4.1: Schematic of air clad (a) half-coaxial and (b) coaxial transmission line

The inclusion of an air gap can mitigate dielectric loss allowing the signal to propagate over longer lengths or at higher frequencies [7]. Additionally, the low dielectric constant of air lowers the loss contributions from the conductor and increases the signal

propagation velocity reducing delay. The use of sacrificial polymers and imprint lithography is compatible with board processing, and this process has similar masking and registration steps to traditional transmission line fabrication. The imprint process produces uniform dielectric material thicknesses while improving line definition allowing lower tolerances for impedance control. Development of this process for advanced packaging applications could advance IC performance capabilities with high throughput and yield, while maintaining low cost.

4.2 Experimental and Material Selection

Schematics of imprint stamp fabrication and transmission line fabrication are provided in Appendix A. To create the semicircular stamp for imprinting, a full seed layer of Ti/Au/Ti (300Å/3000Å/300Å) was sputtered using the Unifilm sputtering system onto glass wafers. A 1.5 μm layer of oxide was deposited using the Unaxis PECVD, and 50-100 μm rectangular lines were photo-patterned using NR-9 (Futurexx). The NR-9 was spin-coated to a thickness of 30 μm and soft baked at 110°C for 30 minutes. The resist was photo-patterned at 400 mJ/cm^2 using the Karl Suss MA-6 Mask Aligner which uses a 350 W mercury lamp that exposes across the spectrum 230 nm to 400 nm. The sample was then post-exposure baked for 20 minutes at 75°C and developed in RD-6 (Futurexx) to define rectangular trenches. The oxide and titanium in the exposed region was wet etched back using buffered oxide etch solution, and tin/lead solder lines were electroplated. The photo-resist was stripped in acetone, and flux (Rector Seal) was used to reflow the lines at 230°C to achieve the semi-circular geometry. The stamp was coated with Teflon AF [85] and soft baked at 115°C for 10 minutes.

Imprint materials were selected for their ability to replicate and retain mold patterns, and Avatrel 2000P serves as the primary imprint material for this structure. Avatrel 2000P is a polynorbornene based negative-tone, photosensitive, dielectric material developed by Promerus LLC. The general chemical structure is illustrated in Figure 4.2 (a). The polymer is a random copolymer in which each of the seven-member norbornene rings on the backbone is functionalized with either decyl or epoxide side groups. The properties of the polymer film can be controlled by varying the ratio of decyl to epoxide side groups that are substituted directly to the polymer backbone. The polymer has a dielectric constant of 2.5 and a glass transition temperature above 250°C[86].

To fabricate the transmission line, a polynorbornene polymer Avatrel 2000P was spin coated to a thickness of 30 μm and soft baked at 100°C for 15 minutes. The semi-circular stamp was imprinted into the soft baked Avatrel 2000P film at 110ºC and 45 bar for 60 seconds using the Obducat Imprint Lithography System. The imprinted polymer sample was blanket exposed to 365 nm UV light at 300 mJ/cm^2 using the Optical Associates Inc. Mask Aligner and post-exposure baked in an oven at 100°C for 20 minutes. A seed layer of Ti/Cu (300Å/3000Å) was sputtered using the CVC DC Sputterer and electroplated to 1.5 μm. Mechanical polishing with 0.05 μm alumina slurry was used to remove copper from the field leaving copper solely in the trench. The sample was rinsed briefly in a 3% sulfuric acid and 3% hydrogen peroxide solution to remove copper oxide and debris.

Polypropylene carbonate (PPC) serves as a place holder for the air cavities because it can be decomposed thermally. PPC, shown in Figure 4.2(b), is an aliphatic polycarbonate produced through copolymerization of carbon dioxide and propylene

oxide. The thermoplastic material has an elastic modulus of 2 GPa, a dielectric constant of 3, and a glass transition temperature of 40°C [87]. PPC can be used as a sacrificial material, and complete thermal decomposition of PPC occurs at 250ºC [87]. The addition of a photo-acid generator has been shown to decrease the temperature of thermal decomposition [88]. A 3% weight loading of photo-acid generator was added to the PPC formulation. The primary volatile products of decomposition are acetone and carbon dioxide and can permeate through many dielectrics at the decomposition temperature [89].

A thick layer of PPC was spin-coated on the imprinted sample and soft baked at 115°C for 15 minutes. Teflon was coated onto a blank glass slide and baked at 115°C for 10 minutes. The flat glass slide was used to press the sacrificial PPC material into the trench and planarize the field at 60ºC and 45 bar for 180 seconds in the Obducat Imprint Lithography System. The sample was blanket exposed to 365 nm UV light at 1000 mJ/cm^2 using the Optical Associates, Inc. Mask Aligner, and the PPC was allowed to decompose from the field region on a hotplate at 180°C for 15 minutes.

A photodefineable epoxycyclohexyl polyhedral oligomeric silsesquioxane (POSS) (Hybrid Plastics Inc.), shown in Figure 4.2 (c), was used for suspending the transmission line in the air cavity due to its mechanical strength coupled with its optimal strain and stress properties. The epoxy functionalized dielectric material along with an iodonium photo-acid generator and a 365 nm sensitizer yields photo-definable, highly cross-linked films [90]. POSS was spin-coated onto the sample to a 3 μm thickness and soft baked for 6 minutes at 85°C. The sample was exposed to UV light at 400 mJ/cm^2 using the Optical Associates Inc. Mask Aligner. A seed layer of Ti/Cu/Ti (300Å/3000Å/300Å) was sputtered using the CVC DC Sputterer. The sample was then photopatterned with NR-9

to a 15 μm thickness and soft baked at 110°C for 30 minutes. The resist was aligned and photopatterned at 400 mJ/cm^2 using the Karl Suss MA-6 Mask Aligner; the sample was post-exposure baked for 20 minutes at 75°C, and developed in RD-6 (Futurexx) to define rectangular trenches. The titanium in the exposed region was wet etched back using buffered oxide etch solution, and copper lines were electroplated. The photo-resist was stripped in acetone, and the titanium seed layer was etched using buffered oxide etch solution, and the copper seed layer was etched back in a 3% sulfuric acid and 3% hydrogen peroxide solution.

The PPC in the trench was slowly decomposed in a nitrogen furnace purged to 1 ppm oxygen. The chosen stepwise recipe maintains the decomposition at 0.25 wt % per minute. The sample was ramped to 140°C at 1°C/min and held at temperature for 4 hours; ramped to 160°C at 1°C/min and held at temperature for 2 hours; ramped to 180°C at 1°C/min and held for 5 hours. The furnace was allowed to cool slowly by natural convection to room temperature.

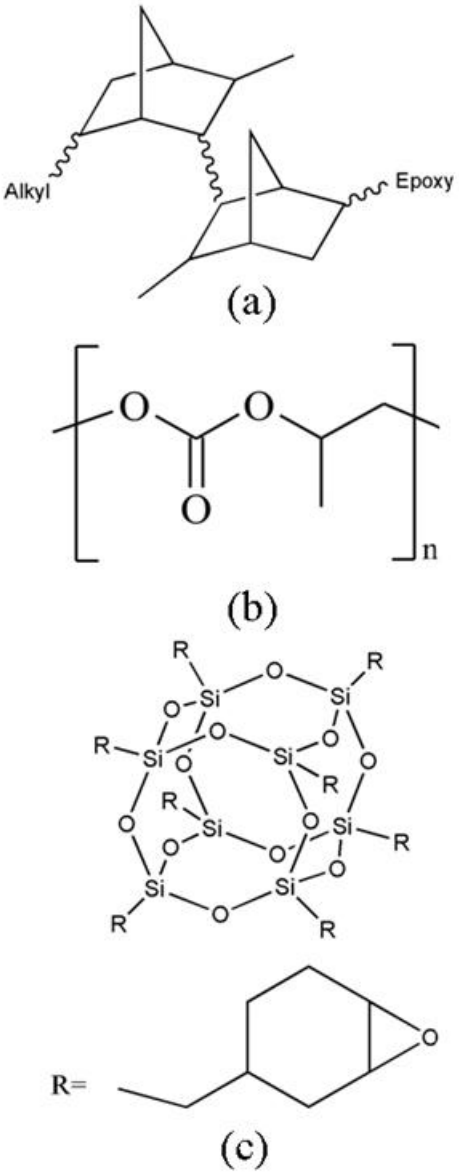

Figure 4.2: Chemical structures of polymers used in fabrication. (a) Avatrel 2000P (b) Polypropylene carbonate (c) Epoxycyclohexyl POSS

Quasi-static nano-indentation was conducted using a Hysitron Triboindenter. Indentations on Avatrel 2000P polymer samples were performed with a Berkovich tip and loaded to 1000μN over five points per sample. A maximum drift rate of 0.1 nm/s of

was set for the experiment and was automatically determined over a 40 s period. The tip was loaded to maximum load in 10 s, held for 10 s, and unloaded in 2 s. The load–depth curves were analyzed using the Oliver–Pharr model to obtain the reduced modulus (E_r) and the hardness (H)[63]. Indentations on air cavities were performed using a 60° conospherical tip and samples were ramped to a force of 8750 μN in 10 s and then unloaded in 10 s.

To complete the top portion of the copper shielding, Avatrel 2000P was spin coated to a thickness of 30 μm and soft baked at 100°C for 15 minutes. The semi-circular stamp was imprinted into the soft baked Avatrel 2000P film at 110ºC and 45 bar for 60 seconds using the Obducat Imprint Lithography System. A seed layer of Ti/Cu (300Å/5000Å) was sputtered using the Unifilm Sputterer and electroplated to a total thickness of 1.5 μm. The sample was then photopatterned with AZ-4620 (AZ Electronic Chemicals) to a 10 μm thickness and soft baked at 90°C for 10 minutes in an oven. The resist was aligned and photopatterned at 900 mJ/cm^2 using the Karl Suss MA-6 Mask Aligner and developed in AZ-400K (AZ Electronic Chemicals). The copper seed layer was etched back in a 3% sulfuric acid and 3% hydrogen peroxide solution, and the resist was stripped in acetone. The top portion of the copper shielding was bonded with the half-coaxial line in the imprinter at 160°C, 15 bar, for 180 seconds. The sample was then cured in a furnace with a ramp to 160°C at 5°C/min and held at temperature for 1 hour. The furnace was allowed to cool slowly by natural convection to room temperature.

For samples with the photo-resist release layer, NR-9 was spin-coated to a thickness of 30 μm and soft baked at 110°C for 30 minutes. Processing then followed the procedure dictated for the top portion of the copper shielding. To release the top wafer

from the bonded transmission line, the sample was placed in acetone in an ultra-sonic bath for 3 minutes. For samples with the photo-sensitive tape release layer, the UC-120m-120 (Furukawa Electric) UV sensitive tape was used. The tape was bonded onto a glass substrate in the imprinter at 125°C, 15 bar, for 180 seconds and processing then followed the procedure dictated for the top portion of the copper shielding. To release the top wafer, the sample was exposed to UV light at 1000 mJ/cm^2 using the Optical Associates Inc. Mask Aligner. For samples coated with Parylene C as an imprint anti-adhesion layer, samples were conformally coated through a vapor phase deposition process in the SCS Labcoater PDS 2010.

A Zeiss Ultra 60 and Hitachi 3500H were used to obtain scanning electron microscope (SEM) images of the processed films. Thermal stability characterization was conducted via thermal gravimetric analysis (TGA) using a TA instruments Q50. The materials were heated to 300°C using a 1°C/min ramp rate and a nitrogen atmosphere.

4.3 Results and Discussion

To begin building the ultra-low loss transmission line, an imprint stamp was fabricated to create the base of the coaxial structure. Photolithography could have been used to pattern the base of the structure. However, straight lines with sharp corners are electrically unfavorable at terminations and discontinuities where reflections could occur, and these power losses become significant at high frequencies. To fabricate a semi-circular trench in the film, a stamp with a semi-circular line was made using solder. At temperatures above the melting point of the alloy and upon removal of surfaces oxides, solder will form a spherical shape in order to minimize its surface forces. By utilizing this behavior, tin-lead solder rectangular lines were electroplated and then reflowed to

achieve a rounded geometry. As shown in Figure 4.3, there is a small amount of surface roughness of the line, but this can be eliminated with further optimization of the reflow conditions or bath chemistry.

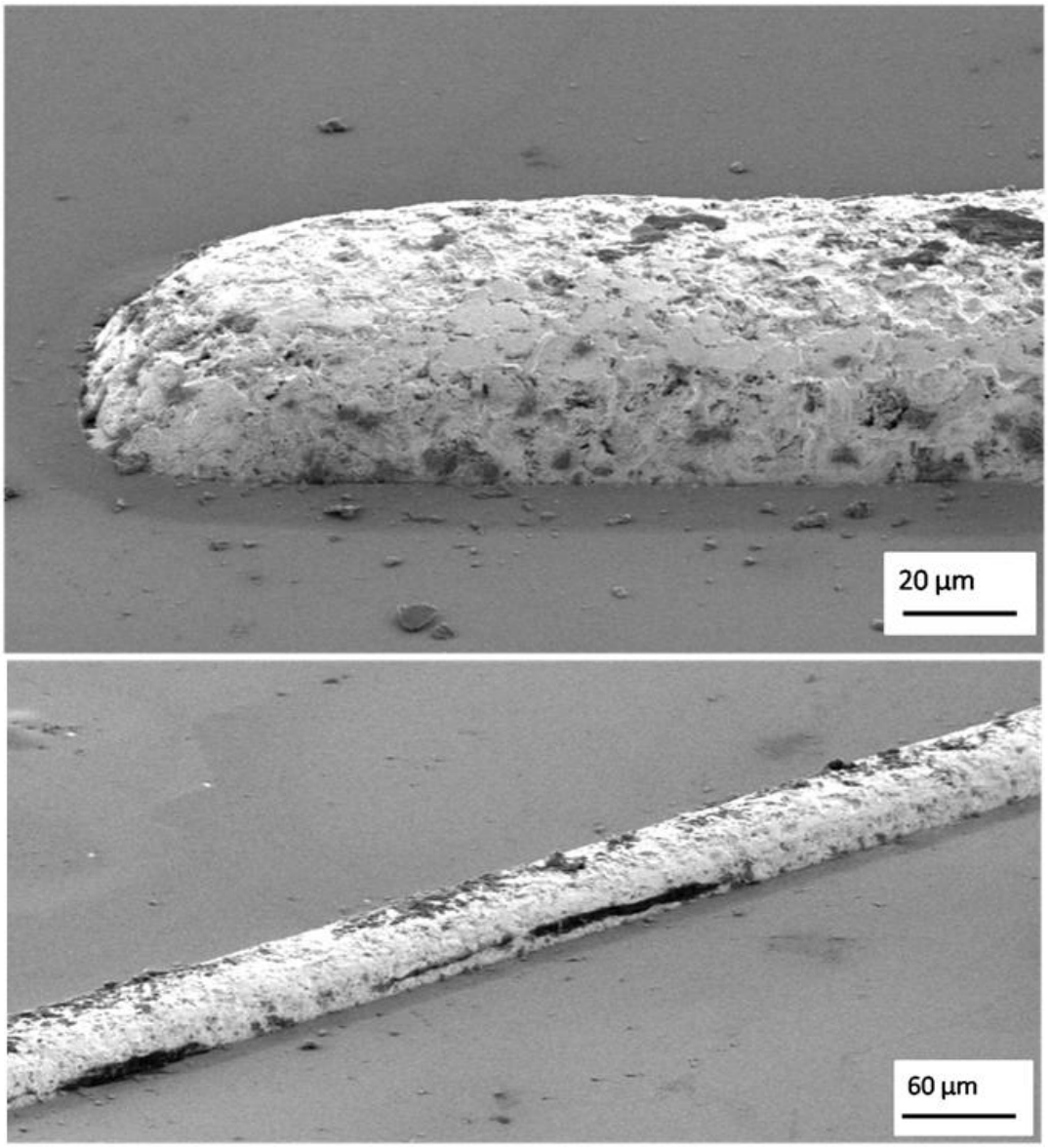

Figure 4.3: SEM images of 50 µm wide solder imprint stamp

The stamps were then coated with either Parylene C or Teflon AF to facilitate easy separation after imprinting. The negative-tone polynorbornene, Avatrel 2000P, serves as the base material for imprinting the trench because of its thermosetting properties and low dielectric constant. Avatrel 2000P polymer properties change during soft bake, UV exposure, post-exposure bake, and cure. To ensure proper pattern transfer into the dielectric, the optimal processing step for imprinting into the material had to be determined. Nano-identation experiments were conducted after each of the four processing steps to determine the optimal Avatrel 2000P process step for imprinting. For a fixed force of 1000 μN, the Berkovich tip displaced 998 nm after soft bake, but about 800 nm after exposure and post exposure bake, and 672 nm after cure. The mechanical properties were determined from force-displacement curves and are summarized in Table 1. The indentation depth data suggest that imprinting after polymer soft-bake displaces the most material for a given force. Therefore, imprinting was conducted after polymer soft-bake, because it requires the least force to displace material.

Table 4.1. Nano-indentation results of Avatrel 2000P for a fixed force of 1000 μN

Step	Depth (nm)	E_r (GPa)	H (GPa)
Soft-bake	998	0.56	0.018
Exposure	822	0.68	0.028
PEB	803	0.74	0.029
Cure	672	0.96	0.043

Ideally, imprint processes would occur at atmospheric pressure and ambient temperature. However, deforming polymers at these conditions is very time consuming. To enable mold filling, thermal imprint lithography is typically conducted at 50-70°C higher than the glass transition temperature of the imprint material [48]. Avatrel 2000P is a photosensitive dielectric that is processed at 100°C and cured at 160°C, and the glass transition temperature of the cured material is above 250°C. Operating at temperatures much higher than the photo-processing conditions can initiate thermal cross-linking of the material and as the indentation data suggested the cross-linked polymer chains are more difficult to displace than the non-cross-linked material. Differential Scanning Calorimetery (DSC) data is presented in Chapter 6 of soft-baked films of Avatrel 2000P. Although a clear T_g cannot be determined, the data suggests that thermal cross-linking of the polymer initiates at approximately 140°C. A range of temperatures and pressures were evaluated for best resolution of features, while avoiding thermal cross-linking of the material during imprinting. Imprinting at 110°C, 45 bar for 60 seconds into a soft baked film of Avatrel 2000P accurately transferred the stamp pattern and had good planarity in the non-imprinted region. This work was done concurrently with imprint work discussed in Chapter 6, and a more detailed discussion is provided in that chapter for determining the optimal imprint conditions for Avatrel 2000P and photosensitive materials. The sample was then blanket exposed to UV light and post exposure baked. As shown in Figure 4.4, the roughness of the imprinted feature replicates stamp roughness, but smoother lines can be achieved by refining the solder reflow conditions.

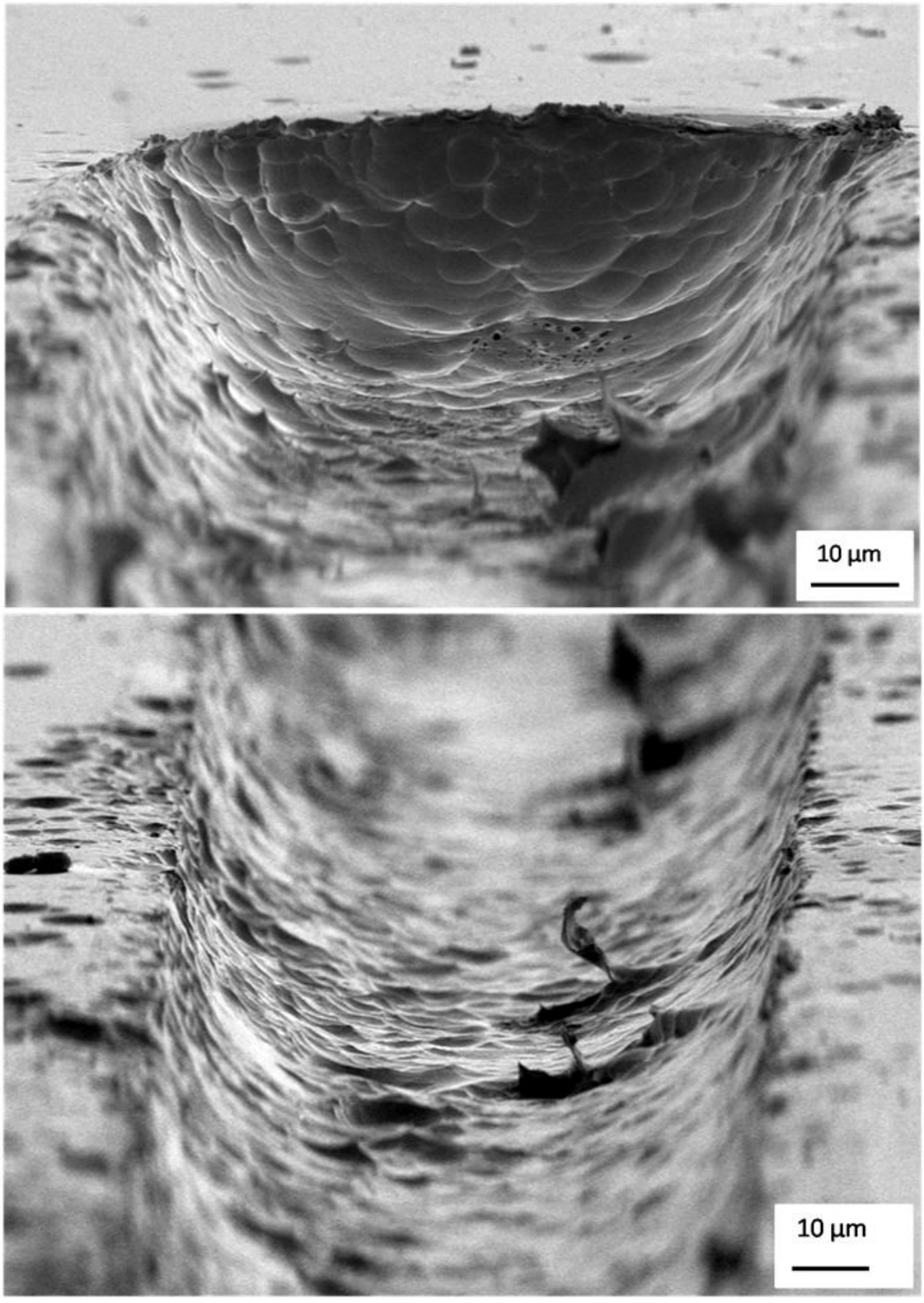

Figure 4.4: SEM images of the imprinted trench in Avatrel 2000P at 110°C, 45 bar, 60 s

Both Parylene C and Teflon AF were tested as imprint anti-adhesion layers for this application. Parylene C is Poly-monochoro-para-xylene and is widely used for its good electrical and barrier properties. Parylene unlike other polymeric materials is produced through vapor-phase deposition and polymerization of para-xylene. Parylene C is a highly crystalline, straight-chain compound that can be deposited in a completely uniform manner at room temperature even on sharp edges without voids. Because of its very low coefficients of static and dynamic friction, Parylene C can serve as a dry film lubricant, and thus was tested as an anti-adhesion layer for imprint stamps. Parylene C prevented adhesion of the stamp and substrate, but it had poor adhesion to the stamp and would peel off the stamp after undergoing approximately 5 imprint cycles. One benefit of this behavior was that the Parylene C film would retain contamination and particles when it was removed from the stamp. As a result, stamps coated with Parylene C rarely fractured after multiple imprint cycles. However the primary disadvantage was that when the film peeled, some small pieces would get caught in the rough patches of the stamp. Subsequently, the Parylene C would not coat flush to the surface of the stamp, and some pieces would then transfer onto the imprinted substrate. This contamination can be seen through careful examination of Figure 4.4. Different thicknesses of Parylene C from 1 μm – 5 μm were tested as anti-adhesion coatings, and although they all performed well as anti-adhesion layers, they all left residue on the stamps. Stamps were cleaned in Avatrel 2000P developer in an ultra-sonic bath, but improved cleaning techniques are necessary to thoroughly remove the contamination. These issues could be resolved with a smoother stamp. Teflon AF has been studied as an imprint anti-adhesion layer [43] and also performed well as an anti-adhesion layer in this application. The primary challenge with

Teflon AF was that it was difficult to physically ascertain when the Teflon coating needed to be reapplied. Since the Teflon AF did not peel off in a cohesive film, it was difficult to clean the surfaces of the stamps. As a result, the frequency of stamps cracking during the imprint process were considerably higher for stamps coated with Teflon AF than Parylene C for the same number of imprints and similar film thicknesses of coating.

To provide electrical shielding for the transmission line, copper was metalized on the imprint sample, and mechanical polishing was used to remove copper from the field regions. The recess of the structure protects the copper in the trench during polishing, reducing the need for patterning and registration steps. This thin layer of copper will minimize electrical interference by confining the signal from the core conductor within the structure and by also impeding outside signals from entering the line.

Furthermore, the inclusion of air dielectric layers in the transmission line lowers the effective dielectric constant, minimizing loss in both the dielectric and the conductor. To encapsulate air cavities, sacrificial polymers are used as space holders, but care must be taken to ensure that decomposition of the sacrificial material is compatible with other materials and processes. Reed et al. demonstrated the use of polycarbonates as a sacrificial material with a polymeric overcoat such a polynorbornene polymer Avatrel [91]. However, the decomposition temperature for the polycarbonates was 285°C making them challenging to implement with existing printed circuit board materials. Jayachandran et al. were able to reduce the decomposition temperature of polycarbonates through the addition of photo-acid generator, and air cavities encapsulated with Avatrel were fabricated at temperatures below 180°C [88]. To make the air dielectric layers suitable for

printed circuit board materials, the sacrificial polymer PPC with a small amount of photo-acid generator was used as a space holder for air cavities in the transmission line.

Incorporating the air dielectric layers requires the fabrication of a multi-layered structure; however, maintaining planarity across multiple film layers is challenging with traditional processing techniques. Planarity is critical for the ultra-low loss transmission line because non-planarity of the sacrificial PPC layer could cause the overcoat layer to be non-planar. Since the overcoat layer acts as a support for the transmission line, non-planarity compromises the mechanical integrity of the transmission line. Several methods were tested to fill PPC into the imprint trench, and the planarity of the PPC layer was subsequently evaluated. Initially, a thick layer of PPC was spin-coated and soft-baked onto the imprint sample, but the film surface was uneven making it difficult to pattern and proceed with processing. Stencil filling was also attempted by taking a blade and pushing the spin-coated PPC into the trench. However, the imprinted trench filled with PPC was recessed when compared to the field region as shown in Figure 4.5.

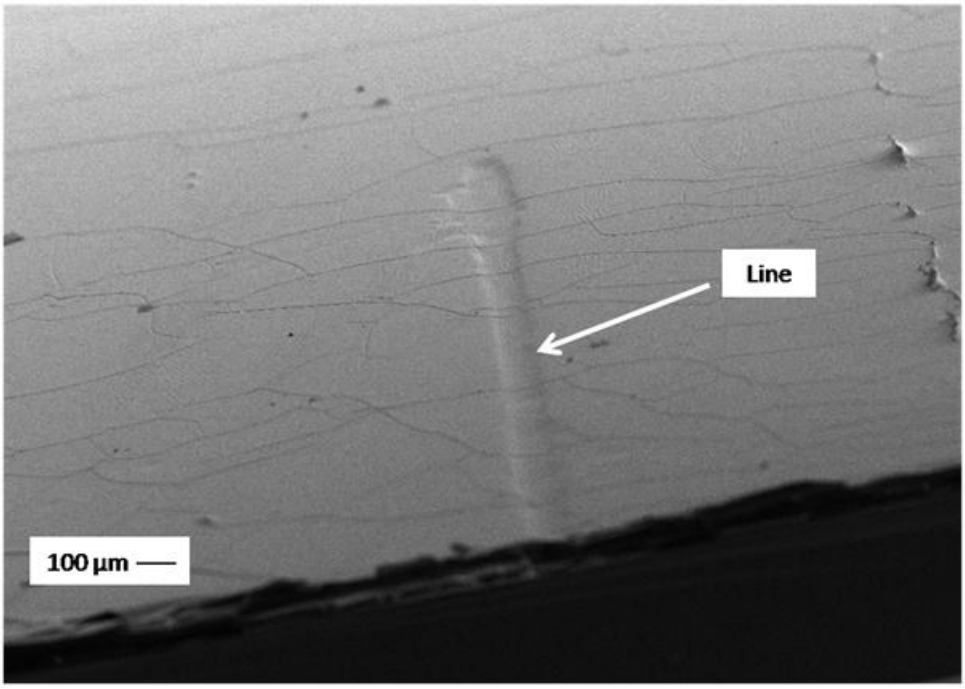

Figure 4.5: SEM image of trench stencil filled with PPC and a layer of gold for imaging

To increase the planarity of PPC in the trench, a thick layer of PPC was spin-coated, and a flat glass slide was used to press the PPC into the trench using the imprinter at 60°C, 45 bar for 180 seconds. The imprinting temperature was above the glass transition temperature of PPC causing the material to reflow into the cavity and become planar with the field as shown in Figure 4.6.

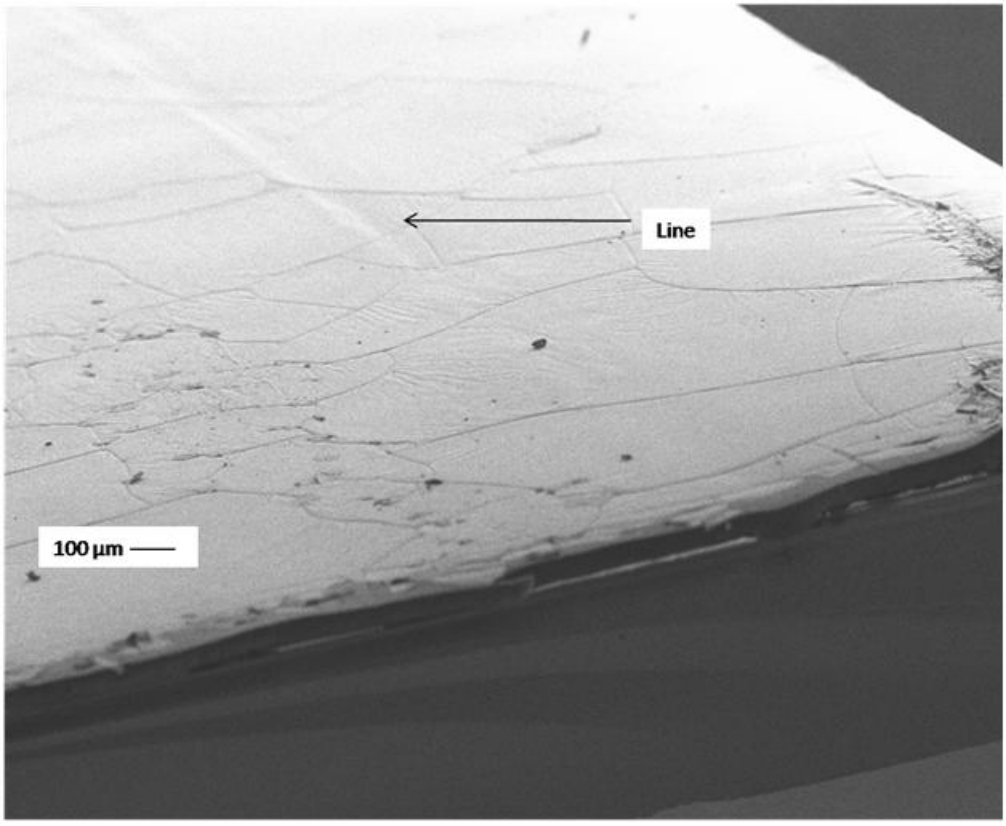

Figure 4.6: SEM image of trench imprint filled with PPC and a layer of gold for imaging

Once a planar layer of PPC was fabricated, the PPC was patterned using a unique interaction with the patterned copper in the trench to minimize masking and registration steps. It has been documented that PPC near a copper surface has slower decomposition kinetics [92]. Thermogravimetric analysis was conducted on PPC films spin-coated onto a copper and a silicon surface. PPC films that were spin-coated and soft-baked on a blank silicon wafer decomposed at approximately 160°C. PPC films that were spin-coated and soft-baked on a layer of oxide-free copper had considerably higher decomposition temperatures around 225°C. The copper only interacts with a limited PPC surface area, and some of the PPC decomposes at the lower temperature as shown in Figure 4.7. Spencer suggests that the copper interferes with the chain un-zipping reaction of PPC as

it decomposes causing the bulk film to decompose at higher temperatures [92]. However, it is unclear why some material begins decomposing at temperatures between 100-150°C. Repeated measurements produced similar results, and since the material reflows at much lower temperatures it is not likely to be a surface contact effect.

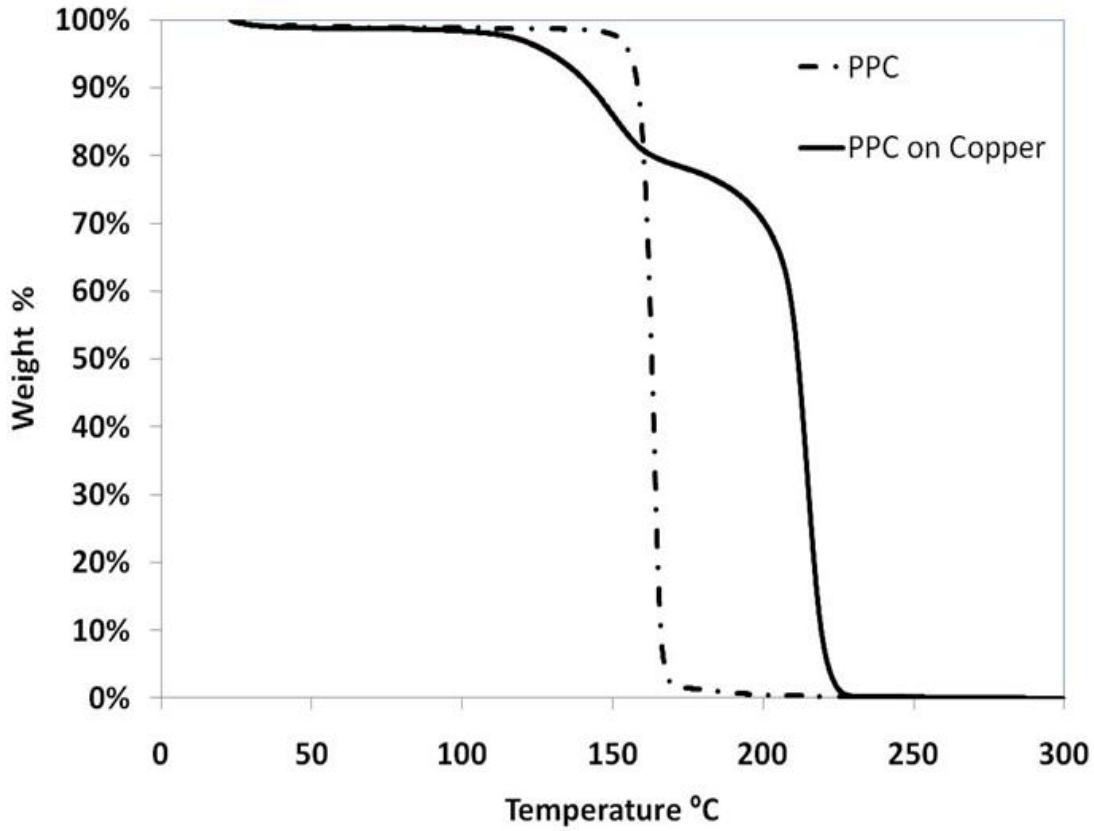

Figure 4.7: Thermogravimetric analysis of polypropylene carbonate casted on silicon wafer (dot-dashed line) and oxide free copper (solid line) using a 1°C/min ramp rate and a nitrogen atmosphere

The PPC was thermally patterned on a hotplate at 180°C. Since the decomposition of PPC on copper and PPC on Avatrel 2000P are different, the PPC on Avatrel 2000P decomposed, while it was preserved in the copper trench. The decomposition temperature is well above PPC's glass transition temperature; therefore,

the PPC reflowed until it was planar with the field. Since the copper only affects the PPC near its surface and does not completely prevent decomposition, excess PPC in the trench decomposed. Figure 4.8 illustrates an imprinted sample with PPC preserved in the trench region and a thin layer of gold for imaging.

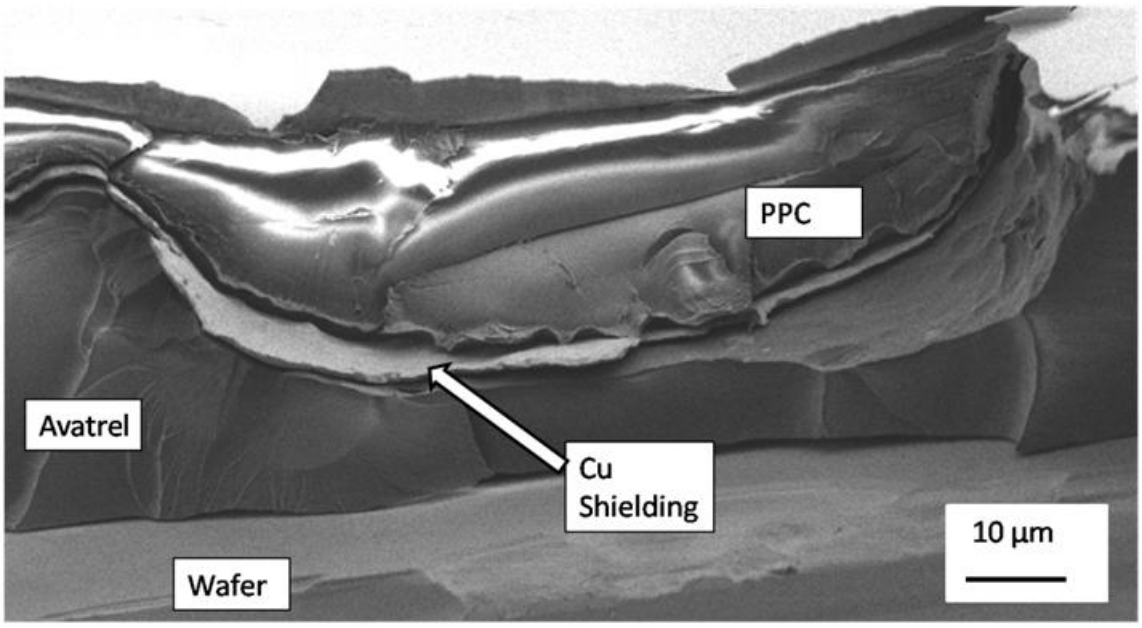

Figure 4.8: SEM image of a cross-sectioned, copper-clad, semi-circular trench with patterned PPC in trench and a layer of gold for imaging

After thermal patterning of the sacrificial material PPC, a thin layer of POSS was spin-coated and photo-processed to act as a support for the copper transmission line. As noted by Fritz et al., the modulus and hardness of POSS films after post-exposure bake is 4.9 GPa and 0.56 GPa, and after curing the modulus and hardness increase to 5.3 GPa and 0.64 GPa [90]. Due to the high mechanical strength of POSS, thin layers of film on the order of a few microns can support the transmission line. As a result, the ratio of air to polymer in the cavity can be maximized after PPC decomposition, reducing the effective dielectric constant and power loss.

Decomposing PPC through the POSS overcoat initially resulted in damage to the POSS overcoat as shown in Figure 4.9.

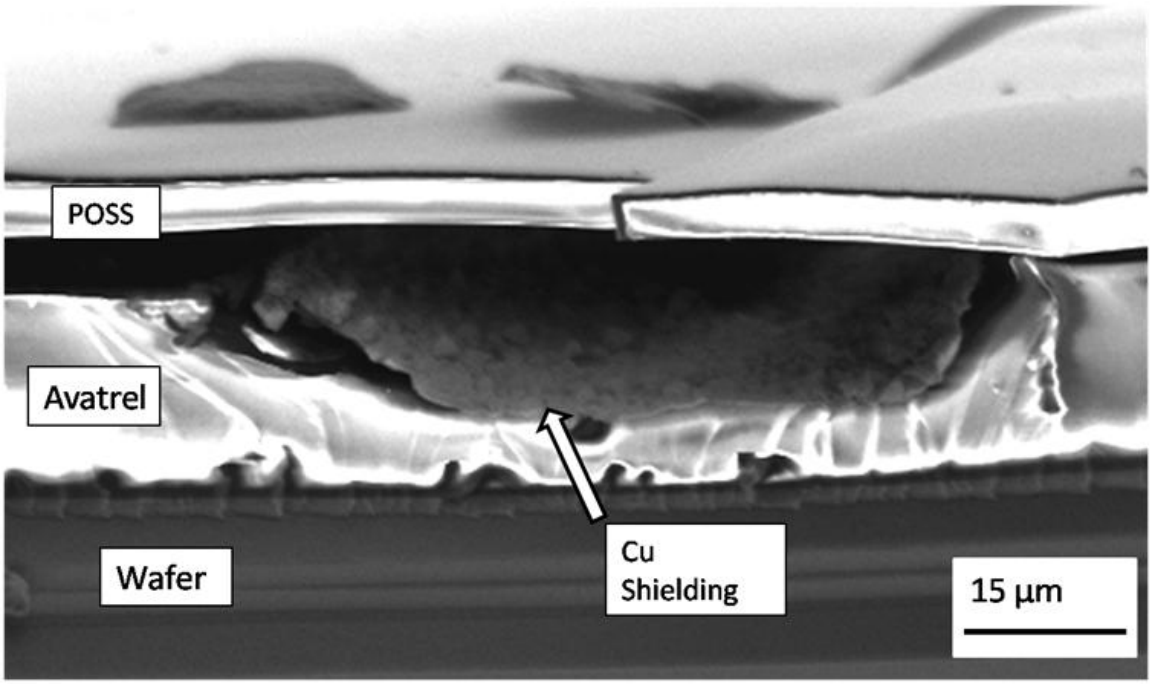

Figure 4.9: SEM image of a cross-sectioned decomposed half coaxial air cavity. The crack in the POSS cavity is due to excessive cavity pressure during decomposition

Decomposing the sacrificial material quickly can cause a pressure disparity between the air cavity and atmosphere leading to overcoat adhesion loss, ruptures, or cracking. To prevent cavity damage, the decomposition process was modified from a constant heat rate to a constant weight percent decomposition rate. By using a constant decomposition rate process, the diffusion of material through the overcoat is relatively constant, and therefore a pressure imbalance is less likely to occur. To redesign the decomposition recipe, TGA analysis of the polymer was conducted to determine kinetic parameters as recommended by Wu et al. [93]. The reaction kinetics for the thermal

decomposition of PPC was expressed as the *n*th order Arrhenius relationship shown in Equation 4.1 and the decomposition rate was assumed to be equal to a constant *r*.

$$r = Ae^{\frac{-E_a}{RT}}(1 - rt)^n \quad (4.1)$$

The decomposition reaction was determined to be first order (*n*) with the pre-exponential factor (*A*) and activation energy (E_a) to be $9x10^{12}$ min^{-1} and 120 kJ/mol respectively. Equation 4.1 was rearranged for temperature (T) vs. decomposition time (t) as shown in Equation 4.2.

$$T = \frac{E_a}{R}\left[ln\frac{A(1 - rt)^n}{r}\right]^{-1} \quad (4.2)$$

The decomposition rate was set to 0.25 weight % per minute, and a step and hold recipe temperature was designed using Equation 4.2. A final temperature hold was added at the end of the recipe to ensure a full decomposition, and the modified decomposition recipe provided a clean cavity without visible overcoat damage.

After successful fabrication of the air cavity, the transmission line was patterned using traditional lithography and electroplating. X-ray tomography confirmed that the transmission line was successfully patterned over the air cavity. However, obtaining cross sectional SEM images required cleaving the sample, resulting in damage to the structure. As shown in Figure 4.10, the copper transmission line extends from the air cavity, and the field is planar with damage only in the cleaved area.

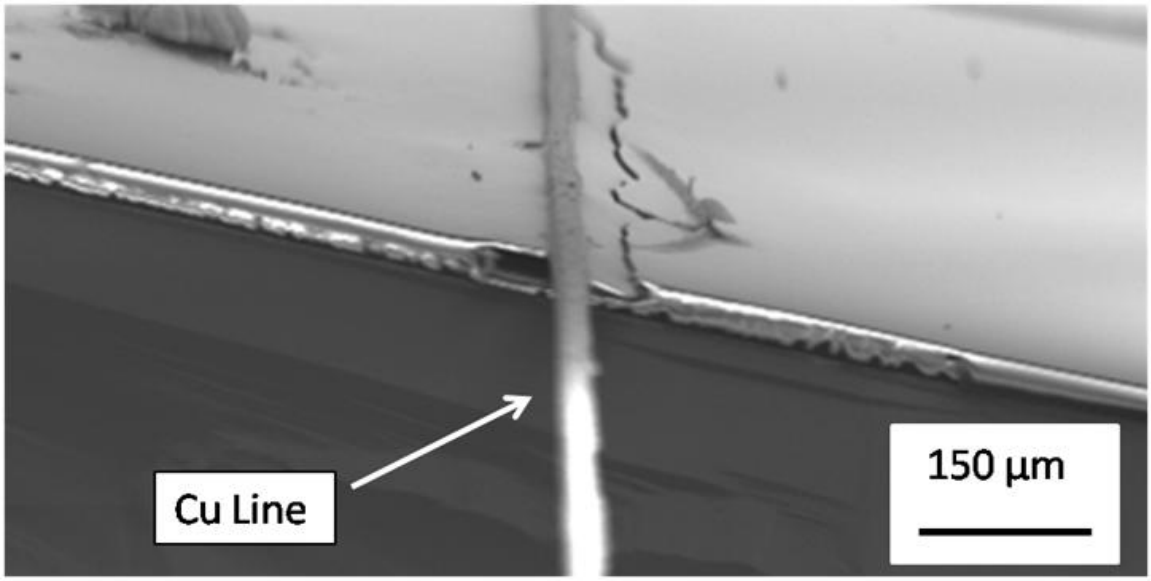

Figure 4.10: SEM image of a cross-sectioned half coaxial transmission line. The copper transmission line extends beyond the sample. The crack in the POSS overcoat is due to cross-sectioning of the sample

To evaluate the mechanical integrity of the half-coaxial structures, push tests were conducted using a nano-indenter with a conospherical tip to prevent piercing of the overcoat as recommended by Bakir et al. [94]. A triangular load function with a 10 second ramp to 8750 µN and a 10 second ramp to zero force was used to test the structures. To have a reference for comparison, push tests were initially conducted on the imprint sample over the Avatrel 2000P and POSS polymer layers and then on the air cavities with no transmission line. As shown in Figure 4.11, the indentation of the air cavity displaced 3500 nm and recovered quickly, which is 2000 nm greater than the indentation conducted on the polymer layers.

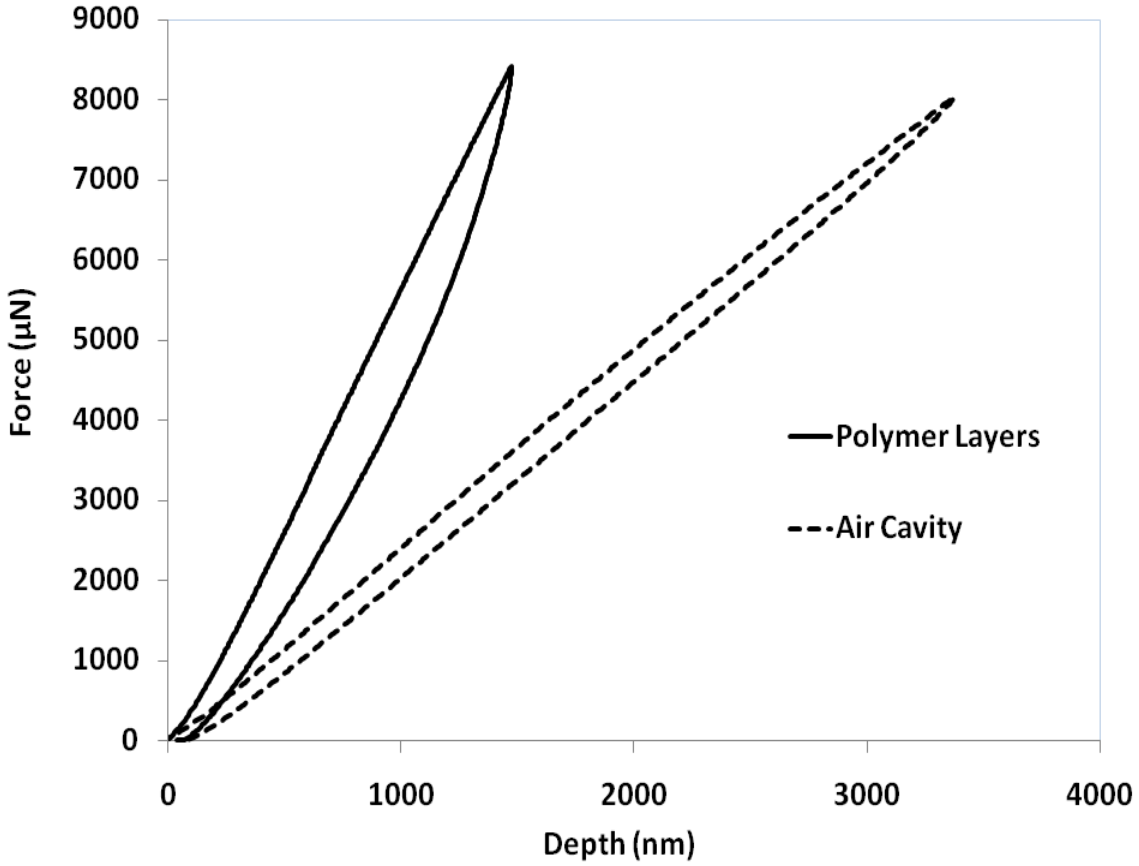

Figure 4.11: Force versus displacement curves using a cono-spherical tip with a maximum force of 8750µN for a fully constructed polymer field (solid line) and a POSS over-coated air cavity (dashed line)

Repeated indentations were attempted on the samples, but the displacement exceeded the maximum displacement on the equipment of 4500 nm. Under examination in a microscope, no visible damage could be seen on samples from the repeated push tests. Indentations were subsequently conducted on samples with a copper transmission line on the air cavity and on a copper line on the polymer layers. To account for variations in samples, an indentation on the Avatrel 2000P and POSS polymer layers was also repeated. As shown in Figure 4.12, the copper line on the polymer layers displaced less than 500 nm, whereas the copper line over the air cavity displaced 3500 nm. The

copper line does not appear to compromise the mechanical integrity of the air cavity, but due to the slow recovery of copper the indentation samples recovered slowly.

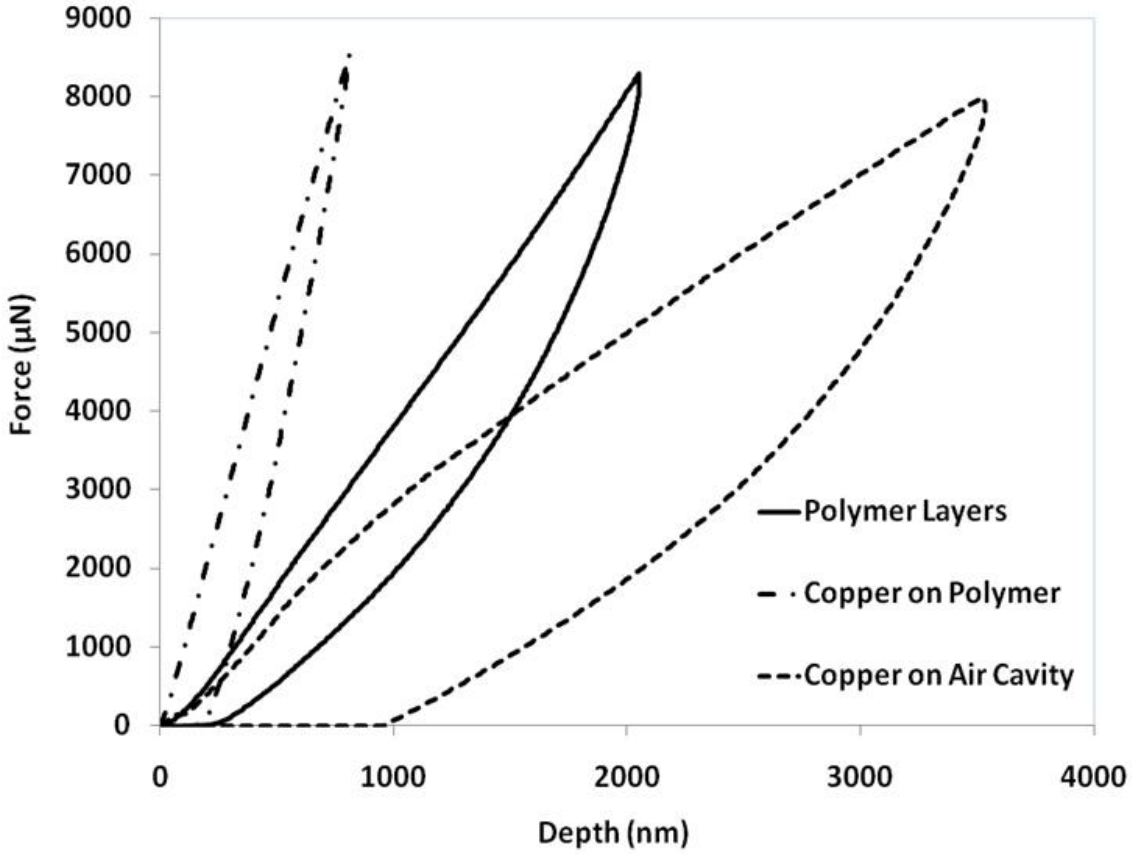

Figure 4.12: Force versus displacement curves using a cono-spherical tip with a maximum force of 8750µN for a fully constructed polymer field (solid line), copper line in the polymer field (dot-dashed line), and the copper line on the air cavity (dashed line)

To fabricate a fully encapsulated ultra-low loss transmission line, the half-coaxial transmission line was sealed with a copper lined trench in the imprinter. Researchers have demonstrated that imprint lithography can be used to thermally bond layers of material to create nano-fluidic channels with SU-8 [95-96]. Bonding the two halves of the transmission line together reduces processing and registration steps. Fabricating a fully

encapsulated air-clad transmission line, allows air dielectric layers to be embedded within the PCB rather than only on the top layers of the PCB. Also, the air-clad transmission line is embedded in a planar layer of polymer simplifying the subsequent buildup of structures and layers in the PCB.

The top half of the structure was fabricated by using a soft-baked film of Avatrel 2000P imprinted with the coaxial trench. As noted earlier, Avatrel 2000P properties change during processing, and the adhesiveness of the material decreases significantly after exposure. Therefore, the sample was sputtered and electroplated with a thin layer of copper after soft-bake. However, the copper shielding could not be patterned via mechanical polishing because the polymer layer could not withstand the abrasive forces. Therefore, the copper trench was patterned via photolithography and wet etching. The Avatrel 2000P layer was not photo-patterned during this step, since the copper layer prevented the transmission of light. The copper-lined trench was then flipped, aligned, and bonded with the half-coaxial line in the imprinter at 160°C, 15 bar for 180 seconds. At this elevated temperature, thermal cross-linking of the material is initiated, and curing was then conducted on the sample in a furnace at 160°C for one hour. The imprinting was conducted at 15 bar, which is the minimum pressure on the equipment, to ensure that the POSS layer would not be damaged during imprinting, even if misalignment of the layers occurred. Samples were attempted to be separated after bonding and after cure, but the substrates would crack before the polymer interfaces would delaminate, suggesting good adhesion between the layers.

Several release layers were also tested for removing the top substrate off the ultra-low loss transmission line. Photosensitive tapes and photo-resist both demonstrate

potential as a sacrificial release layer for this application. To use photo-resist as a sacrificial release layer, a layer of NR-9 was spin-coated onto the substrate before coating of the Avatrel 2000P. This material was chosen because it has similar processing conditions to the Avatrel 2000P and was not miscible in the developer used to photo-pattern the copper trench. Samples imprinted with the NR-9 layer showed no changes in the resolution of the imprinted features. After bonding with the half-coaxial line, the NR-9 was dissolved in acetone in an ultrasonic bath for three minutes. No damage to the encapsulated cavity was observed, and the Avatrel 2000P remained adherent to the POSS layer. On an industrial scale, using a soluble release layer could be challenging as transport would be limited as sample size increased. Photo-sensitive tapes have strong adhesive strength that are reduced significantly after UV irradiation and are used in industrial applications for wafer dicing and grinding. To use as a release layer, the photo-sensitive tape was bonded onto a transparent substrate in the imprinter and the Avatrel 2000P was subsequently spin-coated and processed. On the lab scale, obtaining a completely planar layer was challenging. During bonding in the imprinter, wrinkles would be entrapped in the layer making planarity a challenge during subsequent processing. However on an industrial level, these issues could be resolved with the proper equipment. An additional challenge of implementing the photo-sensitive tape is managing the coefficient of thermal expansion mismatch between the layers. Rapid heating and cooling caused buckling of the photo-sensitive tape from the carrier substrate in some samples.

4.4 Conclusion

Imprint lithography and sacrificial polymers have been used to fabricate a novel structure with smooth transitions, metallic shielding, and encapsulated air dielectric layers. Using imprint lithography, the semi-circular geometry was transferred into Avatrel 2000P with only elevated temperature and pressure. Curved structures are difficult to make using traditional photolithography which demonstrates the potential of imprint lithography to build complex geometries. The rounded terminations can be integrated with vertical connections with smooth transitions that will reduce reflections and therefore increase power transmission. Additionally, the imprint process planarized surfaces simplifying the buildup process and is compatible with traditional board processing. Furthermore, the natural relief of the structure allowed the copper shielding in the trench to be patterned using simple mechanical polishing eliminating a masking and registration step. Sacrificial polymers were encapsulated in copper and Avatrel 2000P. Air insulation layers can lower the effective dielectric constant and therefore, reduce power loss and increase signal propagation velocities [7].

Conductor, dielectric, and radiation losses along with reflections and discontinuities must be reduced to enable high frequency chip to chip communication. This structure is the first reported to incorporate features to mitigate all of these losses. The fully encapsulated air-clad transmission line can be embedded within the PCB extending the benefits of air dielectrics. These processes can enable the fabrication of ultra-low loss transmission lines to increase the lengths at which the signal can be routed at the proper signal to noise ratio or increase the data rate per channel.

CHAPTER 5

AQUEOUS-DEVELOP, PHOTOSENSITIVE POLYNORBORNENE DIELECTRIC: PROPERTIES AND CHARACTERIZATION

5. 1 Introduction

Photosensitive, thick-film, high aspect ratio polymers are used for a wide range of applications in microelectronics and MEMS. Extensive research has been conducted to establish structure-property relationships with epoxy based polymers such as Avatrel 2000P (Promerus LLC) and SU-8 (MicroChem) [97-101]. Avatrel 2000P is a copolymer of alkyl norbornene and epoxide-functionalized norbornene monomers, as shown in Figure 4.2 (a). The properties of the polymer film can be controlled by varying the alkyl to epoxy ratio. The alkyl side groups have been shown to lower the elastic modulus and increase the elongation to break, and the epoxide side groups provide cross-linkable sites, increase adhesion characteristics, and increase the elastic modulus [98].

SU-8, shown in Figure 5.1, is an epoxy-based resin initially developed by IBM[102-103]. It has been used extensively to make high aspect ratio MEMS structures and packaging components [102-104]. The resin has a low molecular weight and can be dissolved in a variety of organic solvents [105]. It has a high degree of functionality with high mechanical strength, chemical inertness, and thermal resistance [101]. The final properties of SU-8 are sensitive to processing conditions, and the reported properties have some variability [16,106-109].

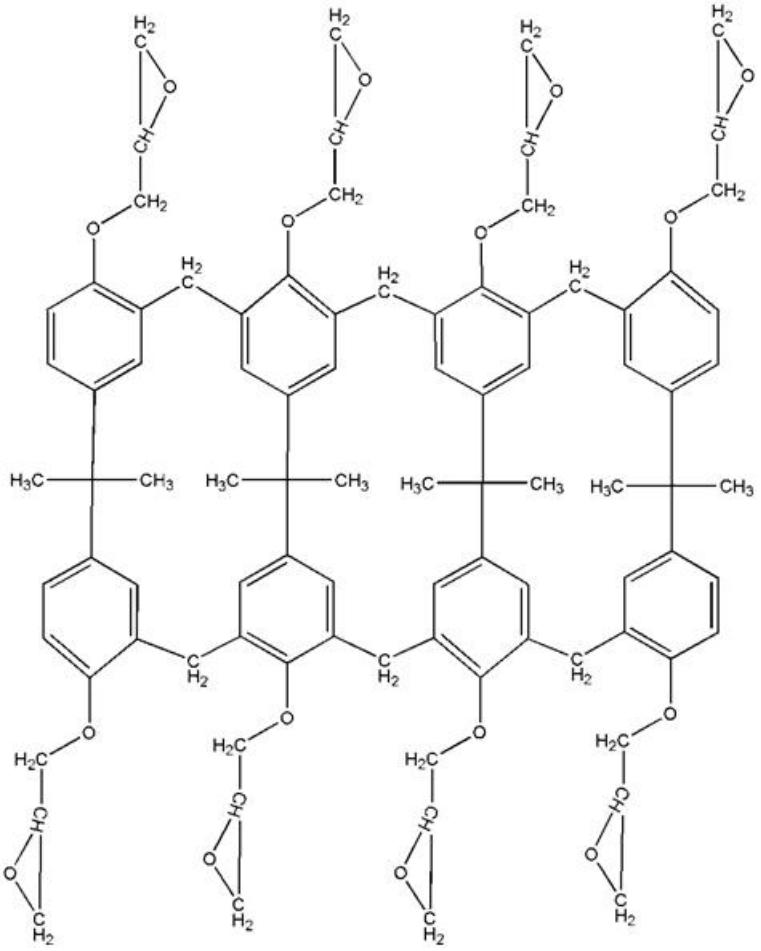

Figure 5.1: The chemical structure of SU-8

In this work, characterization has been performed on Avatrel 8000P (Promerus LLC) a new high aspect ratio, aqueous base develop, photosensitive polymer. Avatrel 8000P, shown in Figure 5.2, consists of a norbornene backbone with fluorinated alcohol groups which provide solubility in an aqueous base and carboxylic acid groups which provide cross-linking sites with epoxy units. The polymer formulation is a mixture containing a multifunctional epoxy cross-linker, a photo-package and an adhesion promoter.

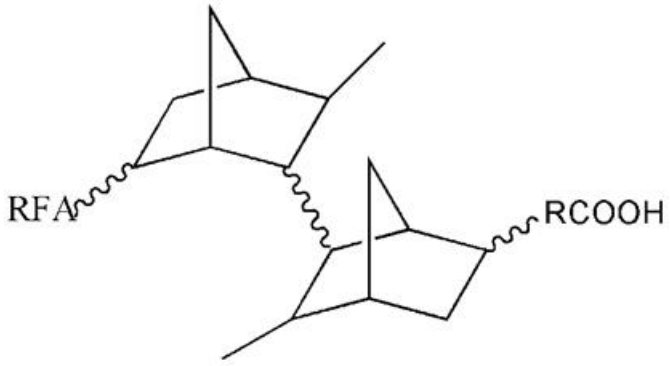

Figure 5.2: The chemical structure of Avatrel 8000P

The contrast and optical properties were studied and compared to Avatrel 2000P and SU-8 to better understand the high aspect ratio of the patterned films. The impact of curing condition and exposure dose on the mechanical, thermal, and electrical properties of Avatrel 8000P has been evaluated. The relationship between processing conditions and material properties were examined to optimize the process conditions in order to obtain a high quality Avatrel 8000P film. Additionally, the impact of the different polymer structures of Avatrel 2000P, SU-8, and Avatrel 8000P on material properties and performance are discussed.

5.2 Experimental

Avatrel 2000P was processed according to the procedures of Bai et al., [97-98] and SU-8 was processed according to the procedures listed on the MicroChem website [110-111]. Avatrel 8000P samples were spin coated onto <100> silicon wafers and then soft baked on a hotplate at 100°C for 5 minutes to remove the solvent from the polymer film. A variable density optical mask (Opto-line International Inc.) was used to study the effect of dose on polymer properties. A 1 kW Hg-Xe lamp with 365 nm filter was used for UV exposure. The post-exposure bake was performed on a hotplate at 100ºC for 5 minutes

and the films were developed in MF-319 (Shipley). Curing was performed in a nitrogen purged furnace, and the samples were ramped to their cure temperature at 5ºC/min and held at temperature for 1 hour. The furnace was allowed to cool slowly by natural convection to room temperature.

A Zeiss Ultra 60 was used to obtain SEM images of the processed films. Film thicknesses were measured with a Veeco Dektak profilometer, and UV absorption was measured on quartz wafers with a Hewlett Packard 8543 UV-vis spectrophotometer. The residual film stress in polymer films was measured at room temperature using the Flexus Tencor F2320. Weight loss due to temperature exposure was measured using a TA Instruments Q50 thermogravimetric analyzer. The temperature inside the sample chamber was increased at a rate of 5^{o}C/min or 0.5^{o}C/min from 27^{o}C to 500^{o}C under N_2 atmosphere.

Quasi-static nano-indentation was conducted on polymer samples using a Hysitron Triboindenter with a Berkovich tip. The peak load was varied between 250 and 7500 μN over a 5x5 array of points per sample. A maximum drift rate of 0.1nm/s was set for the experiment and was automatically determined over a 40 second period. The tip was loaded to maximum load in 10 s, held for 10 s and unloaded in 2 s. The load-depth curves were analyzed for the 25 points using the Oliver-Pharr model [63]. The reduced modulus (E_r) was extracted from 20% to 95% of the unloading curve and the hardness (H) was obtained by using equations 2.4-2.6. The samples were indented in the central regions of the polymer samples to eliminate edge effects. Additionally, to minimize the impact of thermal drift the first five points were discarded, and subsequently, only indents above 500 nm were included in the average modulus and hardness presented.

The ring opening reaction of epoxide groups with the polymer was measured by Fourier transform infrared (FT-IR) spectroscopy using a Magna 560 spectrometer (Nicolet Instruments). FT-IR scans of samples were collected in transmission mode on KBr crystals, and for each measurement 512 scans at a resolution of 2.00 cm^{-1} were averaged. Specifically, the change in the peak at 844 cm^{-1}, associated with the C-O-C stretching, was used to monitor conversion. Dielectric measurements were performed by fabricating parallel plate capacitors. The bottom plate of the capacitors was a full-surface metal film of sputtered Ti/Au/Ti (300/4000/300 Å) using the Unifilm sputtering system. The top electrode consisting of Ti/Au/Ti (300/4000/300 Å) was patterned by photolithography and wet etching. The capacitance and conductance were measured on 25 samples at 10 kHz using a Hewlett Packard 4236 LCR meter on a Karl Suss probe station at room temperature. No correction was needed for fringing fields around the perimeter of the capacitors due to the high capacitor area-to-thickness ratio (>1000) [112].

5.3 Results and Discussion

Photo-definable polymers with high contrast and high sensitivity are valuable because of their ability to form thick, high aspect ratio polymer structures. The polymer structures must also have high mechanical strength and excellent optical properties to be suitable for MEMS and microelectronics applications. The spin speed versus thickness curve in Figure 5.3 illustrates that thick Avatrel 8000P films above 100 μm can be obtained in a single coat.

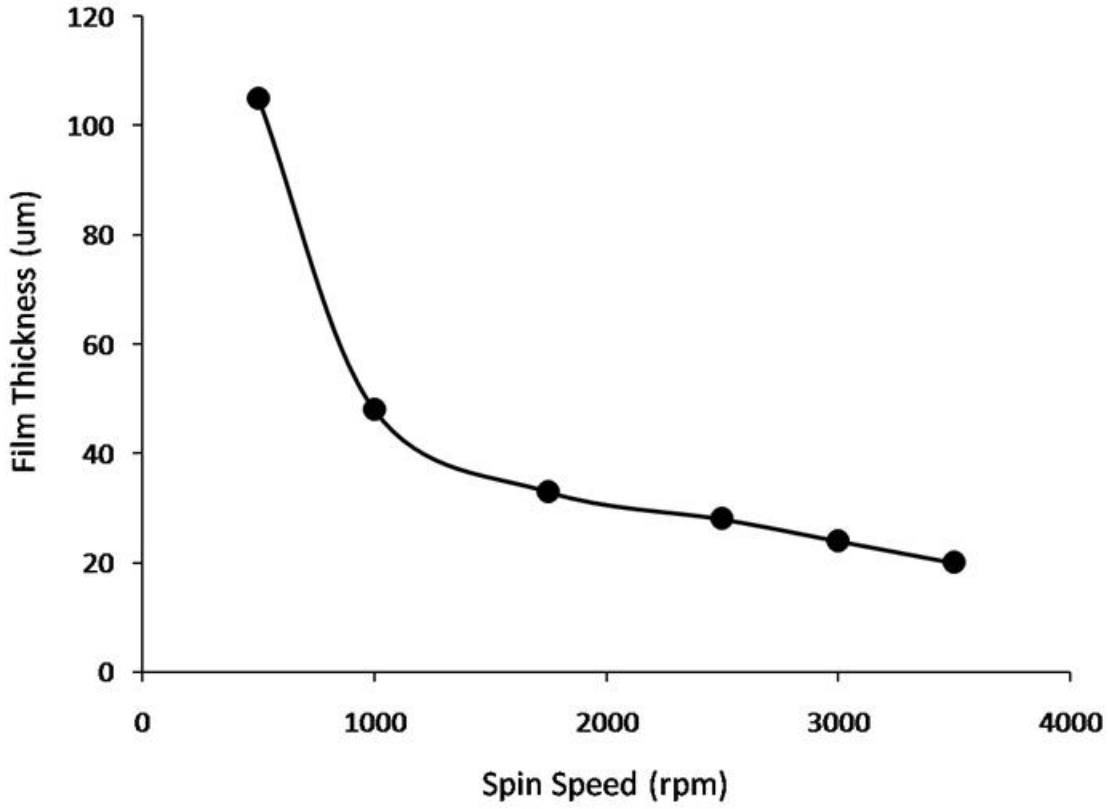

Figure 5.3: Avatrel 8000P spin speed versus thickness curve

Avatrel 8000P samples were baked for 5 minutes before and after exposure at 100°C, whereas SU-8 requires longer processing times and temperature ramping steps for comparable film thicknesses. Avatrel 8000P was spun at 750 rpm, photo patterned with an exposure dose of 500 mJ/cm^2, and the resulting 70 μm features are shown in Figure 5.4. The lines in the SEM image have a high aspect ratio of 7:1 (height:width) with smooth, straight side wall profiles.

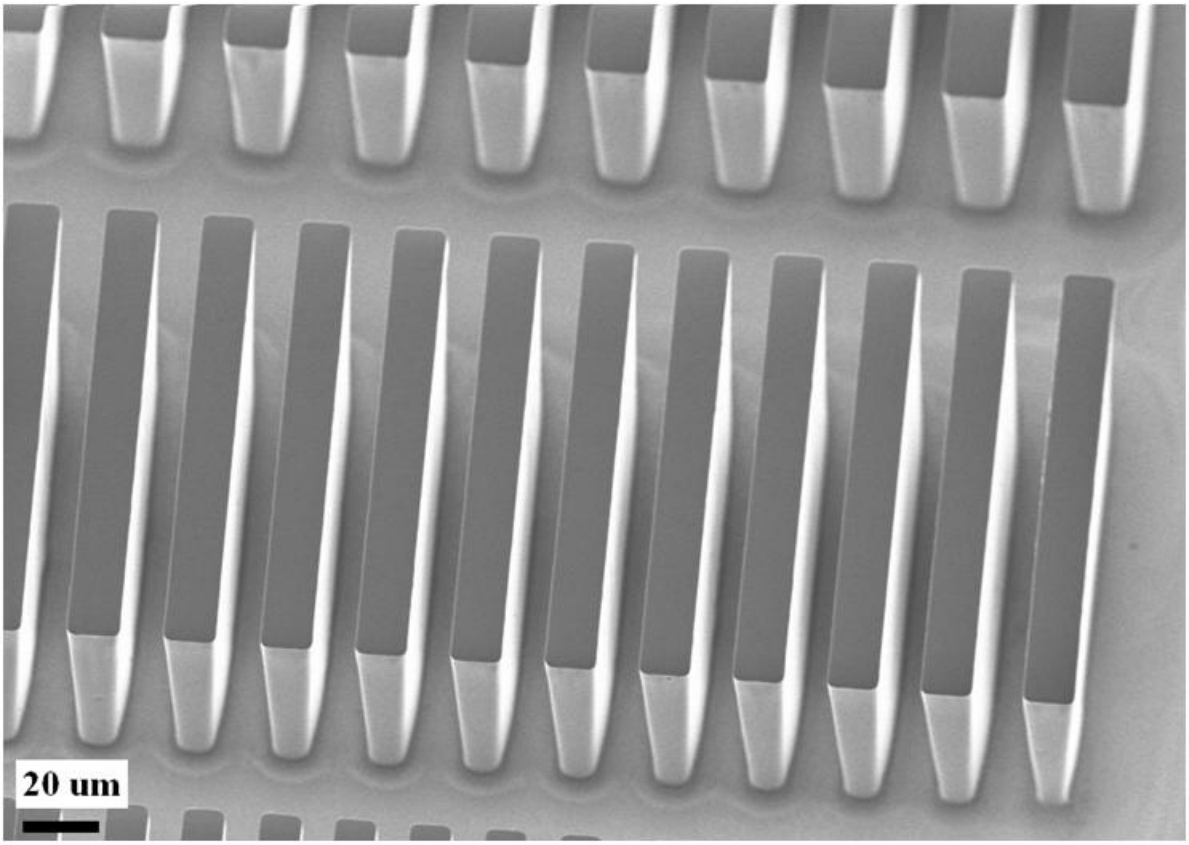

Figure 5.4: S.E.M. image of 7:1 (height:width) Avatrel 8000P lines photo-patterned with an exposure dose of 500 mJ/cm^2

Avatrel 8000P was also evaluated for its ability to make complex shapes, and a hollow core cylindrical structure fabricated with the same processing conditions is shown in Figure 5.5. The aspect ratio in Figure 5.5 is 5:1 (height:width) where the inside diameter of the core corresponds to the width dimension.

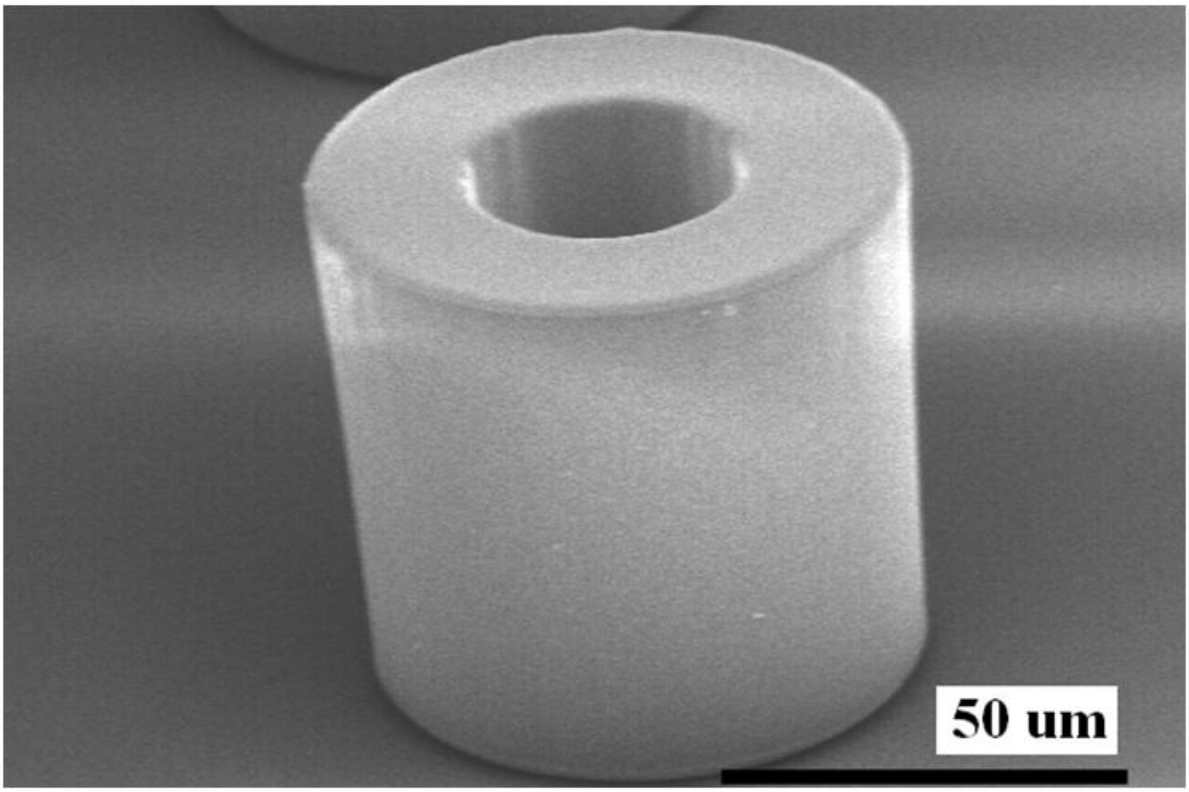

Figure 5.5: S.E.M. image of 5:1 (height:width) Avatrel 8000P hollow core cylinder photo-patterned with an exposure dose of 500 mJ/cm^2

The aspect ratio of the hollow structure is lower than the aspect ratio of the solid structure, because delamination occurred in cylinders with aspect ratios above 5:1. In high aspect ratio hollow structures, the transport of the developer in the core is slow compared to the transport of developer around the perimeter of the feature. As a result, hollow structures required longer develop times than solid features of comparable aspect ratios which caused delamination of features with aspect ratios above 5:1. There is a slight slope in the high aspect ratio lines shown in Figure 5.4 which appears more pronounced due to the angle of the SEM image, but the hollow pillar in Figure 5.5 suggests that the taper is minimal. Sidewall slope occurs in thick, high aspect ratio structures due to variations across the thickness of the film. As MicroChem suggests,

negatively sloped sidewalls can be mitigated by using a filter to remove shorter wavelengths that are absorbed in the upper portion of the polymer and by tuning exposure dose and baking conditions to obtain uniform cross-link density throughout the film [113].

The contrast value of thick Avatrel 8000P films was measured to better understand the limitations of the material to pattern high aspect ratio features. Contrast is an important parameter for photoresists and is usually measured in thin films. Although contrast normally decreases with an increase in film thickness, the contrast value for Avatrel 8000P was high (γ=12.2). Figure 5.6 shows the contrast curve for a thick film of Avatrel 8000P using front-side exposure, and a least squares method was used to fit the slope of the line from D_0 to D_{100} (Eqn. 2.1).

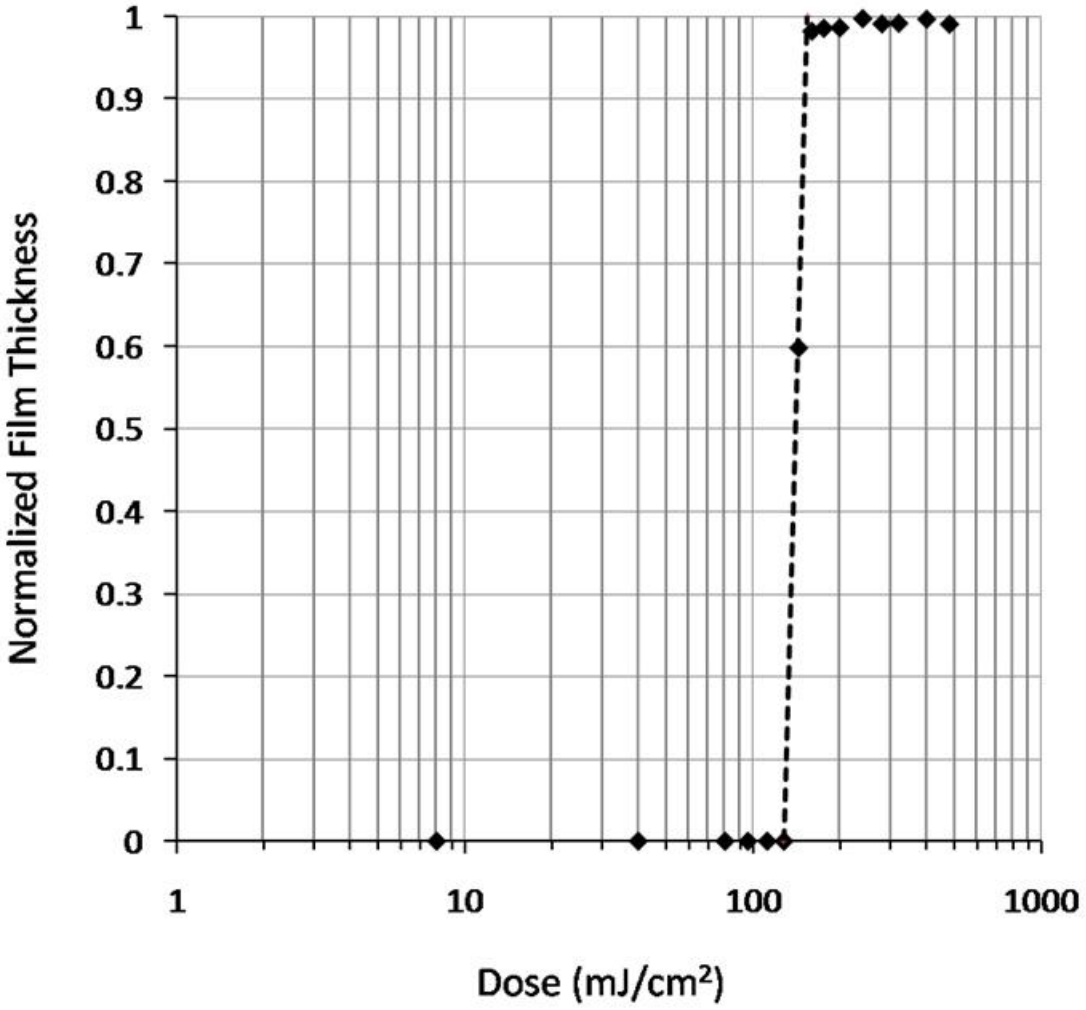

Figure 5.6: Contrast curve for thick Avatrel 8000P films obtained using front-side exposure ($\gamma = 12.2$)

Measuring contrast using front-side exposure is appropriate for processing applications, but the accuracy of the contrast is limited by the number of obtainable data points between D_0 and D_{100}. Contrast measurements are traditionally conducted in thin films where dose can be considered relatively constant through the film. However, in thick films, the exposure dose at the top of a feature is higher than the dose at the bottom of a feature due to absorption of UV light within the film. One consequence of measuring contrast in a thick film is that if the surface of the polymer were exposed to a dose

corresponding to D_{100} then the base of the polymer film may receive a dose less than D_0. Thus, the dissolution rate at the base of the feature would be greater than the dissolution rate at the top of the feature. The higher dissolution rate at the base is a consequence of lower cross-linking and can affect the adhesion of the film to the substrate causing delamination. Therefore, obtaining data points between D_0 and D_{100} is particulary difficult for negative-tone, thick film polymers. For comparison, contrast measurements were conducted using front-side exposure for SU-8 and Avatrel 2000P as shown in Figure 5.7.

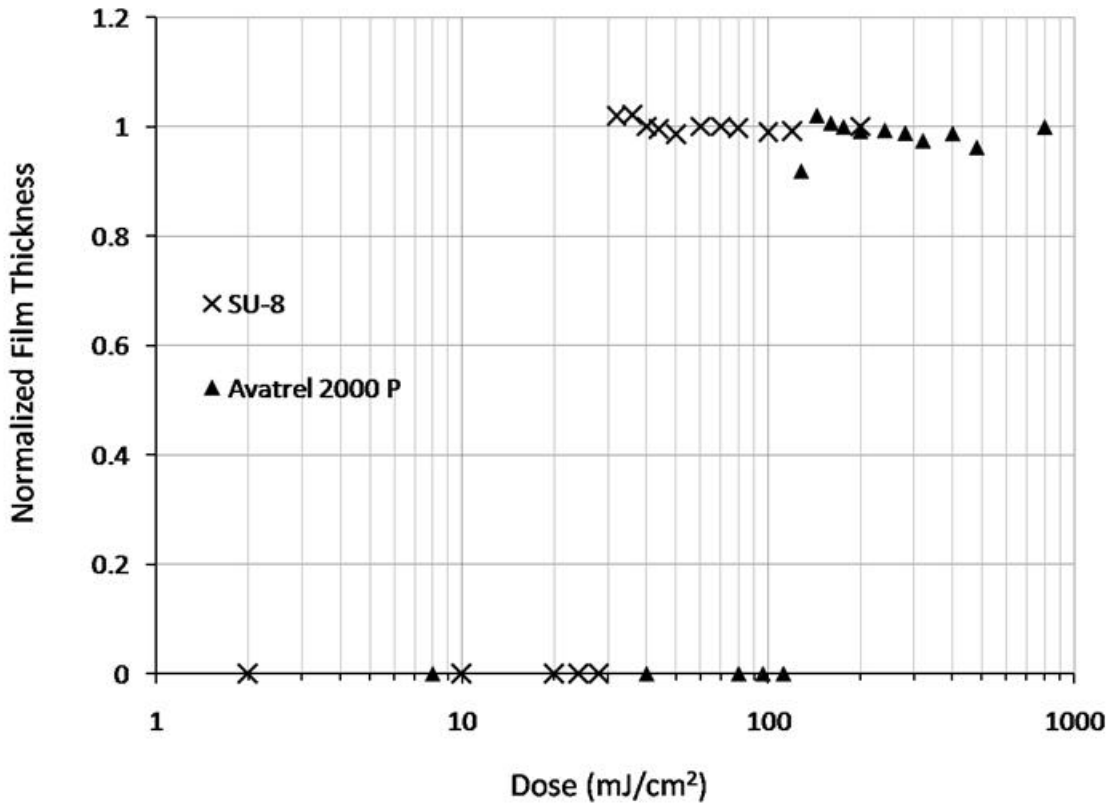

Figure 5.7: Contrast curve for thick Avatrel 2000P and SU-8 films obtained using front-side exposure

In these figures, the films irradiated with doses near D_{100} have delamination due to poor substrate adhesion and high film stress. The contrast values are not reported due to the difficulty in determining the exact value of D_{100} due to delamination. The sensitivity of SU-8 and Avatrel 2000P are 40 mJ/cm^2 and 176 mJ/cm^2, respectively.

A series of back-side exposures were performed to evaluate the impact of adhesion on the contrast values. Irradiating the polymer through a UV transparent substrate results in the highest exposure dose and highest level of cross-linking at the polymer-substrate interface. Since the dissolution rate near the bottom of a feature was less than the top surface with back-side exposure, more data points could be collected between D_0 and D_{100}. Figure 5.8 shows the contrast curve obtained for Avatrel 8000P through back-side exposure, and after curve fitting, the contrast was found to be 9.04.

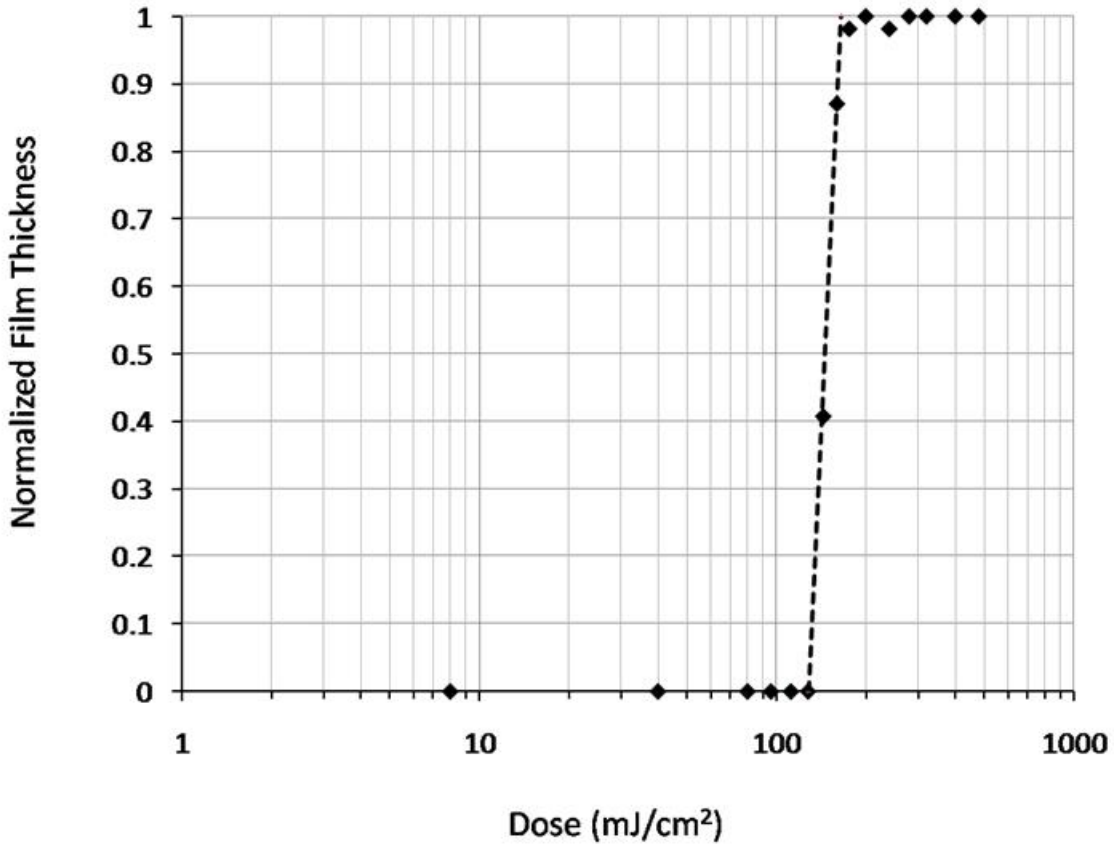

Figure 5.8: Contrast curve for thick Avatrel 8000P films obtained using back-side exposure ($\gamma = 9.04$)

The lower contrast value obtained from backside exposure is attributed to the shift in the D_0 and D_{100} doses. The shift of D_0 and D_{100} occurs because the level of cross-linking at the top and bottom of the film differ from the case of front-side exposure, resulting in different dissolution rates for the two exposure methods.

As previously mentioned, the absorption coefficient of a photo-definable material impacts its resolution and ability to make high aspect ratio features in thick films. Eyre et al. have shown that if the optical absorption of a photo resist is too high, UV light will not penetrate a thick resist layer and therefore clean, sharp images cannot

be generated [114]. The absorption coefficient of fully formulated Avatrel 8000P (i.e. with epoxy functionalized crosslinker, and photo-package) was measured after soft bake, exposure, and post-exposure bake. As shown in Figure 5.9, the absorption coefficient at 365 nm is 110 cm^{-1} after soft-bake and 94 cm^{-1} after post exposure bake. The decrease in absorption coefficient after post exposure bake is due to decomposition of the photo-package after exposure, lowering the number of absorbing groups. To evaluate only the contribution of the norbornene copolymer, the absorption coefficient of the norbornene copolymer was measured in propylene glycol monomethyl ether acetate (PGMEA). At the 365 nm, the absorption coefficient is 0.25 cm^{-1}, indicating that the norbornene molecule absorbs a small amount of photons compared to the photo-package. Thus, the high aspect ratios of the patterned Avatrel 8000P films is a result of the high contrast values and low absorption coefficient.

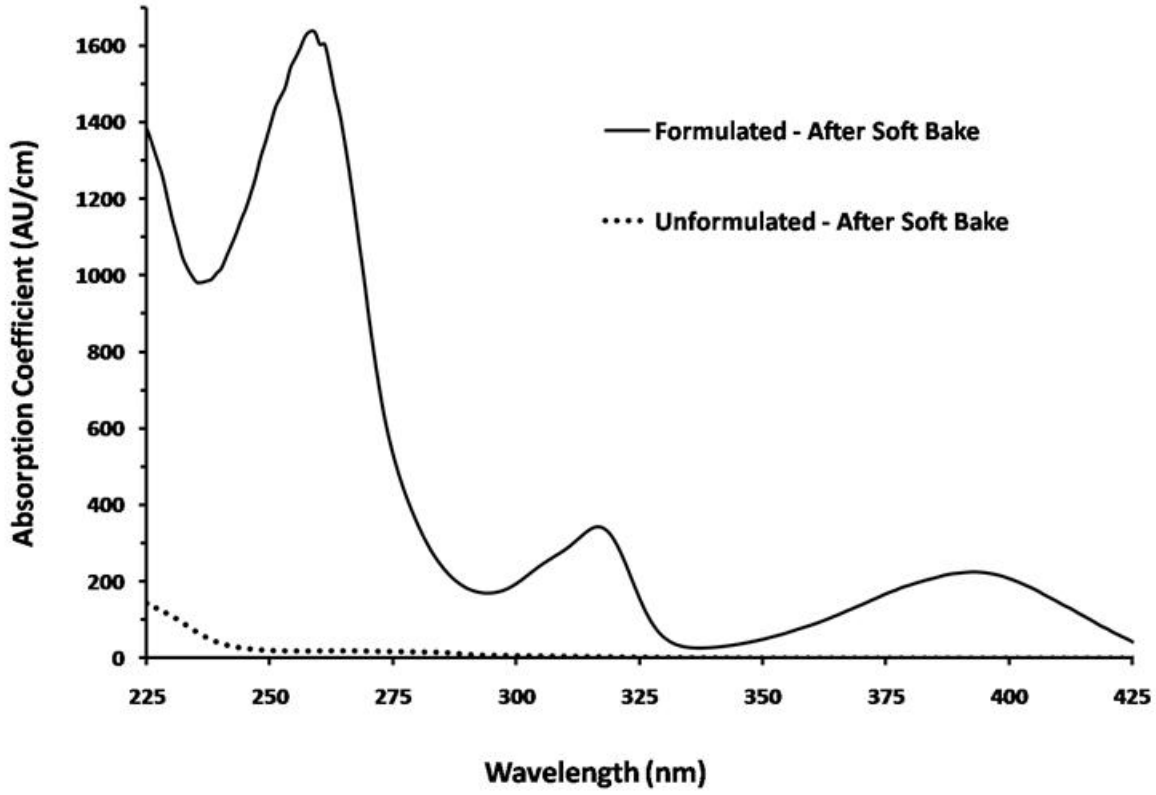

Figure 5.9: Changes in the absorption coefficient of fully formulated Avatrel 8000P and pure norbornene Avatrel 8000P from 225 nm – 425 nm

A brief mechanical comparison of Avatrel 2000P, Avatrel 8000P, and SU-8 was conducted with nano-indentation after cure, and the force versus displacement of the materials at a load force of 2000 μN is shown in Figure 5.10.

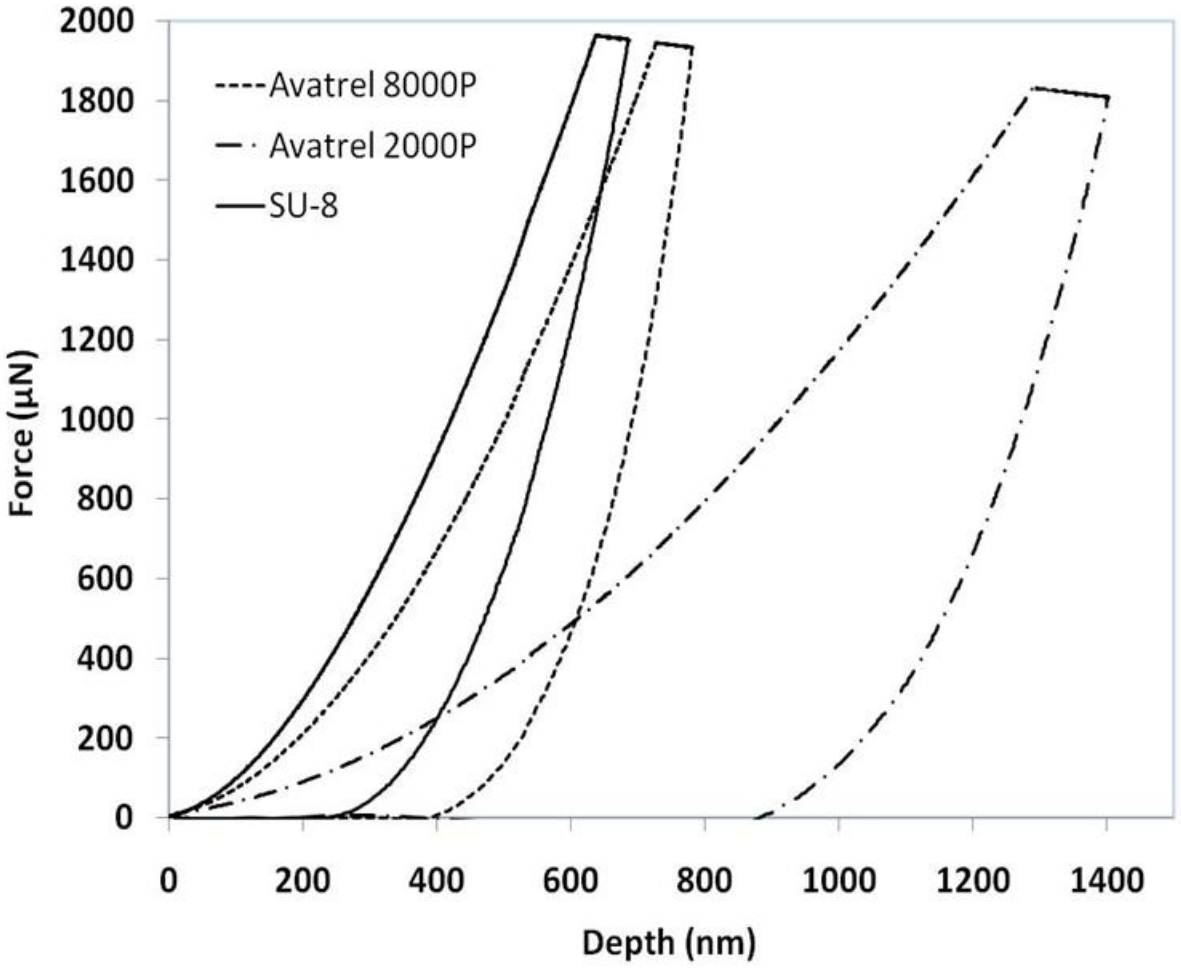

Figure 5.10: Force versus displacement curves with a maximum force of 2000 µN for Avatrel 8000P (dashed line), Avatrel 2000P (dot-dashed line), and SU-8 (solid line) after cure

Avatrel 2000P was the softest material with a modulus of 1.0 GPa and hardness of 0.04 GPa. SU-8 and Avatrel 8000P had comparable modulus values of 2.9 GPa which is illustrated by their similar slopes in the unloading segment of Figure 5.10. However, SU-8 had a hardness value of 0.24 GPa versus 0.18 GPa for Avatrel 8000P which causes SU-8 to have a smaller displacement for a given force than Avatrel 8000P. As a result, SU-8 is more susceptible to brittle failure than Avatrel 8000P in devices.

To evaluate the suitability of Avatrel 8000P as a permanent dielectric in MEMS and microelectronics applications, the impact of processing on the mechanical properties of Avatrel 8000P were analyzed using nano-indentation. Avatrel 8000P samples were indented after soft bake and after an exposure dose of 500 mJ/cm^2, and the modulus of the soft baked and exposed films was 1.1 GPa and 1.3 GPa, respectively. A sample indented after post-exposure bake had variation in modulus values over the top few microns of the surface of the film. To assess the bulk film properties of Avatrel 8000P, a sample was indented from the backside of the film and a modulus of 1.8 GPa was obtained.

To evaluate the impact of cure temperature on Avatrel 8000P's reduced modulus, cure temperatures from 160°C to 250°C were investigated. As shown in Figure 5.11, modulus values increased nearly 40% from 160°C to 225°C, and the increase is attributed to higher cross-link density as the cure temperature increased. Chiniwalla et al. found that the final extent of epoxy ring opening is greater at the higher temperatures due to increased diffusion coefficient of the photo-acid generator and reactive groups leading to improved network interconnectivity [100]. At 250°C, Avatrel 8000P's decomposition reactions occur at a faster rate than the cross-linking reactions, resulting in the lower modulus.

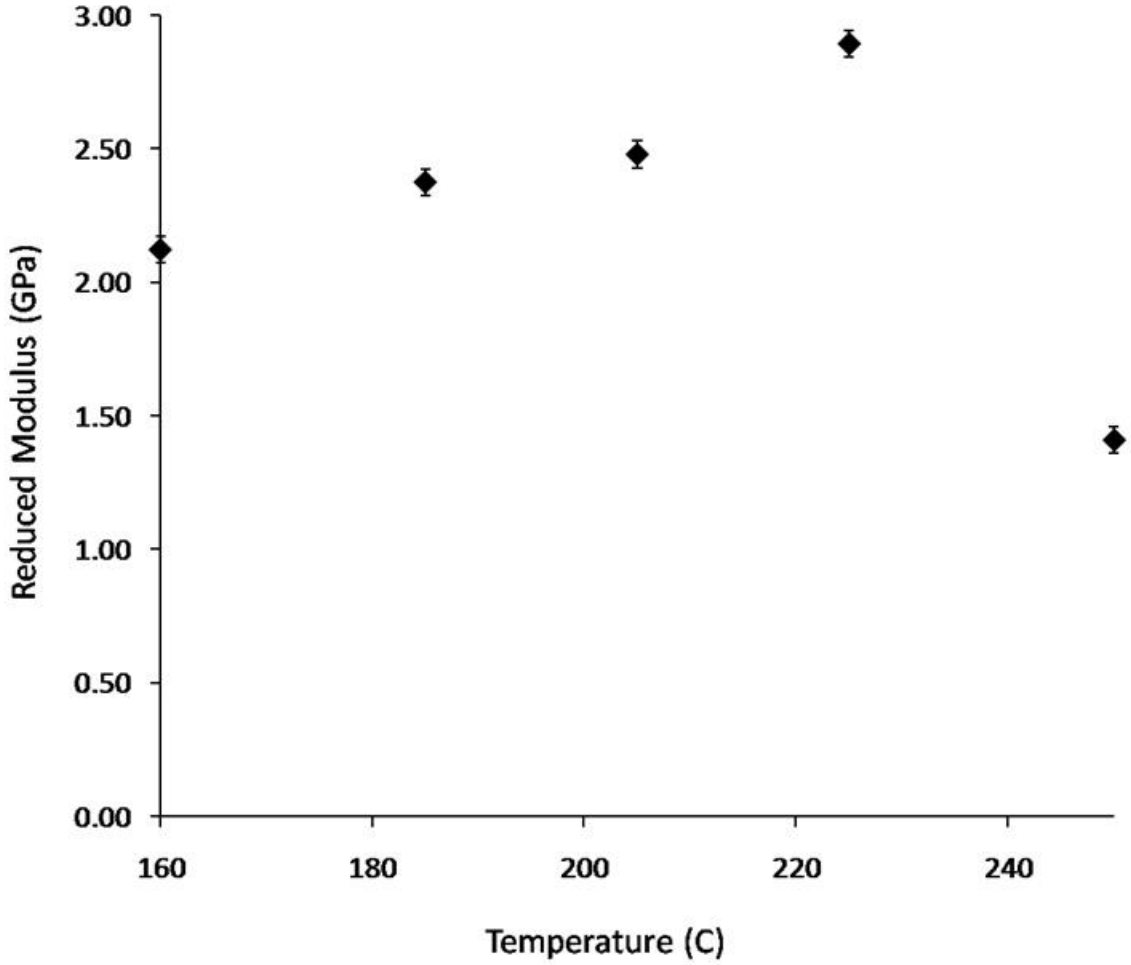

Figure 5.11: The reduced modulus of Avatrel 8000P as a function of cure temperatures from 160°C to 250°C

An Avatrel 8000P sample originally cured at 225°C had a modulus of 2.9 GPa and after being subjected to a second cure for two hours at 250°C, it had a modulus of 2.5 GPa. The moderate rate of decrease in modulus with time at the elevated temperature suggests that the cross-linking groups are difficult to break once formed resulting in high thermal stability of the cross-linked film. Avatrel 2000P and Avatrel 8000P samples were also indented after a 160°C cure and after an extended cure of the same samples for an additional 10 hours at the same temperatures. After the 160°C one hour cure, Avatrel

8000P and Avatrel 2000P had a reduced modulus of 2.1 GPa and 0.6 GPa, respectively. After the extended cure, the modulus of Avatrel 8000P and Avatrel 2000P both drop by 50%. The loss in modulus is attributed to the loss of linkages through thermal decomposition. Chiniwalla et al. have shown that decomposition reactions associated with an epoxide side group can occur at temperatures greater than 160°C [100].

Epoxide reactions were studied using FT-IR spectroscopy to determine the level of cross-linking in Avatrel 8000P after each processing step. The IR spectra from 700 to 950 cm^{-1} are shown in Figure 5.12, and three peaks corresponding to asymmetric and symmetric epoxide ring stretches were observed at 913, 844, and 760 cm^{-1}. Between soft bake and post-exposure bake, minimal conversion of epoxy occurs suggesting that little cross-linking has occurred. After curing at 225°C, the peak area at 844 and 913 cm^{-1} disappeared signifying that the epoxide rings have reacted and cross-linked with the polymer backbone. An extended cure of the same sample at 250°C for 2 hours showed no significant change in the IR spectra confirming that Avatrel 8000P curing reaction was complete.

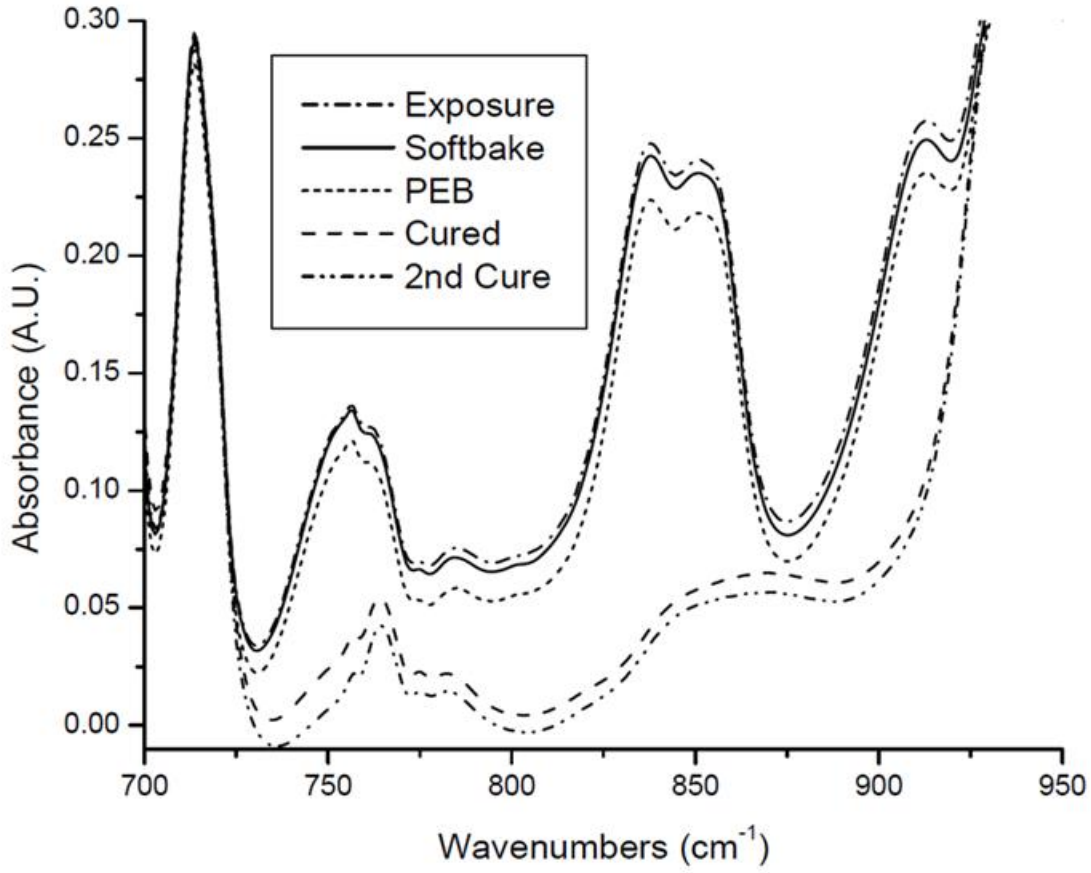

Figure 5.12: Changes in the FT-IR spectrum of Avatrel 8000P from 700 to 950 cm^{-1} as a function of processing steps (soft-bake: 100°C for 5 min., exposure: 500 mJ/cm^2, PEB: 100°C for 5 min., Cure: 1 hour at 225°C, 2nd Cure: 2 hours at 250°C)

The cross-linking reactions have a dramatic effect on the mechanical properties of Avatrel 8000P and also impact the dielectric properties of the polymer. To evaluate the effect of cross-linking, the relative permittivity and loss tangent of cured Avatrel 8000P films were characterized for different processing conditions. For a fixed exposure dose of 500 mJ/cm^2, the loss tangent and dielectric constant decreased with an increase in cure temperature, as shown in Figure 5.13.

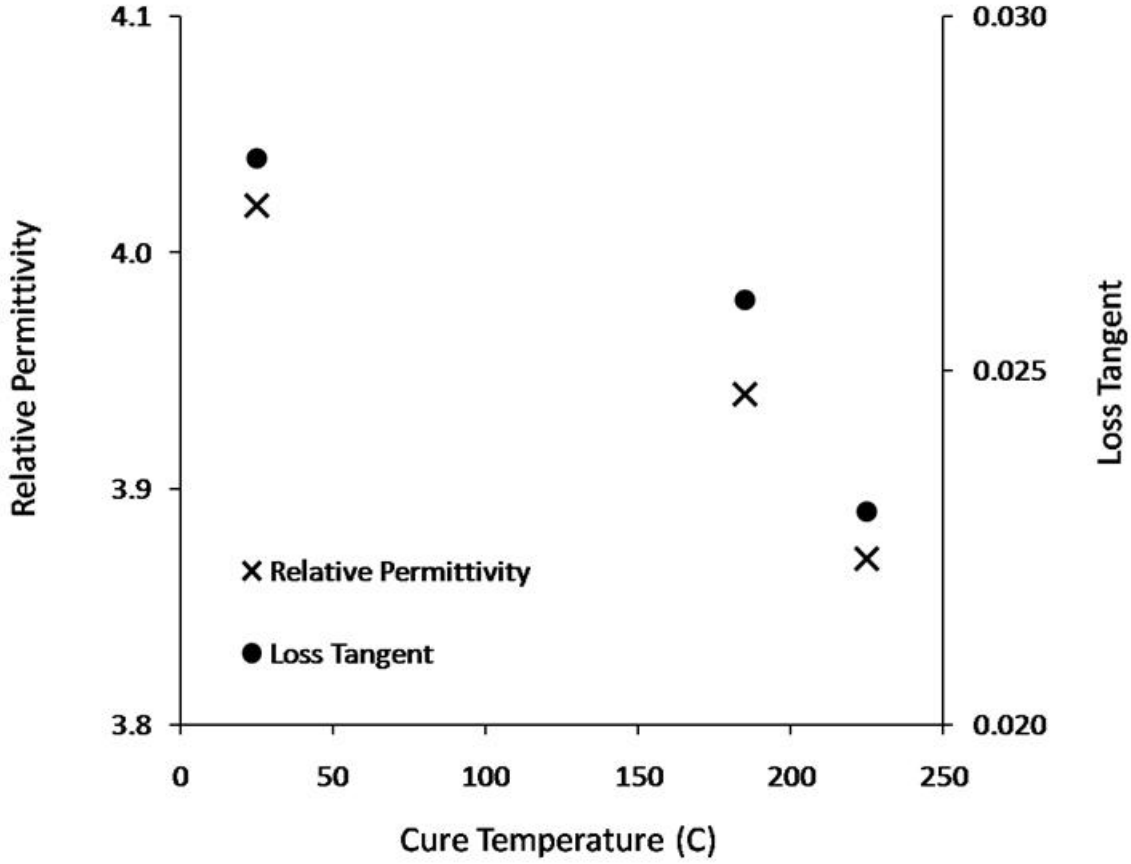

Figure 5.13: Relative permittivity and loss tangent of Avatrel 8000P at cure temperatures of 25°C, 185°C and 225°C

The decrease in the dielectric constant at higher cure temperatures is likely due to increased polymer interconnectivity and a decrease in film polarizability (electron and dipole polarization) when the epoxy is completely cured. Since the C-O in the epoxy ring has a dipole moment of 0.7 which is higher than the dipole moment of the C-C (0.0) and C-H (0.4) bonds, complete reaction of the epoxy rings minimizes dipole polarization. Therefore, curing Avatrel 8000P at 225°C resulted in the lowest measured dielectric constant, ε_r=3.9, which concurs with the high modulus of 2.9 GPa and a high extent of cross-linking.

To evaluate the impact of exposure dose, Avatrel 8000P samples were processed: (i) without an exposure dose, (iii) an exposure dose of 100 mJ/cm^2 and (iii) an exposure dose of 500 mJ/cm^2. All measurements were conducted after a post-exposure bake and cure at 225°C. Figure 14 shows that the unexposed Avatrel 8000P sample had a dielectric constant of 4.0 and loss tangent of 0.030, where as the two samples that had UV exposure both had a dielectric constant of 3.9 and loss tangent of 0.023. The thermal reaction of the photo-acid generator for the unexposed sample resulted in different products and reaction rates than the samples with photolitically reacted PAG. In the unexposed Avatrel 8000P sample, a high concentration of unreacted epoxy groups along with lower polymer interconnectivity resulted in an increase of the overall dipole polarization and permittivity [98].

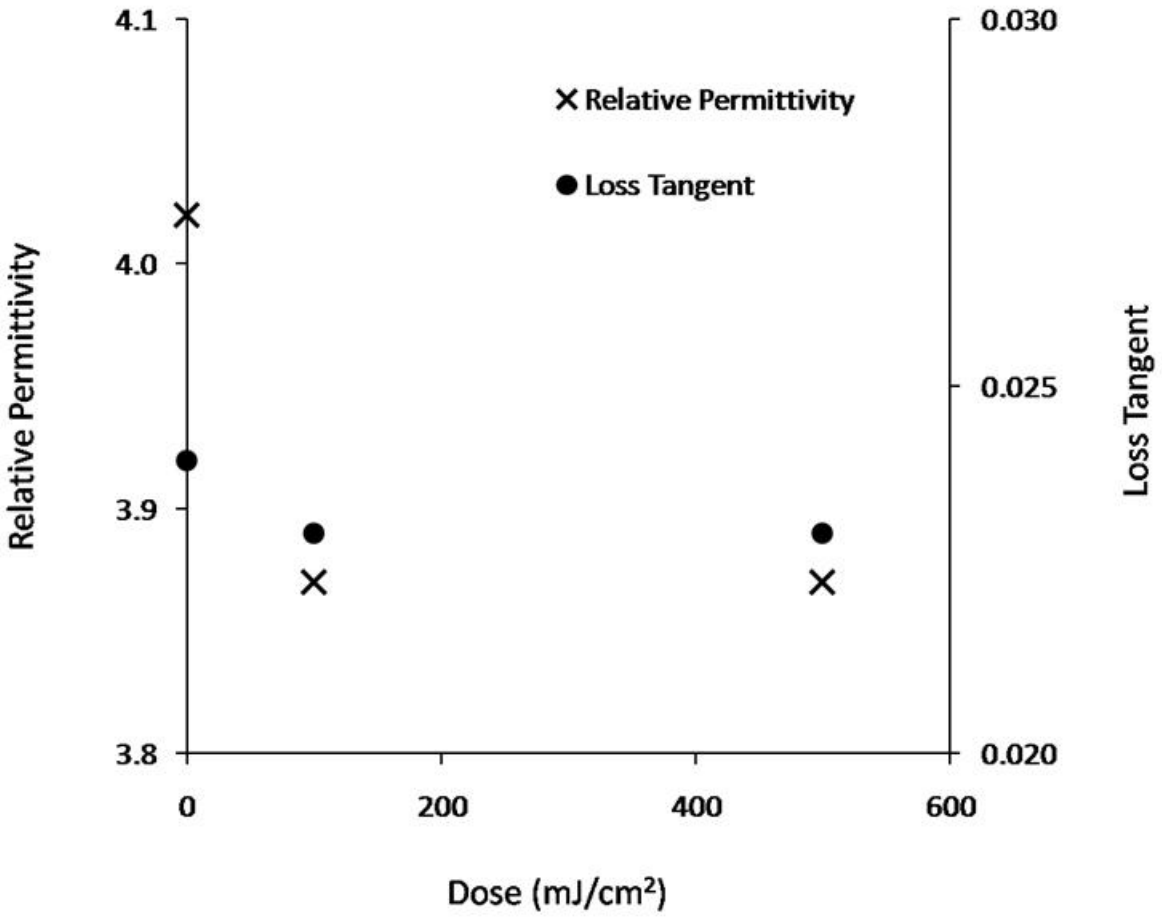

Figure 5.14: Relative permittivity and loss tangent of Avatrel 8000P processed: without an exposure dose, an exposure dose of 100 mJ/cm^2 and an exposure dose of 500 mJ/cm^2 and measured after PEB and cure at 225°C

The dielectric constant of Avatrel 2000P is 2.55 [115] and the dielectric constant of SU-8 is 3.2 [110-111] which are both lower than the dielectric constant of Avatrel 8000P. The higher dielectric constant of Avatrel 8000P is first attributed to its polar side groups: the fluorinated alcohol group and the carbonyl group. Additionally, the multifunctional cross-linker also causes Avatrel 8000P to have a higher dielectric constant than Avatrel 2000P and SU-8.

The residual stress of Avatrel 8000P films ranged from 9 MPa after soft bake to 26 MPa after curing, as shown in Figure 5.15.

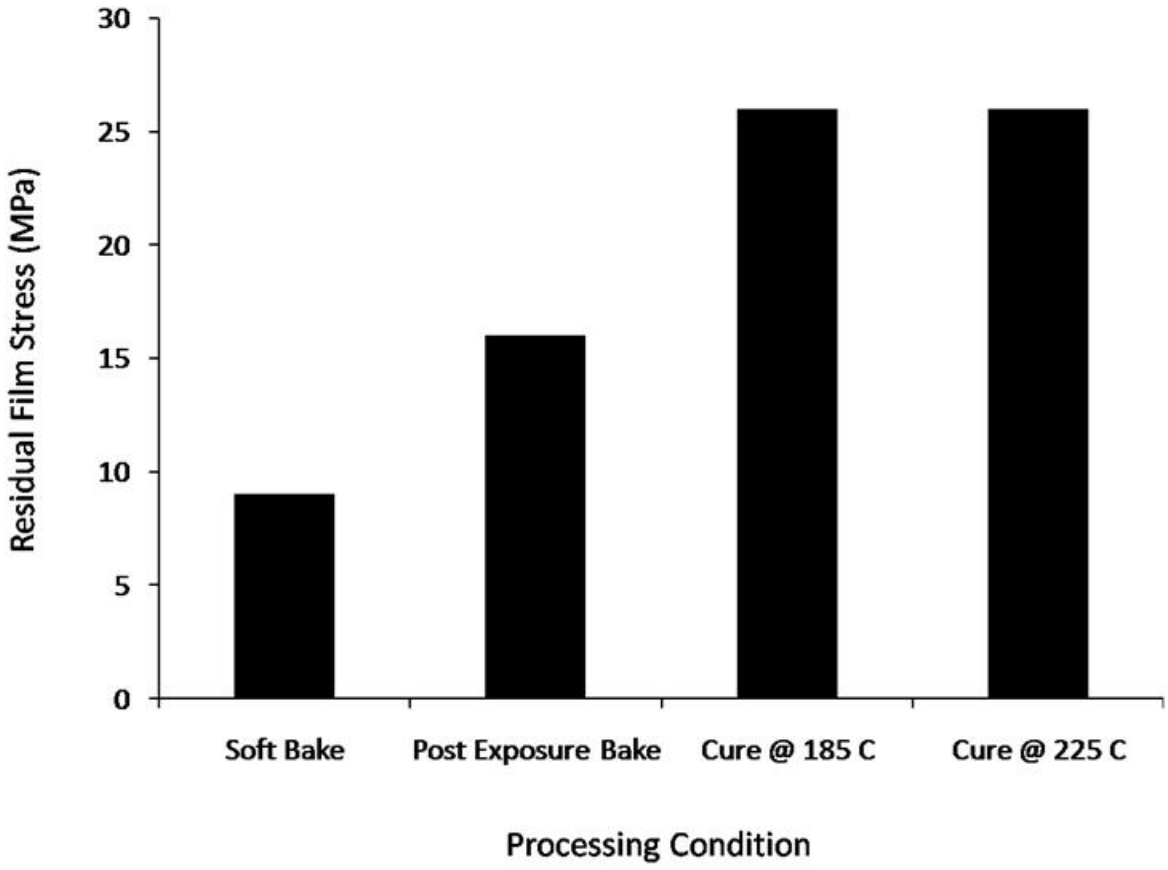

Figure 5.15: Changes in internal film stress of Avatrel 8000P as a function of different processing conditions (soft-bake: 100^{o}C for 5 min, PEB: 100^{o}C for 5 min, Cure 1: 185^{o}C for 1 hour, Cure 2: 225^{o}C for 1 hour)

After soft-bake, residual stress in the film is primarily due to solvent removal. After post exposure bake, the Avatrel 8000P film stress increases because UV exposure initiates photo-acid generator decomposition, and cross-linking is initiated. The high residual stress after cure is due to the high cross-link density of the polymer. Avatrel 2000P has a much lower epoxy content and therefore much lower residual stress values ranging from 2 MPa after softbake to 6 MPa after cure [98]. SU-8 which also has a high

epoxy content has a residual stress of 18 MPa after post exposure bake which is comparable to Avatrel 8000P [116].

In addition to mechanical integrity, a polymer film must also have a high level of thermal stability for the successful implementation of polymer microstructures in MEMS and microelectronics applications. To evaluate the thermal stability of Avatrel 8000P, the decomposition versus temperature of Avatrel 8000P was characterized through thermogravimetric analysis. Figure 5.16 shows thermogravimetric analysis of Avatrel 8000P at ramp rates of 0.5^{o}C/min and 5^{o}C/min. The apparent decomposition temperature shifts to lower values with slower ramp rates due to the longer time spent at each temperature.

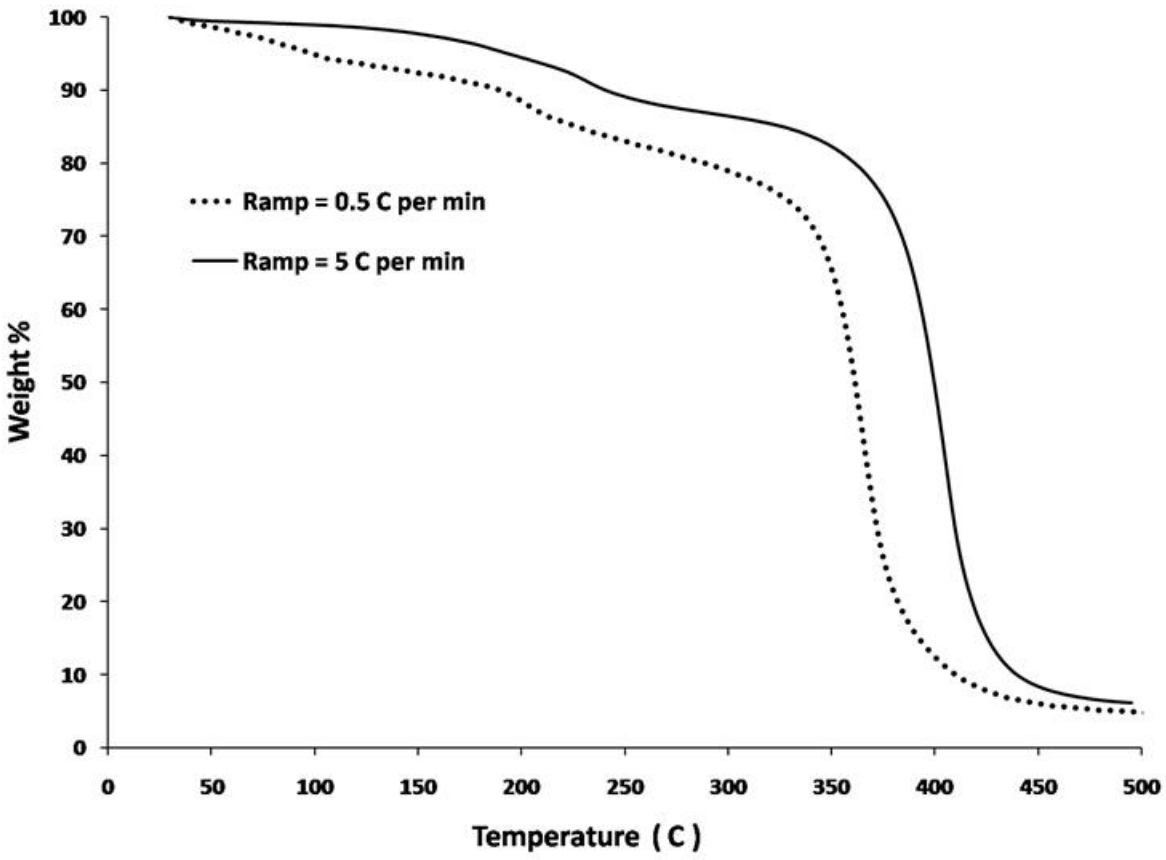

Figure 5.16: Thermogravimetric analysis of Avatrel 8000P

5.4 Conclusion

Avatrel 8000P is a high contrast, i-line sensitive polynorbornene that can be developed in traditional aqueous-base developers. The simple baking procedures make Avatrel 8000P easier to process than Avatrel 2000P and SU-8. Also, the ability to develop Avatrel 8000P in aqueous base can reduce cost and chemical waste. As shown by SEM images, high fidelity structures with aspect ratios of 7:1 can be fabricated in thick films with vertical sidewalls. Due to its high level of cross-linking and polar side groups, Avatrel 8000P has a greater dielectric constant than Avatrel 2000P and SU-8. Avatrel 8000P and SU-8 which both have a high epoxy content have comparable

mechanical strength and residual stress. The excellent photo-definition properties of Avatrel 8000P, its high mechanical strength, and thermal stability make it a suitable candidate for MEMS and microelectronics packaging.

CHAPTER 6

ENHANCED PHOTO-PATTERNING OF POLYMER DIELECTRICS VIA IMPRINT LITHOGRAPHY

6. 1 Introduction

Development of a process to fabricate high aspect ratio polymer molds for copper electroplating interconnects could enable improved IC electrical performance and reliability. However, high aspect ratio photo-processing of thick polymers is difficult with traditional photolithography techniques. Thick films suffer from light scattering, resulting in poor resolution compared to thin films. Furthermore, high aspect ratio hollow pillars are challenging to fabricate with photolithography because the transport of the developer in the core is slow in comparison with the transport of developer around the perimeter of the feature. As a result, hollow core pillars require longer development times than solid pillars of comparable aspect ratios, and at high aspect ratios delamination of the structure occurs before the core can be fully developed.

A novel fabrication method has been developed to produce high aspect ratio, complex structures for highly effective electrical input/output interconnections. This fabrication method combines imprint lithography and photolithography to improve the photo-patterning of polymer dielectrics for high aspect ratio hollow structures. In the photo-imprint process, a transparent stamp with surface relief structures is brought into contact with a photosensitive material. Temperature and pressure are applied to cause the photosensitive material to fill the mold, and ultra-violet light is then emitted to pattern the polymer. To develop high aspect ratio hollow pillars, a shallow photo-imprint stamp has

been developed to physically move material in the polymer core. Since the imprint stamp displaces material in the area of the feature, the effective film thickness is reduced compared to the bulk film. The reduction in film height reduced the effects of scattering in the core and also facilitated transport of developer within the core. The photo-imprint lithography process fabricated high aspect ratio hollow core pillars that exceeded optical resolution capabilities.

6.2 Experimental

Schematics of the photo-imprint stamp fabrication and imprint process are provided in Appendix B. To create the initial photo-imprint stamp, a glass substrate was sputtered with a full seed layer of chrome in the CVC DC Sputterer to a thickness of 1000 Å. The glass substrate was patterned with SC 1813 (Shipley). The SC 1813 was spin-coated to a thickness of 1.5 μm soft baked at 90°C for 3 minutes on a hotplate. The resist was photo-patterned at 100 mJ/cm^2 using the Karl Suss MA-6 Mask Aligner which uses a 350 W mercury lamp that exposes across the spectrum 230 nm to 400 nm. The sample was then developed in MF-319 (Shipley) to define the collar pattern. The chrome was patterned using chromium etchant CR-7 (Cyantek) and the SC 1813 was stripped in acetone. The sample was then sputtered with a full seed layer of Ti/Au/Ti (300Å/3000Å/300Å) using the Unifilm Sputterer. The glass substrates were then patterned with AZ-4620 (AZ Electronic Materials) to pattern the molds for electroplating. The AZ-4620 was spin-coated to a thickness of 40μm and soft baked at 100°C for 30 minutes on a hotplate. The resist was photo-patterned at 1000 mJ/cm^2 using the Karl Suss MA-6 Mask Aligner. The sample was then developed in AZ-400K (AZ Electronic Materials) to define the mold for electroplating. The titanium in the exposed region was

wet etched back using buffered oxide etch solution, and gold pillars were electroplated. The AZ4620 was stripped in acetone, and the titanium seed layers were etched back in buffered oxide etch solution. The gold seed layer was etched back in a 1:2:10 - I_2:KI:H_2O solution. The photo-imprint stamp was coated with (3,3,3-trifluoropropyl)dimethylchlorosilane (Gelest) and then baked at 90°C for 3 minutes.

To create the photo-imprint stamp for imprinting into Avatrel 8000P, a glass substrate was sputtered with a full seed layer of chrome in the CVC DC Sputterer to a thickness of 1000Å. The glass substrate was patterned with NR-7 (Futurexx). The NR-7 was spin-coated to a thickness of 2.5 μm soft baked at 150°C for 5 minutes on a hotplate. The resist was photo-patterned at 400 mJ/cm^2 using the Karl Suss MA-6 Mask Aligner. The sample was then post-exposure baked for 5 minutes at 100°C and developed in RD-6 (Futurexx) to define the collar pattern. The chrome was patterned using chromium etchant CR-7 (Cyantek) and the NR-7 was stripped in acetone. The sample was then sputtered with a full seed layer of Ti/Cu/Ti (300Å/3000Å/300Å) using the CVC DC Sputterer. The glass substrates were then patterned with NR-9 (Futurexx) to pattern the molds for electroplating. The NR-9 was spin-coated to a thickness of 10 μm and soft baked at 110°C for 15 minutes on a hotplate. The resist was photo-patterned at 400 mJ/cm^2 using the Karl Suss MA-6 Mask Aligner. The sample was then post-exposure baked for 20 minutes at 110°C and developed in RD-6 (Futurexx) to define the mold for electroplating. The titanium in the exposed region was wet etched back using buffered oxide etch solution, and copper pillars were electroplated. The NR-9 was stripped in acetone and the titanium seed layers were etched back in buffered oxide etch solution. The copper seed layer was etched back in a 3% sulfuric acid and 3% hydrogen peroxide

solution. The photo-imprint stamp was coated with Teflon AF and baked at 115°C for 10 minutes to drive off solvent.

Avatrel 2000P samples were spin-coated to varying thicknesses. The soft bake time and exposure doses were varied depending on the thickness of the material. The soft bakes were conducted on a hotplate at 100°C and post exposure bakes were conducted in an oven at 100°C for 20 minutes. Avatrel 2000P samples were developed in BIOACT EC-7R Defluxer (Petroferm) in an ultrasonic bath. Avatrel 8000P samples received varying soft bake times and exposure doses depending on the thickness of the material. The soft bakes were conducted on a hotplate at 100°C and post exposure bakes were conducted on a hotplate at 100°C for 5 minutes. Avatrel 8000P was developed in MF-319 (Shipley) via puddle or ultrasonic bath.

All imprinting was conducted in the Obducat Imprint Lithography System and exposures were conducted in the Karl Suss MA-6 Mask Aligner. The Hitachi 3500H was used to obtain SEM images of the processed films. The Wyko non-contact profilometer was used to obtain profile information on the samples. DSC data was obtained using the TA instruments Q20, and samples were ramped from room temperature to 300°C at a ramp rate of 5°C/min.

6.3 Results and Discussion

A photo-imprint process was developed to develop high aspect ratio, hollow core pillars shown in Figure 6.1.

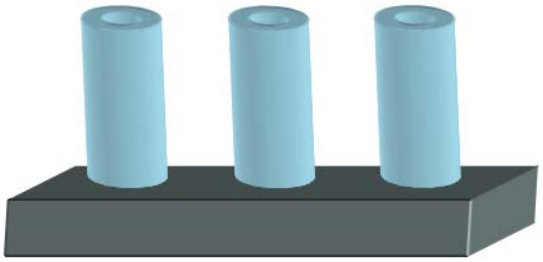

Figure 6.1: Schematic of a high aspect ratio, hollow core pillar

Guo and coworkers noted that by using a combined imprint lithography and photolithography process, the aspect ratio of the resist patterns could have a higher aspect ratio than the feature on the stamp [17]. By using an imprint stamp with a photo-pattern and protrusions that do not transmit light, it is possible to keep a negative tone material from cross-linking beneath the relief features of the stamp. The negative tone material can then be dissolved like an unexposed negative resist, resulting in chemical selective removal of the residual layer [17,117]. Furthermore since a shallow imprint process is used, a polymer layer exists between the stamp protrusions and the surface of the substrate and acts as a cushion, reducing the likelihood of the stamp being damaged.

The combined photo-imprint process was evaluated with Avatrel 2000P to pattern hollow core pillars. The chemical structure of Avatrel 2000P is shown in Figure 4.2 (a) and a more detailed discussion of the structure and material properties is provided in Chapter 4 and Chapter 5. DSC data was conducted of soft-baked Avatrel 2000P films to assess the T_g of the material and ascertain an imprint processing window. No clear T_g could be determined from the data in Figure 6.2, but it did show that the material thermally cross-links at temperatures above 150°C.

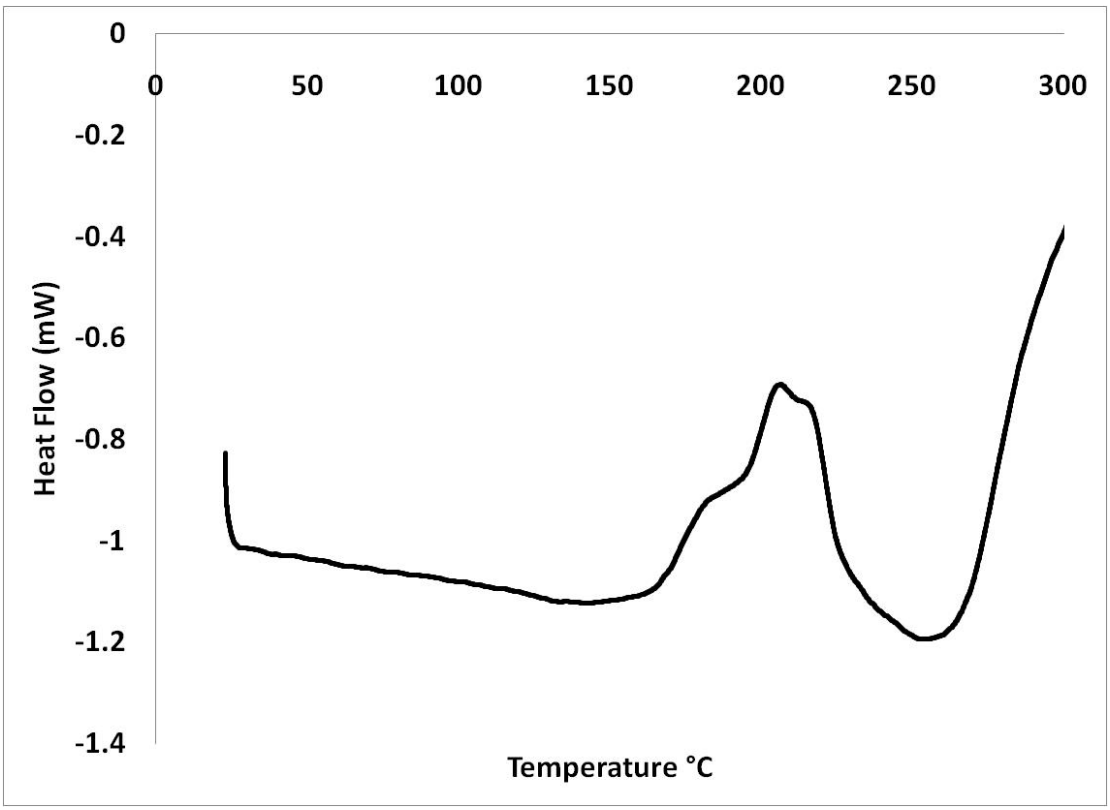

Figure 6.2: DSC data of Avatrel 2000P with a ramp rate of 5°C per minute

Thermal imprinting was conducted to establish imprint parameters that generated high fidelity replicas of the stamp and promoted easy separation between the stamp and substrate. A 7 μm stamp coated with a (3,3,3-trifluoropropyl)dimethylchlorosilane release agent was imprinted into a soft baked 12 μm film of Avatrel 2000P. An operating pressure of 15 bar was initially selected, as it was the minimum operating pressure on the tool. An imprint time of 10 seconds was selected to maintain high throughput. Temperature was varied and the patterns were assed for fidelity, field planarity, and ability to separate without damaging the stamp or substrate. Below 90ºC, the imprint could not be completed in ten seconds and above 115ºC, the stamp and the substrate

could not be separated. Figures 6.3 and 6.4 show microscope images of the thermal imprint sample at 90°C, 15 bar, 10 seconds and 115°C, 15 bar, 10 seconds, respectively.

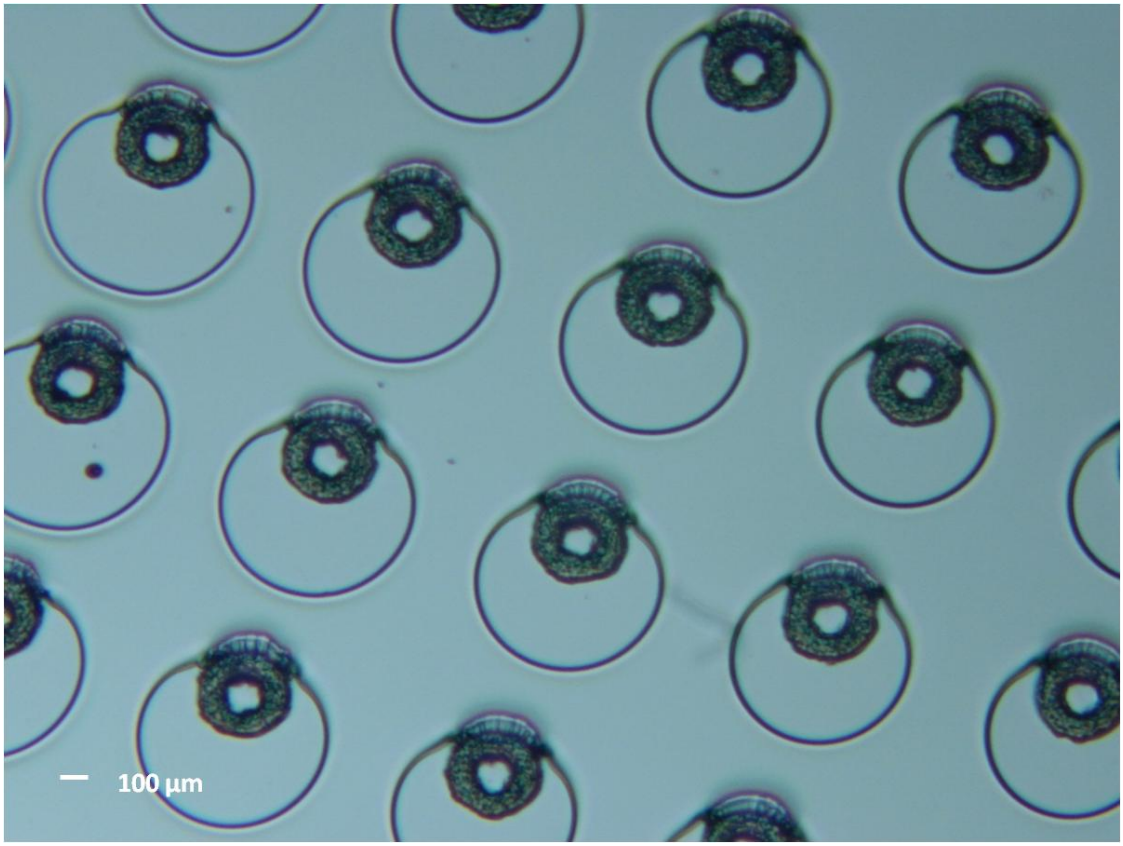

Figure 6.3: Avatrel 2000P sample imprinted at 90°C, 15 bar for 10 seconds

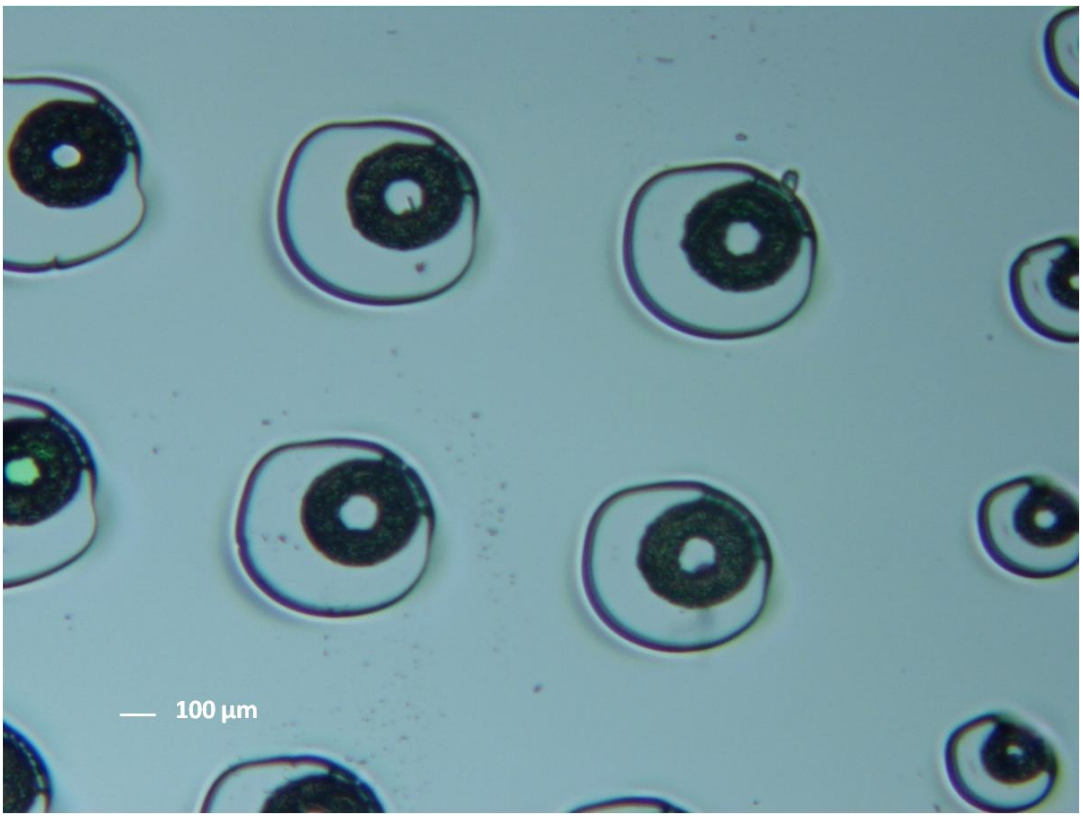

Figure 6.4: Avatrel 2000P sample imprinted at 115°C, 15 bar for 10 seconds

Both imprint conditions transferred the 7 µm protrusion into the film of Avatrel 2000P. The sample imprinted at 115°C had smaller residual flow fields around the pillar than the sample imprinted at 90°C. However, Avatrel 2000P had a strong adhesion to the stamp even with the anti-adhesion agent, and its adhesiveness increased with increasing imprint temperature. As a result, more damage was caused to the stamps imprinted at 115°C. Subsequent imprinting into Avatrel 2000P was therefore conducted at 90°C, 15 bar for 10 seconds.

To assess the ability of imprint lithography to improve the aspect ratio of patterned features, a 60 µm photo-imprint stamp was imprinted into a 125 µm soft baked film of Avatrel 2000P at 90°C, 15 bar, 10 seconds. The sample was then photo-patterned

in the imprint tool with an exposure dose of 200 mJ/cm^2 exposure dose. After separation, the sample was post exposure baked for 20 minutes in an oven at 100°C and ultrasonic developed in BIOACT EC-7R for two minutes. As shown in Figure 6.5, the shallow 60 μm photo-imprint stamp was able to clear the full 125 μm polymer core. The height to width ratio of the stamp was approximately 0.6, and the pattern on the substrate had a ratio of 1.25 which is more than a two fold increase in aspect ratio. However, the photo-pattern had poor fidelity when compared to structures made with photolithography. The Obducat imprint lithography tool has a broad band UV lamp with an intensity of 200 mW/cm^2, making it difficult to refine the dose to achieve the optimal dose for materials. Additionally, the exposure was conducted at the imprint temperature and pressure. These issues make it difficult to fairly compare the photo-imprint process with the performance of a material patterned with photolithography. Furthermore, Avatrel 2000P as noted in Chapter 5 has a modulus of 1.0 GPa which makes it too soft to fabricate mechanically compliant molds for copper electroplating.

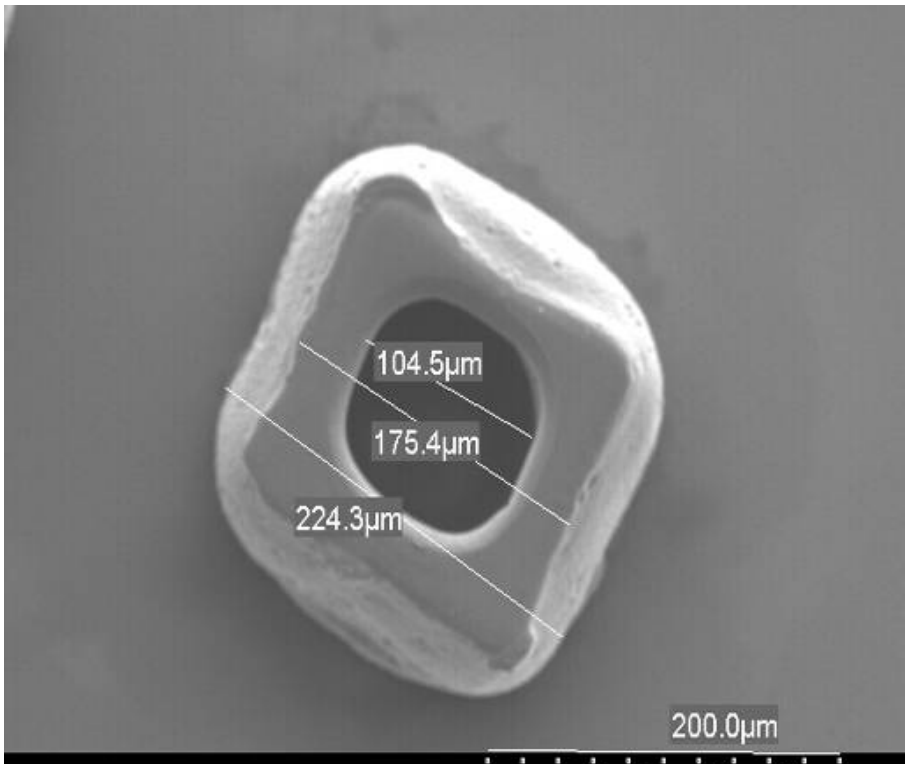

Figure 6.5: Avatrel 2000P sample photo-imprinted at 90°C, 15 bar, 10 seconds and an exposure dose of 200 mJ/cm^2

The polynorbornene polymer Avatrel 8000P shown in Figure 5.2 had a modulus of 2.9 GPa and also demonstrated a high contrast of 12.2 and high aspect ratio structures. Avatrel 8000P was used to evaluate how the photo-imprint lithography process compares with optical resolution capabilities. A feature set that could not be fabricated with optical lithography was characterized and then tested with the photo-imprint lithography process. Hollow core pillars shown in Figure 6.1 were first attempted using photolithography. A film of Avatrel 8000P was spin coated to a thickness of approximately 30 µm onto a silicon oxide substrate and soft baked at 100°C for 5 minutes on a hotplate. Features with a 10 µm wide core and a total diameter of 30 µm were attempted. Exposures of 500 mJ/cm^2, 400 mJ/cm^2, and 300 mJ/cm^2 and two different development techniques were tested. To determine the optimal development time for the samples, testing with an

optical dissolution rate monitor was attempted. However, the material became very rough during development making the thickness difficult to quantify. To establish a minimum development time, films of Avatrel 8000P were spin coated and then soft baked and puddle developed. The un-patterned film developed completely in MF-319 in 2 minutes and 15 seconds. The photo-patterned samples were developed for 2 minutes and 30 seconds since significant delamination of features occurred with longer development times.

Table 6.1. Height profiles for varying exposure and development times with Avatrel 8000P

Dose (mJ/cm^2)	Develop Type	Time (min:sec)	Core Height (μm)
500	Puddle	2:30	24.85 ± .47
400	Puddle	2:30	17.67 ± .19
400	Ultrasonic	2:30	15.03 ± .12
300	Puddle	2:30	17.37 ± .31

The profile data of the features is summarized in Table 6.1; a height of zero represents the wafer/polymer interface, a height of 28 μm represents the top of the film. At an exposure dose of 500 mJ/cm^2, the core height is 24.85 μm suggesting that only about 3 μm developed. For an exposure dose of 400 mJ/cm^2, the core height was 17.67 μm suggesting that about 10 μm of material developed. The decrease in core height with a decrease in exposure dose suggests that at 500 mJ/cm^2 there is scattering within the core that hinders development of the feature. However, lowering the dose further to 300 mJ/cm^2 did not decrease the height of material in the core appreciably. Therefore, ultrasonic development was attempted at 400 mJ/cm^2. Samples developed in the ultra-

sonic bath, had a height of 15.03 μm suggesting that transport within the core does impact the ability to pattern the geometry.

To fabricate a photo-imprint stamp, a glass wafer was sputtered with chrome and then photo-patterned to have the same photo-pattern as the mask used in photolithography. Copper pillars were electroplated in the center of the collar to physically displace material during imprint and also eliminate the need for alignment. Since the mold for imprint lithography has a high density of protrusions on its surface, it has a high total surface area in contact with the imprinted polymer which makes it possible for the polymer to adhere to the stamp. Due to the difficulty separating Avatrel 2000P from the stamp with (3,3,3-trifluoropropyl)dimethylchlorosilane, another anti-adhesion layer was used for this application. Researchers have noted that fluorosilane layers applied to UV imprint stamps have been shown to be attacked by different photosensitive materials [40]. Therefore, Teflon AF was used as an anti-reflective coating and a mold release coating. The material has excellent light transmission from the deep UV range out through visible spectrum, and because it does not absorb light, it will not deteriorate with exposure to light [85].

To enable mold filling, thermal imprint lithography is typically conducted at 50-70°C higher than the glass transition temperature of the imprint material [48]. DSC analysis was conducted of soft-baked films of Avatrel 8000P to determine the processing window for the material and is shown in Figure 6.6. There is a slight inflection in the graph around 70°C, and the material begins thermally cross-linking at approximately 140°C.

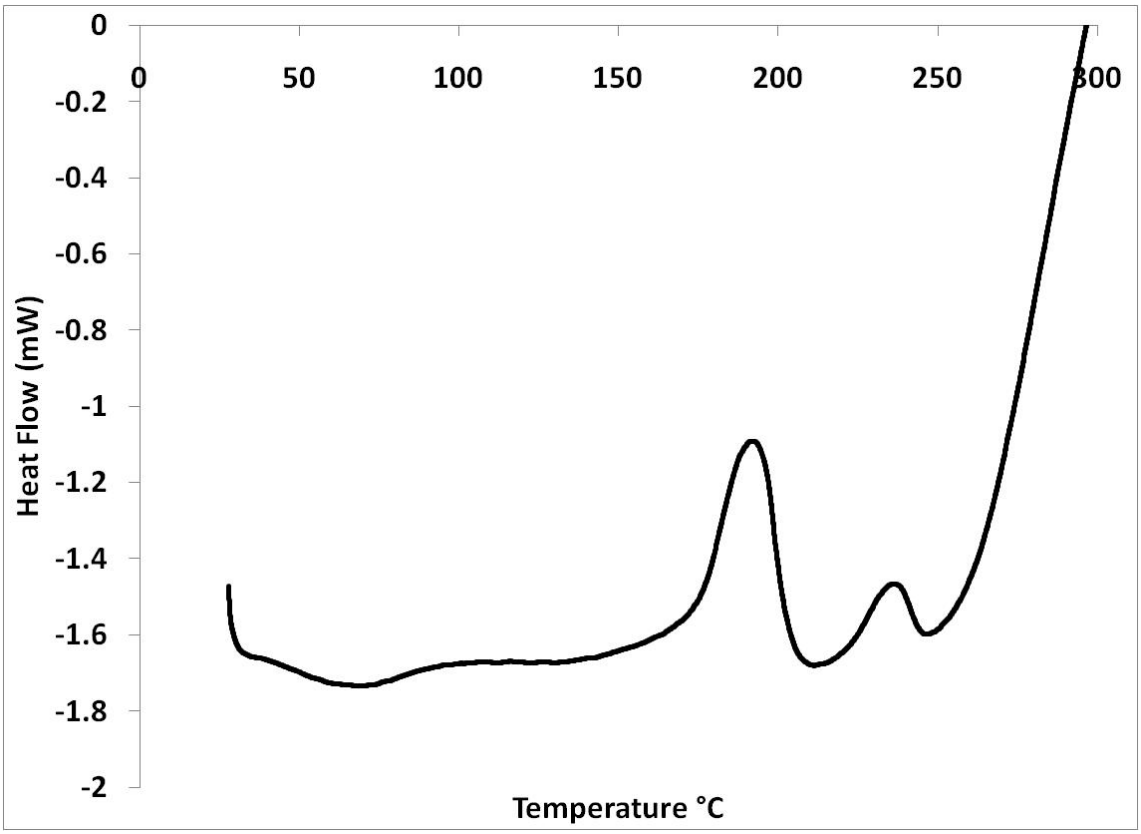

Figure 6.6: DSC data of Avatrel 8000P with a ramp rate of 5°C per minute

To determine the optimal temperature for imprint, a stamp with 15-16μm tall copper pillars was imprinted into a 30 μm film of Avatrel 8000P at 45 bar for 60 seconds for incremental temperatures shown in Figure 6.7. Imprinting at 150°C displaced the full height of the stamp, however imprinting at this condition initiated thermal cross-linking of the material, and samples that had no exposure would not develop. Imprinting at 125°C, 45 bar for 60 seconds, did not displace the full height of the stamp, and increasing time or pressure did not cause the stamp to displace its full height. Due to viscous polymer flow, the large-scale protrusion patterns cannot fully penetrate the polymer yielding a reduced aspect ratio than intended[117]. However, thermal cross-linking of the

material was not initiated at this temperature, and therefore subsequent imprints were conducted at 125°C, 45 bar for 60 seconds.

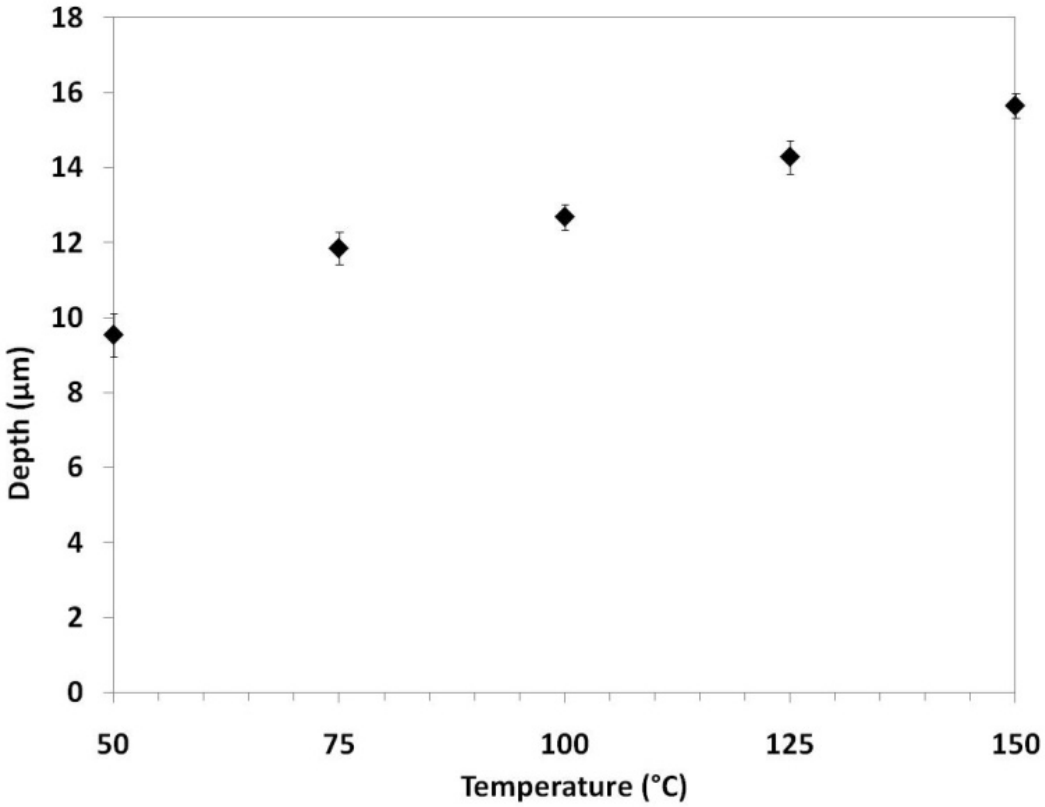

Figure 6.7: Depth vs. Temperature for thermal imprinting into Avatrel 8000P at 45 bar and 60 s

To evaluate the impact of incomplete pattern transfer on field planarity, a non-contact profilometer was used to profile the height around the features, immediately after imprinting but before photo-patterning the sample. The depth profiles were averaged for 10 similar features using the profilometer software. A cross-sectional view of the feature is shown in Figure 6.8 for the averaged data.

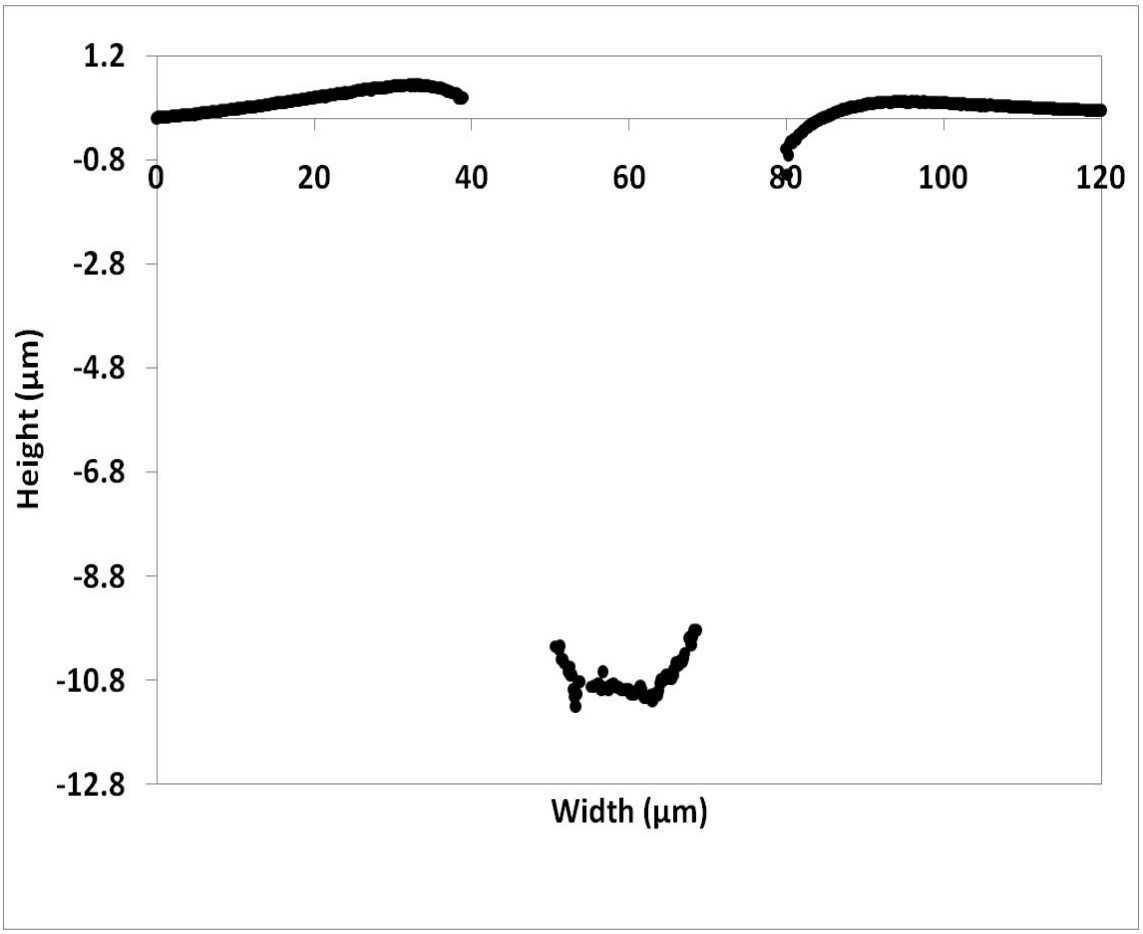

Figure 6.8: Depth profile for thermal imprinting into Avatrel 8000P at 125°C, 45 bar, and 60 s

Zero refers to the top of the film in Figure 6.8, and the material displaced by the copper pillar appears to buildup around the feature. Examination of the data suggests that approximately a half micrometer of non-planarity exists around the imprinted feature. The non-contact profilometer uses the phase change of light reflecting from various heights of similar materials to measure the uniformity of a flat surface or the horizontal distance between two adjacent surfaces. There is little sidewall profile data since light that reflects from the sidewalls are not captured by the sensor.

To compare the performance of photo-imprinting with photolithography, Avatrel 8000P samples were imprinted in the tool at 125°C, 45 bar for 60 seconds and then exposed in the Karl Suss MA-6 Mask aligner. After separation, the samples were puddle developed for 2 minutes and 30 seconds. As shown in Figure 6.9, a non-contact profilometer was used to grey-scale map the height of the imprint patterned feature. In the top down view of the photo-imprinted feature, the black refers to the silicon oxide substrate and the grey to the top of the feature. The core of the pillar is also black suggesting that the pillar has been fully developed.

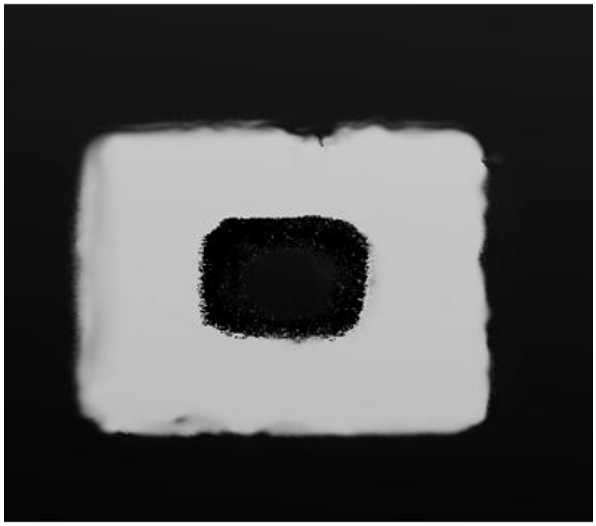

Figure 6.9: Grey-scale map of the height of the photo-imprinted feature into Avatrel 8000P at 125°C, 15 bar, 60 seconds, exposure dose of 500 mJ/cm^2 and puddle develop for 2 min 30 s

Two dimensional height analysis was also conducted of the feature to confirm that the core had cleared and a cross-section of the feature in Figure 6.9 is shown in Figure 6.10. The photo-imprint process was able to fully develop the hollow core pillar with a (height to width) aspect ratio of 2.8 which was not possible with photolithography.

The photo-imprint process reduced scattering within the core and also facilitated development within the core by displacing material.

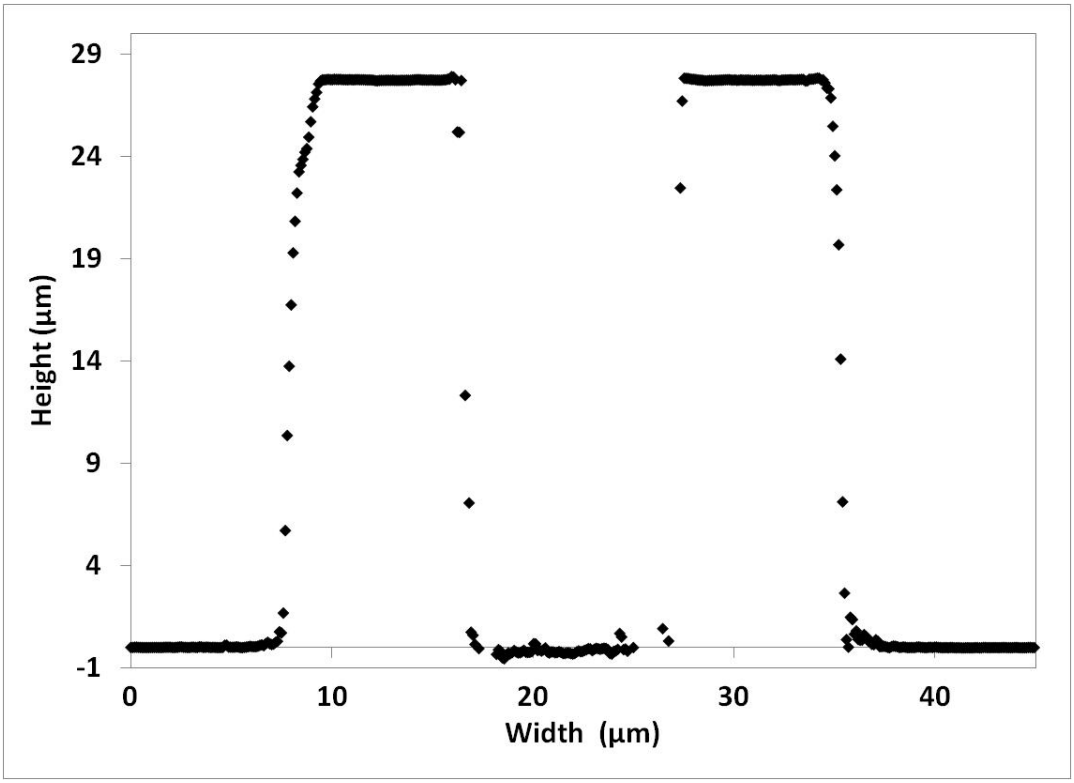

Figure 6.10: Two dimensional height profile of the photo-imprinted feature into Avatrel 8000P at 125°C, 15 bar, 60 seconds, exposure dose of 500 mJ/cm^2 and puddle develop for 2 min 30 s

Imprint lithography demonstrated the ability to enhance the photo-patterning of polymer dielectrics such as Avatrel 2000P and Avatrel 8000P. Avatrel 2000P and Avatrel 8000P have polynorbornene backbones, but have different optical, mechanical, and electrical properties as discussed in Chapter 5. The mechanical properties of Avatrel 2000P and Avatrel 8000P were evaluated to assess their impact on imprinting. As noted in Chapter 5, the modulus and hardness of cured Avatrel 2000P are 1.0 GPa and 0.04 GPa respectively, and the modulus and hardness of cured Avatrel 8000P are 2.9 GPa and

0.18 GPa respectively. To evaluate the mechanical properties of the soft-baked materials, nano-indentation of both materials was conducted at a force of 1000 μN and the load versus displacement is shown in Figure 6.11.

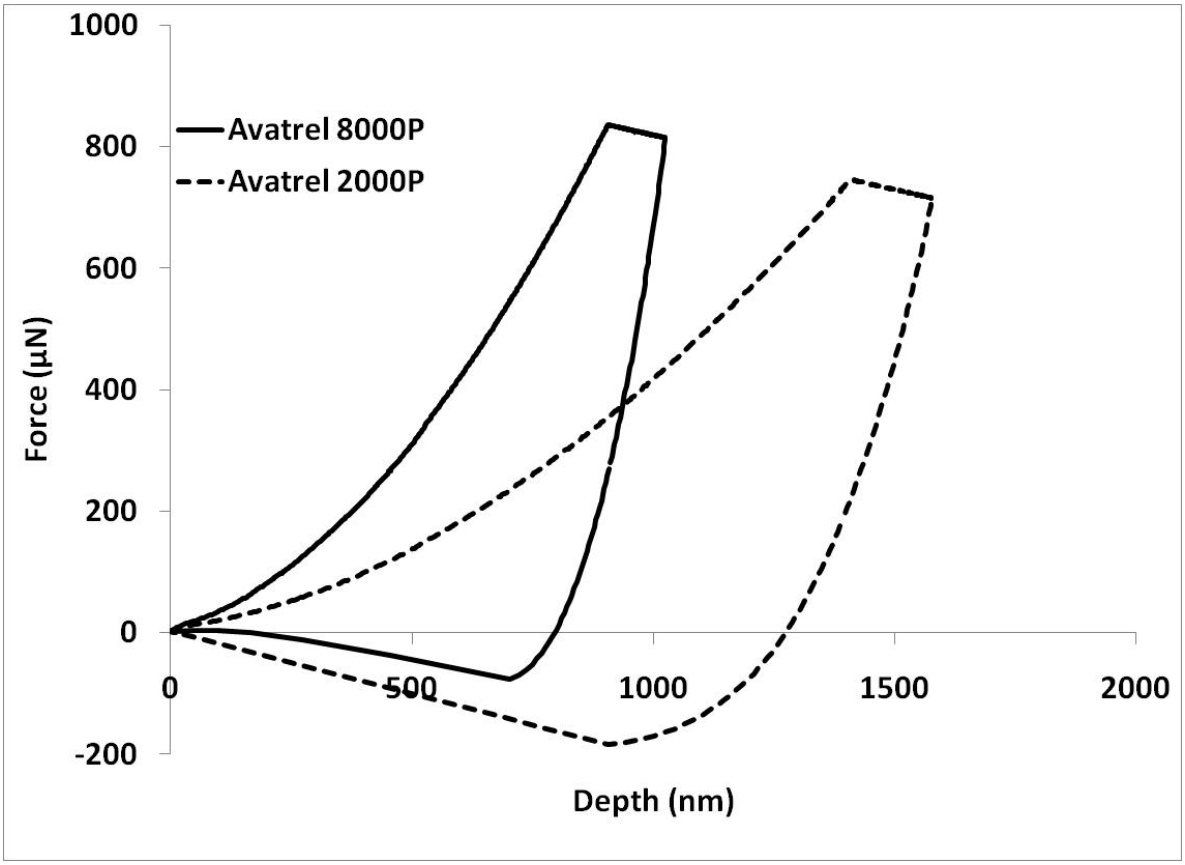

Figure 6.11: Force versus displacement curves with a maximum force of 1000 μN for Avatrel 8000P (solid line) and Avatrel 2000P (dashed line) after soft-bake

The modulus and hardness of Avatrel 2000P after soft-bake were 0.46 GPa and 0.01 GPa respectively, and the modulus and hardness of Avatrel 8000P after soft-bake were 1.1 GPa and 0.04 GPa respectively. As a result, for a given force Avatrel 2000P displaces a greater distance than Avatrel 8000P. The same photo-imprint stamp imprinted into Avatrel 8000P was imprinted into a 30 μm film of Avatrel 2000P at 45 bar for 60 seconds

for incremental temperatures from 50°C to 125°C. The full height of the stamp was displaced at 50°C for Avatrel 2000P, whereas the full height of the stamp was only displaced at 150°C. Avatrel 8000P is four times harder than Avatrel 2000P and therefore required much higher imprint temperatures. As shown by the DSC data, imprint temperatures are limited for photo-sensitive materials by thermal cross-linking. Higher imprint pressures and longer imprint times can compensate for the limited temperature processing window. As shown in this chapter, a 7 μm stamp was able to imprint Avatrel 2000P at 90°C, 15 bar, and 10 seconds, and a 15 μm stamp was able to imprint Avatrel 2000P at 50°C, 45 bar, and 60 seconds. A much taller stamp was able to imprint at a lower temperature in Avatrel 2000P due to the increased imprint pressure and time. Due to the processing limitations of the imprint tool, pressure could not be elevated sufficiently to transfer the full 15 μm height of the stamp in Avatrel 8000P at temperatures below its thermal crosslink temperature.

The non-planarity of Avatrel 2000P and Avatrel 8000P over the range of temperatures was also compared and is presented in Table 6.2.

Table 6.2: Height profiles of non-planarity of Avatrel 2000P and Avatrel 8000P imprint samples at 45 bar, 60 seconds and varying temperatures

	Avatrel 2000P	Avatrel 8000P
Temperature °C	Height (µm)	Height (µm)
50.00	0.18	0.79
75.00	0.24	0.98
100.00	0.20	0.71
125.00	0.11	0.50

The non-planarity around the features varies at the lower temperatures, but both Avatrel 2000P and Avatrel 8000P had the lowest measured non-planarity around the feature at a temperature of 125°C. Avatrel 2000P also consistently had lower levels of non-planarity than Avatrel 8000P.

6.4 Conclusion

A novel fabrication method has been developed to enhance the photo-patterning of polymer dielectrics for high aspect ratio hollow structures. The photo-imprint stamp was able to physically move material in the polymer core and reduce the effective film thickness compared to the bulk film. The reduction in film height reduced the effects of scattering in the core and also facilitated transport of developer within the core. The photo-imprint lithography process fabricated high aspect ratio hollow core pillars that exceeded the resolution of the imprint stamp and the optical resolution. This process was tested with Avatrel 2000P and Avatrel 8000P, and correlations between the mechanical properties of the materials and imprint behavior were also assessed.

CHAPTER 7

IMPRINT LITHOGRAPHY AND MICROELECTRONICS PACKAGING

7. 1 Summary and Conclusions

Imprint lithography is an emerging research area with applications ranging from nano-scale IC fabrication to sensors, biochips and optics [5,13,51]. In this thesis, the capability of imprint lithography to produce complex three-dimensional patterns has been used to enable advanced packaging applications. Specifically, imprint lithography has been employed to fabricate metal-clad encapsulated, air dielectric layers to enable low loss, off-chip, electrical signal lines and high aspect ratio hollow core polymer molds to facilitate the electroplating of dense all copper chip to board interconnections.

7.1.1 Ultra-Low Loss Transmission Lines

As the operating frequency of off-chip signals increases, low-loss structures are needed to enable fast interconnections. The three primary types of losses in transmission lines are conductor loss, dielectric loss, and radiation loss; losses can also occur due to reflections and discontinuities. The inclusion of an air can mitigate dielectric loss and lower the loss contributions of the conductor [7]. Additionally confining electromagnetic fields with metallic shielding can reduce radiation losses [7]. Traditional structures such as the microstrip line with a dielectric layer between the conductor and ground are not viable for high frequency applications. Researchers have demonstrated techniques to incorporate air dielectric layers by suspending the conductor on posts and demonstrated

metallic shielding over traditional microstrip lines [71-72]. However, these structures are only viable as top layer structures and lose their benefit if encapsulated.

In this work, imprint lithography has been used to fabricate an innovative structure that incorporates smooth transitions, metallic shielding, and encapsulated air dielectric layers. This structure is the first report to incorporate all of these features to enable ultra-low loss transmission lines. To fabricate smooth transitions, the reflow properties of solder were used to create a semi-circular stamp and imprint lithography was used to transfer the pattern into Avatrel 2000P. Good pattern fidelity and field planarity was achieved which can reduce reflections and discontinuities enabling high quality data channels. The potential exists to simultaneously form the line and via which could reduce masking, plating and registration steps. Metal shielding was electroplated and patterned using mechanical polishing and wet etching. The sacrificial polymer PPC was used to incorporate air dielectric layers, and imprint lithography was used to planarize the PPC layer over the semi-circular trench. Imprint lithography can fabricate uniform dielectric material layers which can improve line definition and allow lower tolerances for impedance control. The PPC was patterned using a unique interaction of the PPC with copper, and a layer of POSS was used to suspend a copper transmission line over the structure. The PPC was decomposed through the POSS layer using a constant weight decomposition recipe. The decomposition temperatures are compatible with board materials, but one limitation of this process is the long decomposition time required to prevent damage to the overcoat layer. Nano-indentation demonstrated that the air cavities can withstand forces up to 8750μN, but cycling of loads could not be conducted due to the displacement limitations of the machine. Maintaining mechanical integrity of

the air dielectric layers is a primary challenge for industrial applications. The POSS material was chosen as an overcoat layer because its high hardness allows thin layers of material to suspend the transmission line which increases the amount of air in the cavity. However, the thin glass is brittle and could not withstand polishing or dicing. Extensive mechanical testing is necessary to evaluate if the POSS layer can withstand thermal cycling and shock testing. Thicker, more flexible layers can also be implemented, but the improved mechanical integrity must be balanced with the impact on the electrical properties of the transmission line. The top shielding of the structure was fabricated by bonding the half-coaxial structure with a metal-clad semi-circular trench using the Obducat imprint lithography tool. Strong adhesion was achieved between the layers, and the complete structure was fabricated using a comparable numbers of registration steps as traditional transmission lines.

7.1.2 Mechanically Compliant Chip to Substrate Interconnects

Solder balls are currently used to make the electrical connections from the chip to the substrate and also from the substrate to the board. Solder has some great properties for industrial application such as the ability to compensate for lateral misalignment and non-planar surfaces. However, solder has poor mechanical properties and is difficult to implement as the stand-off distance between the chip and substrate decrease to match the increasing I/O requirements. High performance chip-to-substrate interconnects are necessary to accommodate high frequency signal and to meet the increase in I/O interconnect density. Researchers have developed copper pillars with solder caps to improve the mechanical compliance of solder based structures [81-83]. However, these structures are still limited by the poor mechanical and electrical properties of solder.

Researchers have also developed mechanically compliant, high yield stress polymer pillars with metal cladding [84]. However, plasma etching was used to fabricate the high aspect ratio polymer pillars, and plasma etching of polymer structures at these length scales has poor throughput and is not a cost effective packaging technology. Implementing all copper connections between the chip and substrate would provide high conductivity electrical connections, allow resistance to electromigration, avoid the formation of brittle intermetallics, and reduce reflection loss and impedance mismatch [8]. However, to be viable the copper connections need to have high aspect ratios to be mechanically compliant. The fabrication of high aspect ratio hollow polymer pillars for electroplating copper connections is difficult to achieve with existing materials and traditional photolithography.

In this work, characterization has been conducted on a new high aspect ratio photosensitive polymer Avatrel 8000P and enhanced patterning techniques using imprint lithography to facilitate the fabrication of mechanically compliant all-copper interconnections. Using photolithography, Avatrel 8000P was able to fabricate 7:1 (height:width) aspect ratio lines and 5:1 (height:width) hollow core cylinders. The contrast of the material was studied to understand the limitations of the polymer to pattern high aspect ratio features, and the contrast value for Avatrel 8000P was high, γ=12.2. The high aspect ratios of the patterned Avatrel 8000P films is attributed to its high contrast values and low absorption coefficient. The mechanical and dielectric properties of Avatrel 8000P also impact the interconnections and were evaluated. The fully cross-linked films had an elastic modulus of 2.9 GPa and hardness of 0.18 GPa which corresponded to the lowest measured dielectric constant, ε_r=3.9. Avatrel 8000P's

excellent photo-definition properties, high mechanical strength, and simple baking procedures make it suitable for microelectronics packaging applications.

High aspect-ratio hollow-core pillars are challenging to fabricate with photolithography because light scattering can occur in the core, and the slow transport of developer in the core can cause delamination of the features. A UV imprint lithography process was developed to enhance photo-patterning of polymers. Photo-imprint stamps were fabricated with relief features to displace material in the polymer core, and the photo-pattern was used to chemically, selectively remove the polymer field. The UV imprint lithography process fabricated high aspect ratio hollow core pillars that exceeded the aspect ratio of the stamp feature and also optical resolution capabilities. However, the limited processing windows for Avatrel 2000P and Avatrel 8000P, and the adhesion between the stamp and substrate make this a challenging packaging application.

7. 2 Feasibility and Challenges

Imprint lithography has been shown to have a great variety of process variations[1,3-4,49]. The adaptations reflect the myriad of research in this area, but also reflect that standard processes have not been established for imprint lithography as they have been for other patterning techniques such as photolithography. Standard processes are difficult to define with diverging applications requiring different resolution requirements, resists, and pattern transfer techniques. There are also dimensional challenges that are unique for applications that require a thorough understanding of mechanical deformation and chemical properties to ensure reliable manufacturing. In this thesis, imprint lithography has been applied to enable the fabrication of encapsulated air dielectric layers for ultra-low loss transmission lines and high aspect ratio polymer molds

for mechanically compliant all-copper chip to board connections. Since imprint lithography is a contact patterning method, the process is limited by the capability of a material to be molded to the stamp pattern, and the ability to be de-molded from the stamp without damaging either substrate. Although packaging applications are performed on the microscopic scale, their molding and de-molding behavior are quite different, and a discussion is provided of the feasibility and challenges of implementing imprint lithography for these technologies.

7.2.1 Pattern Filling

Imprint lithography relies on three dimensional mechanical deformation of materials to transfer patterns. A pressure driving force displaces the imprint resist, and capillary forces and surface energy controls the wetting and spreading of the material. The simplest case in imprint lithography is that of the squeeze-flow of a Newtonian fluid between two parallel disks separated by a distance corresponding to the thickness of the fluid layer. Mold filling depends on the pattern size and density, and the resist flow is governed by the viscoelastic properties of the material at the imprint temperature and pressure.

Planarizing PPC using imprint lithography corresponds to this simple case of fluid flow between two parallel plates, and a planar PPC layer was achieved without difficulty. Planar fields and good pattern transfer were also obtained when imprinting the semi-circular lines. However, imprinting the high aspect ratio hollow pillars was a much more challenging pattern filling case. As shown by the thermoplastic imprint microscope pictures and non-planarity analysis in Chapter 6, there are flow fields remaining after thermoplastic imprint for both Avatrel 8000P and Avatrel 2000P. Longer times and

higher pressures were attempted, but significant improvement in field planarity was not achieved. Elevating the imprint temperature made the largest impact on field planarity, but the imprint temperature was limited due to the susceptibility of the material to initiate thermal cross-linking. Incomplete pattern transfer reduced the aspect ratio of the imprinted Avatrel 8000P structures, but complete filling was not critical for this application since photo-patterning eliminated the residual flow fields. However for many applications, flow borders around imprinted features can deteriorate the quality of the pattern. This application requires optimization of materials where different factors must be balanced. The high aspect ratio polymer molds require a material with a high modulus and hardness, but the mechanical properties of the material makes imprinting at modest pressures difficult, and the photo-sensitive nature of the material limits the imprint temperature.

Displacement of large fields of material, plug flow in high aspect ratio cavities, and high density patterning is challenging with imprint lithography, and numerous scientific advances must take place before imprint lithography can have widespread implementation for these applications. Modeling of the complex flow fields, and the stress on the stamp and substrate during molding and de-molding could facilitate improved stamp design and process schemes. Elevated temperatures and increased imprint times could also facilitate implementation of some applications. However, for an imprint time of one minute at 100°C, the actual time to load, ramp to process conditions, imprint, cool, and separate is on the order of 15 minutes. Operating at elevated process temperature further increases the time to run a sequence. Short process times are preferable for industrial application. As shown in Chapter 6, high modulus,

photosensitive materials have limited processing windows, and advanced materials are needed that have large operating windows with adaptability for specific applications.

7.2.2 Adhesion and Stamp Damage

High end photolithography avoids the mechanical contact of the mask and resist, and therefore extends the life of the photolithography masks. However, imprint lithography requires intimate contact between the stamp and resist. One primary challenge of imprinting for microelectronics packaging is the task of minimizing adhesion between the stamp and the mold. During de-molding, high adhesion and friction forces are exerted on stamp structures. The friction and strain can cause deformation in the form of cracking or abrasion. Furthermore, stress can build between layers during imprint leading to the delamination of layers. The level of adhesion between stamps and molds depends on the stamp materials, the imprint materials, the processing conditions, and the geometry and the density of the patterns being transferred.

In the case of planarizing PPC for the low-loss transmission lines, adhesion between the stamp and the PPC was minimal. Since a flat glass stamp was used to push the PPC into the semi-circular trench, the surface area in contact between the stamp and substrate was the minimal case for imprint lithography. Furthermore, the PPC was imprinted at a moderate temperature of 60°C and with minimal adhesion when one of several anti-adhesion layers were used, including gold, with (3,3,3-trifluoropropyl)dimethylchlorosilane, and Teflon AF.

For imprinting the semi-circular stamp into Avatrel 2000P, the density of the lines and the surface area between the stamp and substrate was low. The surface area of the semi-circular line for a 1 cm^2 die was $1.4x10^{-3}$ cm^2. The Avatrel 2000P had a relatively

high adhesion to the stamps requiring frequent recoating of the Parylene C and Teflon AF anti-adhesion layers. To separate the stamps, razor blades were used to wedge the stamp and substrate apart. Furthermore, the imprint stamps were diced into 1 cm^2 dies to allow for increased separation force per die.

For imprinting the high aspect ratio structures into Avatrel 2000P and Avatrel 8000P, the density of the features was considerably greater. Also since the pillars being imprinted were free standing, there was a much greater surface area in contact between the stamp and the imprint materials. For the stamp with the 15 μm tall pillars, the surface area of the features was $1.2x10^{-2}$ cm^2 for a 1 cm^2 die which is an order of magnitude greater than the semi-circular line stamp. Using imprint stamps that were 1 cm^2 die, and frequent recoating with Teflon AF made separation of the stamp and substrate manageable. The stamps imprinted into Avatrel 2000P were 60 μm tall pillars with much larger feature sizes, significantly increasing the surface area in contact with the stamp. These imprint samples were extremely difficult to separate, even with small stamp die. Imprinting high aspect ratio structures on the micrometer scale is particularly challenging because of the high level of surface area in contact between the stamp and the imprint material. Improved the anti-adhesion layers or separation techniques are necessary to implement imprint lithography for high surface area applications.

Adhesion and particle entrapment were among the primary causes of damage to imprint stamps. For planarizing surfaces, damage never occurred to the flat substrates and they could be recycled often. For the semi-circular imprint stamps, damage never occurred to the physical relief feature, but particle entrapment and buildup of contamination caused cracking of the substrates limiting their reuse. Packaging facilities

do not have the controlled particle counts found in semi-conductor fabrication. Therefore, techniques to minimize particle entrapment and to thoroughly clean stamps are necessary for industrial implementation of imprint lithography for packaging applications. Intermediate layers such as the intermediate polymer stamps demonstrated by Obducat are one solution to reduce contamination and to extend the life of imprint stamps [36-37]. For imprinting high aspect ratio structures, the adhesion forces were high and some metal pillars would shear from the stamp and become trapped into the imprint polymer after de-molding. Stamp damage is a significant challenge for an industrial application because the fabrication of complex stamps adds to the cost of the process. To be a low cost alternative lithographic technique, imprint stamp must withstand multiple imprint cycles. In addition to improved anti-adhesion layers, modeling needs to be conducted to design stamps structures that can withstand the forces of de-molding. Furthermore, as imprint stamps are recycled, the likelihood of damage to the stamp increases. Additionally, thermal and pressure cycling and separation produce wear on the stamp. In-situ techniques are needed to analyze the stamp to assess when anti-adhesion layers need to be recoated and when stamp features such as the high aspect ratio pillars are too fatigued to withstand imprint forces. Another source of damage during imprinting was the buildup of stress during imprint cycles. The photosensitive tapes were difficult to implement as a release layer because the CTE mismatch caused buckling of the film with rapid heating and cooling rates. To fabricate multilayer structures, materials need to be selected with similar CTE properties and process windows to mitigate stress buildup between different layers during imprint heating and cooling cycles.

7. 3 Future Directions

In this research, imprint lithography has been used to fabricate advanced transmission lines on the printed circuit board and high aspect ratio polymer molds for all copper chip to board connections. Before imprint lithography can be industrially implemented for packaging applications, predictive models are necessary to model the complex flow fields that arise during imprinting and of the stresses that occur to the stamp and substrate during molding and de-molding. This modeling would facilitate improved stamp design, process schemes, and imprint material selection. Improved anti-adhesion layers, techniques to quantify substrate/stamp adhesion and methods to minimize stamp contamination are also necessary.

Electrical test structures must also be built to quantify the electrical improvement of the metal-clad encapsulated air gap structure with traditional transmission lines and other advanced transmission lines. Processes must be developed to simultaneously form the line and via and to connect the air-gap transmission lines with vertical connections to the all copper chip-to-board interconnections. Thermo-mechanical reliability studies must also be conducted for the off-chip and chip-to-board connections. Further material studies are also necessary to optimize polymer photo-definition, mechanical, and electrical properties for these applications.

APPENDIX A

PROCESS SCHEMATIC FOR AIR-CLAD DIELECTRIC LAYERS

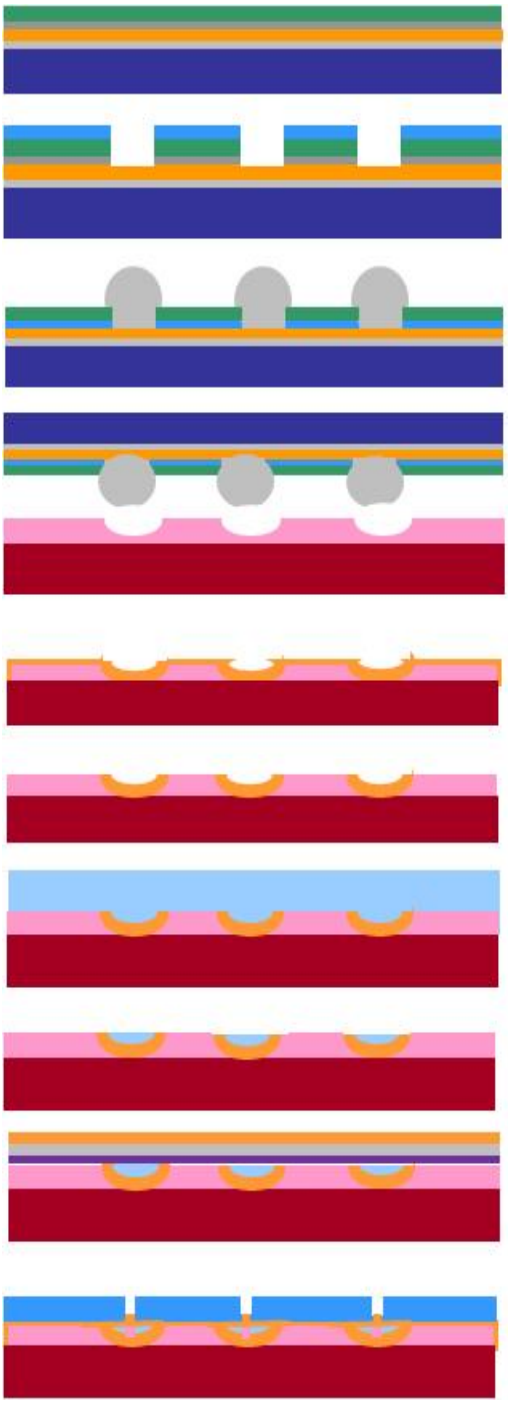

Strip resist, etch back seed layer, and decompose sacrificial layer

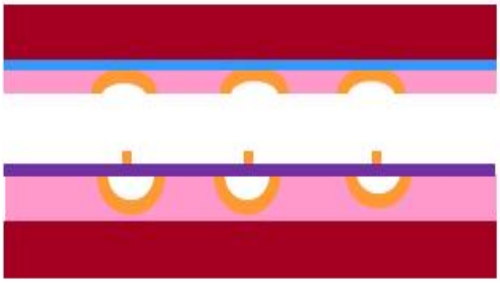

Take another Avatrel sample on a sacrificial substrate and make the copper shield;
Align and bond to complete coaxial structure

Remove top substrate

APPENDIX B

PROCESS SCHEMATIC OF HIGH ASPECT RATIO POLYMER MOLDS

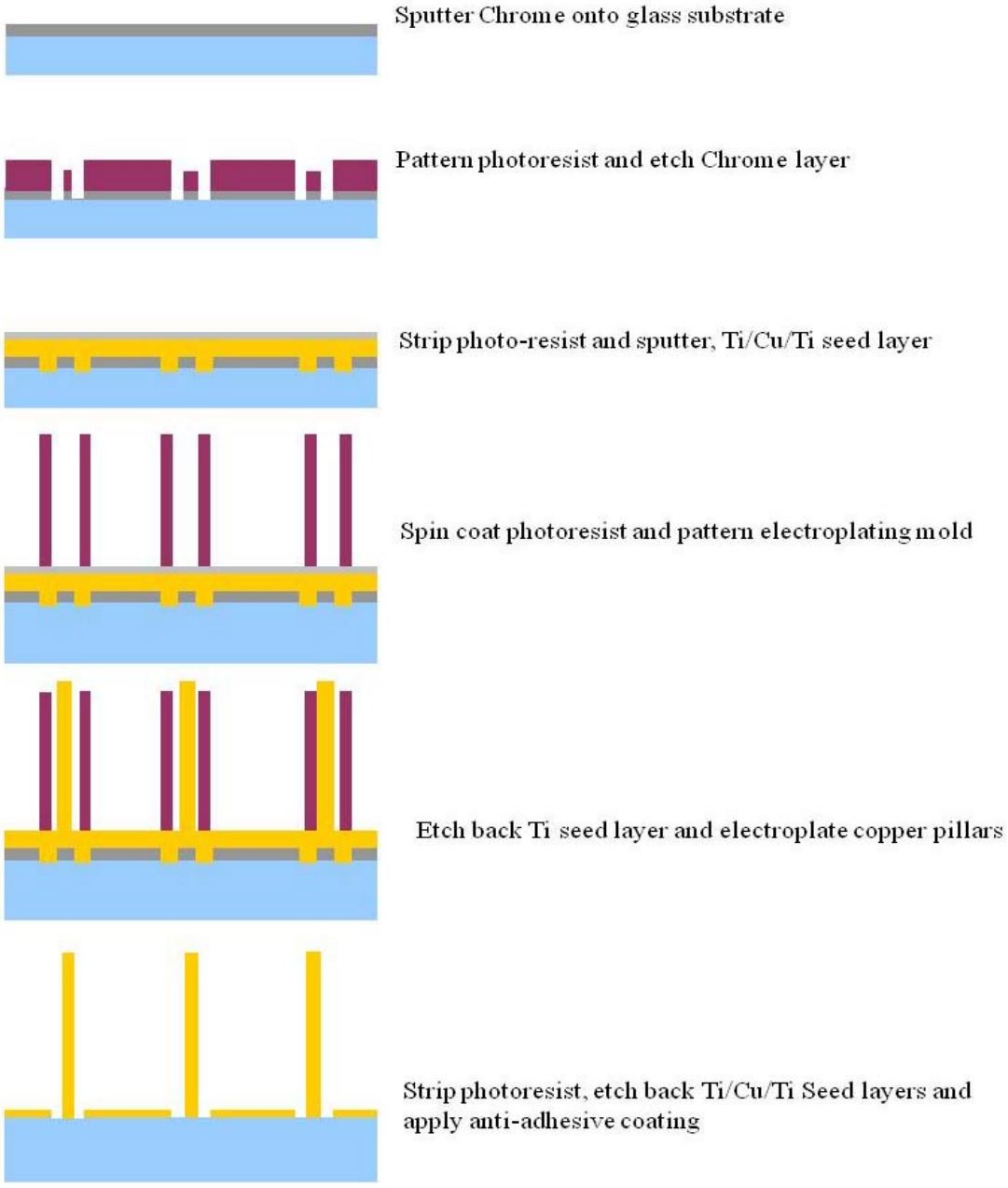

Coat substrate with photo-sensitive dielectric

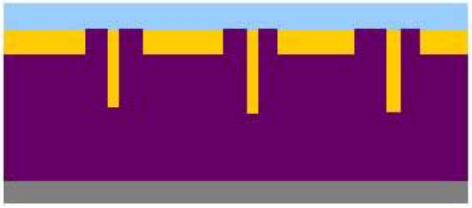

Imprint and expose

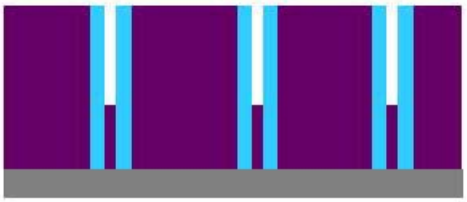

Separate

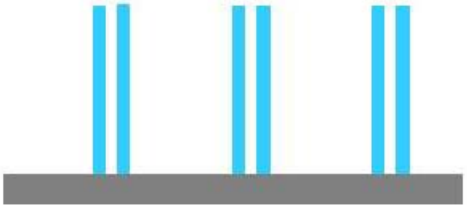

Develop

REFERENCES

1. Chou, S. Y.; Krauss, P. R.; Renstrom, P. J. *Applied Physics Letters* **1995**, *67*, 3114.

2. Guo, L.; Krauss, P.; Chou, S. *Applied Physics Letters* **1997**, *71*, 1881.

3. Jaszewski, R.; Schift, H.; Gobrecht, J.; Smith, P. *Microelectronic Engineering* **1998**, *41*, 578.

4. Resnick, D.; Dauksher, W.; Mancini, D.; Nordquist, K.; Ainley, E.; Gehoski, K.; Baker, J.; Bailey, T.; Choi, B.; Johnson, S. *Journal of Microlithography, Microfabrication, and Microsystems* **2002**, *1*, 284.

5. Chou, S.; Krauss, P.; Zhang, W.; Guo, L.; Zhuang, L. *Journal of Vacuum Science and Technology-Section B-Microelectronics Nanometer Structur* **1997**, *15*, 2897.

6. Tummala, R. *Fundamentals of microsystems packaging*; McGraw-Hill Professional, 2001.

7. Pozar, D. *Microwave Engineering, 3rd*; John Wiley & Sons, Hoboken, NJ, USA, 2005.

8. Dubin, V.; Thomas, C.; Baxter, N.; Block, C.; Chikarmane, V.; McGregor, P.; Jentz, D.; Hong, K.; Hearne, S.; Zhi, C. In *IEEE International Interconnect Technology Conference.* 2001, p 271.

9. He, A.; Osborn, T.; Allen, S.; Kohl, P. *Electrochemical and Solid-State Letters* **2006**, *9*, C192.

10. Pohlmann, K.; Carver, B.; Design, C.; Concerns, P.; Formats, D.; Manufacturing, D. *AR Editions, Madison, WI* **1992**.

11. Menz, W.; Mohr, J.; Paul, O. *Microsystem technology*; Vch Verlagsgesellschaft Mbh, 2001.

12. Herzig, H. *Micro-optics: Elements, systems and applications*; CRC, 1997.

13. Baraldi, L.; Kunz, R.; Meissner, J. In *Proc. SPIE* 1992; Vol. 21.

14. Schift, H. *Science and New technology in Nanoimprint*; Frontier Publishing: Japan, 2006.

15. ITRS, The International Technology Roadmap for Semiconductors, 2007, http:///www.itrs.net

16. Bertsch, A.; Lorenz, H.; Renaud, P. In *IEEE Micro Electro Mechanical Systems* 1998, p 18.

17. Cheng, X.; Jay Guo, L. *Microelectronic Engineering* **2004**, *71*, 288.

18. Chou, S. Y.; Krauss, P. R.; Kong, L. *Journal of Applied Physics* **1996**, *79*, 6101.

19. Chou, S. Y.; Krauss, P. R.; Renstrom, P. J. *Journal of Vacuum Science & Technology B* **1996**, *14*, 4129.

20. Chou, S.; Krauss, P.; Renstrom, P. *Science* **1996**, *272*, 85.

21. Scheer, H.; Schulz, H.; Hoffmann, T.; Torres, C. *Journal of Vacuum Science & Technology B: Microelectronics and Nanometer Structures* **1998**, *16*, 3917.

22. Schift, H.; Heyderman, L.; der Maur, M.; Gobrecht, J. *Nanotechnology* **2001**, *12*, 173.

23. Heyderman, L.; Schift, H.; David, C.; Gobrecht, J.; Schweizer, T. *Microelectronic Engineering* **2000**, *54*, 229.

24. Krauss, P.; Chou, S. *Applied Physics Letters* **1997**, *71*, 3174.

25. Yu, Z.; Schablitsky, S.; Chou, S. *Applied Physics Letters* **1999**, *74*, 2381.

26. Guo, L.; Leobandung, E.; Chou, S. *Science* **1997**, *275*, 649.

27. Zhang, W.; Chou, S. *Applied Physics Letters* **2001**, *79*, 845.

28. Schulz, H.; Scheer, H.; Hoffmann, T.; Torres, C.; Pfeiffer, K.; Bleidiessel, G.; Grützner, G.; Cardinaud, C.; Gaboriau, F.; Peignon, M. *Journal of Vacuum Science & Technology B: Microelectronics and Nanometer Structures* **2000**, *18*, 1861.

29. Li, M. In *Electron, Ion and Photon Beam Technol. and Nanofabrication* Palms Springs ,CA, 2000.

30. Haisma, J.; Verheijen, M.; Van Den Heuvel, K.; Van Den Berg, J. *Journal of Vacuum Science & Technology B: Microelectronics and Nanometer Structures* **1996**, *14*, 4124.

31. Bouwhuis, G. *Principles of optical disc systems*; Taylor & Francis, 1985.

32. Colburn, M. In *SPIE's 25th Intl. Symp.* Santa Clara, CA, 2000.

33. Choi, B.; Meissl, M.; Colburn, M.; Bailey, T.; Ruchhoeft, P.; Sreenivasan, S.; Prins, F.; Banerjee, S.; Ekerdt, J.; Willson, C. In *Proc. SPIE* 2001; Vol. 4343, p 436.

34. Cheng, X. C., M. H.; Guo, L. J. In *Proceedings of SPIE* 2004; Vol. 5374, p 337.

35. Suh, D.; Choi, S.; Lee, H. *Advanced Materials* **2005**, *17*, 1554.

36. Beck, M.; Heidari, B. 2006, p 22.

37. Dauksher, W. J.; Le, N. V.; Gehoski, K. A.; Ainley, E. S.; Nordquist, K. J.; Joshi, N. In *Proc. SPIE*; Michael, J. L., Ed.; SPIE: 2007; Vol. 6517, p 651714.

38. Jung, G.; Li, Z.; Wu, W.; Chen, Y.; Olynick, D.; Wang, S.; Tong, W.; Williams, R. *Langmuir* **2005**, *21*, 1158.

39. Schift, H.; Saxer, S.; Park, S.; Padeste, C.; Pieles, U.; Gobrecht, J. *Nanotechnology* **2005**, *16*, 171.

40. Houle, F.; Rettner, C.; Miller, D.; Sooriyakumaran, R. *Applied Physics Letters* **2007**, *90*, 213103.

41. Ramachandran, S.; Tao, L.; Lee, T.; Sant, S.; Overzet, L.; Goeckner, M.; Kim, M.; Lee, G.; Hu, W. *Journal of Vacuum Science & Technology B: Microelectronics and Nanometer Structures* **2006**, *24*, 2993.

42. Nakamatsu, K.; Yamada, N.; Kanda, K.; Haruyama, Y.; Matsui, S. *Japan. J. Appl. Phys* **2006**, *45*.

43. Khang, D.; Kang, H.; Kim, T.; Lee, H. *Nano Lett* **2004**, *4*, 633.

44. Khang, D.; Lee, H. *Langmuir* **2004**, *20*, 2445.

45. Choi, P.; Fu, P.; Guo, L. *Advanced Functional Materials* **2007**, *17*, 65.

46. Hirai, Y.; Harada, S.; Kikuta, H.; Tanaka, Y.; Okano, M.; Isaka, S.; Kobayasi, M. *Journal of Vacuum Science & Technology B: Microelectronics and Nanometer Structures* **2002**, *20*, 2867.

47. Schift, H.; Heyderman, L. J. In *Nanostructure Science and Technology*; Kulwer Academic: New York, 2003, p 46.

48. Schift, H.; Bellini, S.; Gobrecht, J.; Reuther, F.; Kubenz, M.; Mikkelsen, M.; Vogelsang, K. *Microelectronic Engineering* **2007**, *84*, 932.

49. Scheer, H.; Bogdanski, N.; Wissen, M.; Konishi, T.; Hirai, Y. *Journal of Vacuum Science & Technology B: Microelectronics and Nanometer Structures* **2005**, *23*, 2963.

50. Hirai, Y. *Journal of Photopolymer Science and Technology* **2005**, *18*, 551.

51. Schift, H. *Journal of Vacuum Science & Technology B: Microelectronics and Nanometer Structures* **2008**, *26*, 458.

52. Schulz, H.; Wissen, M.; Bogdanski, N.; Scheer, H.; Mattes, K.; Friedrich, C. *Microelectronic Engineering* **2006**, *83*, 259.

53. May, G. S.; Sze, S. M. *Fundamentals of Semiconductor Fabrication*; John Wiley & Sons, Inc.: Hoboken, NJ, 2004.

54. Stoney, G. *Proc. R. London* **1909**, *Ser. A*.

55. Klein, C. A. *Journal of Applied Physics* **2000**, *88*, 5487.

56. Loubet, J.L.; Georges, J.M.; Marchesini, O.; Meille, G. 1984; Vol. 106(1), p 43.

57. Jian, S.; Li, X.; Guo, S.; Hu, Y.; Yang, J.; Jiang, Q. *Smart Materials and Technology* **2005**, *144*, 769.

58. Yuan, Z.Y., Xu, D., Ye, Z.C., Cai, B.C. *Journal of Materials Science and Technology* **2005**, *21*, 319.

59. Shaw, G.A.; Trethewethy, J.S.; Johnson, A.D.; Drugan, W.J.; Crone, W.C. *Advanced Materials* **2005**, *17*, 1123.

60. VanLandingham, M.R.; Villarrubbia, J.S.; Guthrie, W.F.; Meyers, G.F. **2001**, *167*, 15.

61. Briscoe, B. J.; Fiori, L.; Pelillo, E. *Journal of Physics D-Applied Physics* **1998**, *31*, 2395.

62. Shen, L.; Phang, I. Y.; Liu, T. X.; Zeng, K. Y. *Polymer* **2004**, *45*, 8221.

63. Oliver, W. C.; Pharr, G. M. *J. Mater. Res.* **1992**, *7*, 1564.

64. Stillwell, N. A.; Tabor, D. *Proc. Phys. Soc. London* **1961**, *78*.

65. Tabor, D. *Proc. R. Soc. A* **1948**, *192*, 247.

66. Wornyo, E.; Gall, K.; Yang, F.; King, W. *Polymer* **2007**, *48*, 3213.

67. Klapperich C; Komvopoulos, K.; Pruitt, L. *Journal of Tribology-Transactions of the ASME* **2001**, *123*, 624.

68. Chen, L.; Varadan, V. *Microwave electronics: measurement and materials characterization*; John Wiley & Sons Inc, 2004.

69. Djordjevi, A.; Biljie, R.; Likar-Smiljanic, V.; Sarkar, T. *Ieee Transactions on Electromagnetic Compatibility* **2001**, *43*, 662.

70. Hoyeol, C.; Kyung-Hoae, K.; Kapur, P.; Saraswat, K. C. *Electron Device Letters, IEEE* **2008**, *29*, 122.

71. Lee, H.; Shin, D.; Kim, S.; Lim, B.; Baek, T.; Ko, B.; Chun, Y.; Kim, S.; Park, H.; Rhee, J. *Journal of Micromechanics and Microengineering* **2004**, *14*, 746.

72. Yook, J.; Kim, K.; Kwon, Y. *IEEE Microwave and Wireless Components Letters* **2009**, *19*, 623.

73. Jun-De Jin, S.; Yang, M.; Liu, S. *IEEE Transactions on Microwave Theory and Techniques* **2006**, *54*, 4333.

74. Natarajan, S.; Weller, T.; Hoff, A. In *IEEE MTT-S International Microwave Symposium Diges* 2006, p 424.

75. Pascariu, G.; Cronin, P.; Crowley, D. In *Proceedings of Electronics Manufacturing Technology Symposium* 2003, p 423.

76. Suthiwongsunthorn, N.; Kilbey, N.; Cordery, A. *IEEE Transactions on Components and Packaging Technologies* **2003**, *26*, 503.

77. Ganasan, J. *IEEE Transactions on Electronics Packaging Manufacturing* **2000**, *23*, 28.

78. Yala, N.; Gamota, D. *IEEE Transactions on Electronics Packaging Manufacturing* **2001**, *24*, 31.

79. Kang, S.; Kim, C.; Muncy, J.; Schmidt, M.; Lee, S.; Baldwin, D. In *IEEE Electronic Components & Technology Conference* 2005, p 832.

80. Lodge, K.; Pedder, D. *IEEE Transactions on Components, Hybrids, and Manufacturing Technology* **1990**, *13*, 847.

81. Wang, T.; Tung, F.; Foo, L.; Dutta, V.; Ltd, A. In *Proceedings of the Electronic Components Technology Conference* 2001, p 945.

82. Rao, V.; Tay, A.; Kripesh, V.; Lim, C.; Yoon, S. In *Electronic Packaging Technology Conference* 2004, p 444.

83. Tummala, R. R.; Markondeya Raj, P.; Aggarwal, A.; Mehrotra, G.; Sau Wee, K.; Bansal, S.; Tan Teck, T.; Ong, C. K.; Chew, J.; Vaidyanathan, K.; Srinivasa Rao, V. In *Electronic Components and Technology Conference, 2006. Proceedings. 56th* 2006, p 10 pp.

84. Aggarwal, A.; Raj, P.; Tummala, R. *IEEE Transactions on Advanced Packaging* **2007**, *30*, 384.

85. DuPont, Teflon® AF Properties, 2010, http://www2.dupont.com/Teflon_Industrial/en_US/products/product_by_name/teflon_af/properties.html

86. Promerus, Materials, 2008, http://www.promerus.com/packaging_materials.asp

87. Empower-Materials, Poly(Alkylene Carbonates) Typical Properties, 2008, http://www.empowermaterials.com/download/Technical%20Information/typical_properties.pdf.

88. Jayachandran, J.; Reed, H.; Zhen, H.; Rhodes, L.; Henderson, C.; Allen, S.; Kohl, P. *Microelectromechanical Systems, Journal of* **2003**, *12*, 147.

89. Cupta, M., Georgia Institute of Technology, 2006.

90. Fritz, N.; Saha, R.; Allen, S.; Kohl, P. *Journal of Electronic Materials* **2010**, *39*, 149.

91. Reed, H.; White, C.; Rao, V.; Allen, S.; Henderson, C.; Kohl, P. *Journal of Micromechanics and Microengineering* **2001**, *11*, 733.

92. Spencer, T., Georgia Institute of Technology, 2010.

93. Wu, X.; Reed, H.; Wang, Y.; Rhodes, L.; Elce, E.; Ravikiran, R.; Shick, R.; Henderson, C.; Allen, S.; Kohl, P. *Journal of The Electrochemical Society* **2003**, *150*, H205.

94. Bakir, M. S.; Reed, H. A.; Thacker, H. D.; Patel, C. S.; Kohl, P. A.; Martin, K. P.; Meindl, J. D. *Electron Devices, IEEE Transactions on* **2003**, *50*, 2039.

95. Hoff, J.; Cheng, L.; Meyhofer, E.; Guo, L.; Hunt, A. *Nano Letters* **2004**, *4*, 853.

96. Wang, X.; Ge, L.; Lu, J.; Li, X.; Qiu, K.; Tian, Y.; Fu, S.; Cui, Z. *Microelectronic Engineering* **2009**, *86*, 1347.

97. Bai, Y. Q.; Chiniwalla, P.; Elce, E.; Allen, S. A. B.; Kohl, P. A. *Journal of Applied Polymer Science* **2004**, *91*, 3031.

98. Bai, Y. Q.; Chiniwalla, P.; Elce, E.; Shick, R. A.; Sperk, J.; Allen, S. A. B.; Kohl, P. A. *Journal of Applied Polymer Science* **2004**, *91*, 3023.

99. Chiniwalla, P.; Bai, Y. Q.; Elce, E.; Shick, R.; Allen, S. A. B.; Kohl, P. *Journal of Applied Polymer Science* **2004**, *91*, 1020.

100. Chiniwalla, P.; Bai, Y. Q.; Elce, E.; Shick, R.; McDougall, W. C.; Allen, S. A. B.; Kohl, P. A. *Journal of Applied Polymer Science* **2003**, *89*, 568.

101. Feng, R.; Farris, R. *Journal of Micromechanics and Microengineering* **2003**, *13*, 80.

102. Shaw, J. M.; Gelome, J. D.; Labianca, N.; Conley, W. E.; Holmes, S. J. *IBM J. Res. Dev.* **1997**, *41*.

103. IBM, 1989, 4882245

104. Lee, C.; Jiang, K. *Journal of Micromechanics and Microengineering* **2008**, *18*, 055032.

105. Lee, K.; LaBianca, N.; Rishton, S.; Zolgharnain, S.; Gelorme, J.; Shaw, J.; Chang, T. *Journal of Vacuum Science & Technology B: Microelectronics and Nanometer Structures* **1995**, *13*, 3012.

106. LaBianca, N. In *Proceedings of SPIE - The International Society for Optical Engineering* 1995 p846

107. Lorenz, H. *Journal of Micromechanics and Microengineering* **1997**, *7*, 121.

108. Despont, M. et. al In *10th IEEE Micro. Electro. Mech. Sys.* 1997, p 518.

109. Lorenz, H.; Laudon, M.; Renaud, P. *Microelectron. Eng* **1998**, *41*, 371.

110. MicroChem, 2008, http://www.microchem.com/products/pdf/SU-82000DataSheet2000_5thru2015Ver4.pdf

111. http://www.microchem.com/products/su_eight.htm

112. Materials, American Society for Testing Materials, Standard Test Methods for AC Loss Characteristics and Permittivity (dielectric constant) of Solid Electrical Insulating Materials, 1992,

113. MicroChem, 2009, http://www.microchem.com/products/su_eight_faq.htm

114. Eyre, B.; Closiu, J.; Wiberg, D. In *11th IEEE Micro. Elec. Mech. Sys.* Chicago, USA, 1995, p 218.

115. Patel, K. *Journal of Applied Polymer Science* **2001**, *80*, 2328.

116. Hammacher, J.; Fuelle, A.; Flaemig, J.; Saupe, J.; Loechel, B.; Grimm, J. *Microsystem Technologies* **2008**, *14*, 1515.

117. Cheng, X.; Jay Guo, L. *Microelectronic Engineering* **2004**, *71*, 277.